REIHE 18
MECHANIK/
BRUCHMECHANIK

Fortschritt-Berichte VDI

M.Sc. Christian Woitzik,
Hamburg

NR. 356

Experimental testing and numerical simulation of granules as crash absorber for double hull structures

BAND
1|1

VOLUME
1|1

REIHE 18
MECHANIK/
BRUCHMECHANIK

Fortschritt-Berichte VDI

M.Sc. Christian Woitzik,
Hamburg

NR. 356

Experimental testing and numerical simulation of granules as crash absorber for double hull structures

BAND
1|1

VOLUME
1|1

VDI verlag

VDI verlag

Woitzik, Christian

Experimental testing and numerical simulation of granules as crash absorber for double hull structures

Fortschritt-Berichte VDI, Reihe 18, Nr. 356. Düsseldorf: VDI Verlag 2021.

142 Seiten, 134 Bilder, 17 Tabellen.

ISBN 978-3-18-335618-8, ISSN 0178-9457

52,00 EUR/VDI-Mitgliederpreis: 46,80 EUR

Für die Dokumentation: Kollisionssicherheit – Doppelhülle – Martime Anwendung – Crash-Absorber – Kollisionsversuch – Granulate – Expandiertes Glass-Granulat – Experimentelle Untersuchung – Finite-Elemente-Methode

Keywords: Collision safety – Double hull structure – Maritime applications – Crash absorber – Collision test – Granules – Expanded glass material – Experimental testing – Finite element method

In the maritime sector, the collision safety is an essential aspect of ship operation. Aiming at further improvements, the filling of the cavity in a double hull structure with granular material is investigated in this thesis. In order to do so, the potential of different granules is determined experimentally, along with the description of their material parameters as particles and as a bulk material, respectively. Furthermore, a simplified side hull structure is designed for experimental testing, followed by a numerical study of different material models for the granules. This leads to the simulation of a realistic collision scenario, showing the potential in the maritime industry.

Bibliographische Information der Deutschen Bibliothek
Die Deutsche Bibliothek verzeichnet diese Publikation in der Deutschen Nationalbibliographie; detaillierte bibliographische Daten sind im Internet unter www.dnb.de abrufbar.

Bibliographic information published by the Deutsche Bibliothek (German National Library)
The Deutsche Bibliothek lists this publication in the Deutsche Nationalbibliographie (German National Bibliography); detailed bibliographic data is available via Internet at www.dnb.de.

Arbeitsgruppe Numerische Strukturanalyse mit Anwendungen in der Schiffstechnik

ISBN 978-3-18-335618-8, ISSN 0178-9457

Experimental testing and numerical simulation of granules as crash absorber for double hull structures

Vom Promotionsausschuss der
Technischen Universität Hamburg

zur Erlangung des akademischen Grades

Doktor-Ingenieur (Dr.-Ing.)

genehmigte Dissertation

von
Christian Woitzik, M.Sc.

aus
Hamburg

2021

Vorsitzender des Prüfungsausschusses
Prof. Dr.-Ing. Thomas Rung

Gutachter
1. Gutachter: Prof. Dr.-Ing. habil. Alexander Düster
2. Gutachter: Prof. Dr.-Ing. habil. Dr. h.c. mult. Dr.-Ing. E.h. Peter Wriggers

Tag der mündlichen Prüfung: 3. August 2021

Acknowledgements

This thesis is the result of my work at the Institute for Ship Structural Design and Analysis (M-10) at Hamburg University of Technology (TUHH). It was funded by the Deutsche Forschungsgemeinschaft (DFG) in the period from October 2015 to February 2020 and was carried out in cooperation with the Leibniz University Hannover. Many people contributed to my work and supported me during this time – and I would like to thank all of them for their help.

First, I would like to express my gratitude to Prof. Dr.-Ing. habil. Alexander Düster, the supervisor of this work. Dear Prof. Düster, your expertise, your helpfulness and our fruitful discussions were a great support during my time working with you. I would also like to thank Prof. Dr.-Ing. habil. Dr. h.c. mult. Dr.-Ing. E.h. Peter Wriggers – for acting as co-supervisor for this thesis and for his ideas and helpful comments during several project meetings – and Prof. Dr.-Ing. Thomas Rung for chairing my PhD-examination.

Further, I would like to thank all my colleagues: First of all, my project partner Mohsin Chaudry from the Leibniz University Hannover, who was always open to discussions. Next, the colleagues in our laboratory, as well as from other institutes, who helped me a lot with the experiments and invested a lot of their free time to do so. And of course, all my colleagues at M-10, who have always been an inspiration and made my time at the university very pleasant.

Last but not least, my heartfelt thanks go to my family and friends for their moral support. In particular, I want to thank my beloved mother. Thank you for your endless love, faith, and support in my life.

Contents

Abstract

In the maritime sector, the collision safety is an essential aspect of ship operation. In order to advance, new options have to be investigated. A recent idea is to fill the cavity in the double hull structure of a ship. To do so, this thesis provides fundamental research in this field.

Thus, the aim of this thesis is to investigate the potential of using granules as filling material based on experiments. Furthermore, the numerical modelling of these granules shall be investigated and verified.

In order to achieve this, several aspects have to be considered. Starting with the basic idea, suitable granules have to be determined. Therefore, a list of requirements is developed and experiments for the mechanical characterization of granules are developed. To describe the behaviour of single grains, a statistical approach is applied. The mechanical properties, such as crushing strength, and Young's modulus are determined using a single particle test assuming a Hertzian contact model. Based on this, a three-dimensional model covering the probability of the parameter distribution in combination with the diameter distribution is developed.

For the numerical modelling of the granules as bulk material, experiments such as oedometer test, triaxial test, and friction test are performed. This test data is used to calibrate and validate the numerical models used in this thesis. For the calibration, we use a numerical optimization to fit the material parameters to the experimental results, comparing these values with parameters obtained by identification using only experimental data.

One of the main aspect of this thesis is related to examine the potential of the granules used as filling material. Thus, a simplified side hull structure is designed for experimental testing. In these tests, reference experiments without granular material are performed. These are compared with structures containing granules. To do so, aside strain and displacement sensors, a digital image correlation system is used. In addition, we investigate the influence of the granules to stiffeners in the side hull structure. In doing so, the energy dissipation in case of a collision shall be increased.

The second main aspect refers to the numerical modelling of these experiments and the validation of different material models used for simulation. To do so, a continuum approach is applied, using the finite element method with explicit time stepping scheme. The granules are modelled using the Mohr-Coulomb material model and the hypoplastic material model, comparing the abilities of these in combination with the different material parameter sets. The advantages and disadvantages are discussed, leading to a recommendation for the application in finite element simulations.

In the last part of this thesis, we apply the numerical model to a mid-ship structure, comparing the two granules. Furthermore, we show possible changes in design, using the increase in collision resistance with granules. This addresses the potential in maritime industry, considering filling material in the design process of a ship structure.

1 Introduction

Granules are a popular material in modern industry. They combine features such as lightweight with strength, and are therefore considered in more and more fields of industrial and engineering applications: in civil engineering – where granules are used as a material for insulation, levelling, or as a lightweight aggregate for concrete – in the automotive and aviation industry (as a reinforcement material), in the chemical industry (as active materials) and in many other fields of application. Taking advantage of the dissipative behaviour of granules, they are also used for crash absorption purposes.

All the applications above require advanced knowledge about the particles. On a larger scale, the macroscopic description of the bulk behaviour can be satisfactory. Changing the point of view to a smaller scale, e.g. the particle size, a better understanding of the mechanical behaviour and material properties moves into focus. In particular, particle crushing under high load is a very complex mechanism.

In the maritime sector, the collision behaviour of ships plays an important role with respect to the ship safety. The improvement of crashworthiness of a vessel is always an aspect regarding the development, manufacturing, and operation of a ship. A double hull structure is a widely used design for tankers, bulk carries, container ships, as well as for many other types of ships. This thesis investigates the potential outcome focusing on the design of a double hull structure. To put the empty space into a good use, granules are considered as a filling material for further improvements in crashworthiness. In order to do so, the description of the granular behaviour will be of particular interest. Therefore, experimental testing of the granules will be carried out, followed by a numerical study to describe the mechanical behaviour. In the following, the general idea will be motivated in more detail, substantiated by a brief overview of the state of the art. Subsequently, the aim of this thesis will be presented and the content will be outlined.

1.1 Motivation

Precisely in view of the increasing cargo transport by sea, there is also an increased risk of ship collisions. During the last decades, the amount of cargo transported by ship has increased significantly, which results in more and larger ships manoeuvring on the seas and in harbours. Despite improvements in collision avoidance – e.g. traffic segregation or radar systems – collisions can and will still occur due to human and technical errors. Today, an additional risk factor is introduced through the installation of offshore wind turbines. As fixed foundation wind turbines are limited to coastal areas, they are often found close to estuaries used by ships. Furthermore, floating offshore wind turbines are under development and will fill the seas further away from the coast.

Apart from the increase in ship traffic, there is also more environmental awareness. The catastrophic consequences of large oil spills in the last decades, such as *Exxon Valdez* [1] or *Prestige* [2], puts ship safety more and more to the forefront. This has already resulted in design specifications such as double hull structures for oil tankers, leading to a reduction of catastrophic ship accidents.

Nevertheless, all these factors contribute to a higher demand in ship collision safety. Modern engineering tools such as the finite element method (FEM), and its advances in solving non-linear problems and including contact formulations, urge to investigate the collision behaviour of ships using simulations. The advantage of this approach cannot be dismissed: It is cheaper than actual testing, and it can be used in an early design stage during ship development to find weaknesses and to evaluate design improvements. The increasing availability of computational power makes this approach even more attractive. Today, there exist several commercial FEM tools that are used as standard tools in industry. The numerical methods and material models have already been validated for a wide range of applications, but there is still room for improvement.

Considering the collision safety of double hull structures, changes in the structural design can be sufficiently evaluated with numerical methods in a fairly easy manner. Thus, new designs, such as X-Core structures, are under development. In order to use existing double hull structures, using granules to fill the empty space between the outer and inner hull is a recent idea. The filling material is supposed to distribute the local load occurring during a collision, and to dissipate energy. The feasibility of this idea was already shown in a previous project, but with a focus on structural changes [3]. Thus, the modelling of granules as filling material is an open question.

In order to simulate a ship collision, it is necessary to model the granules. To resolve local behaviour, effects at particle size have to be investigated – and it is especially the breakage of particles that plays an important role. On continuum level, material models for soils and granules are known, but they are primarily used for soil modelling. Thus, the extension of the material models for the proposed use has to be verified. In order to do so, experimental tests are required to gather data for numerical modelling and verification.

The modelling on particle level is carried out by a project partner at Leibniz University Hannover, using the discrete element method (DEM). The idea in this joint project is a coupling of DEM and FEM, as shown in Figure 1.1. Here, the focus lies on the aspects mentioned before.

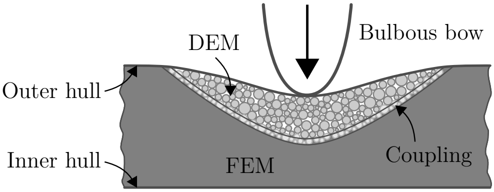

Figure 1.1: Modelling idea of a double hull filled with particles.

1.2 State of the art

With the introduction of double hull structures as a result of the oil tanker accidents in the 1980s and 1990s by the International Maritime Organization [4], experimental and numerical investigations of ship structures became more important. The increasing availability of sophisticated finite element methods for the treatment of non-linear [5, 6] and contact problems [7, 8] advanced the use of numerical tools leading to contributions to conferences regarding ship collision, beginning with the first conference on collision and grounding in 1996 [9] and in the early 2000s [10, 11, 12]. Latest results can be found in [13, 14, 15]. Despite the considerable progress in this field, there is still the risk of major uncertainties when comparing simulations and experiments, especially in the non-linear case. Therefore, experiments are still necessary to improve and validate the numerical methods [3].

In the 1990s, experimental investigations of double hull structures were performed [16] in which a scaled, simplified double hull structure was penetrated with a cone. The probe had the dimensions of 1 m × 1 m, used with penetrating cones of different radii. In [17], the experiment was numerically investigated using a commercial software product. This setup – a scaled side hull structure penetrated with a cone – can be found in many research projects [18, 19, 20]. Some of them focus on the design of the structure [21, 22, 23], while other focus on the numerical simulation [24, 25, 26]. Large-scale experiments using modified tank barges were carried out in [27, 28]. Here, it makes sense to mention the work of [29, 20, 26], which provide an introduction to experimental tests – and to the aspect of numerical simulation – similar to the experiments discussed in this thesis.

In order to improve the collision behaviour, changes in design of the double hull were investigated [30]. The aim of these changes was to achieve a higher energy dissipation due to the changed load distribution. Thus, designs such as the X-Core or Y-Core [31], see Figure 1.2, between the outer an the inner hull were investigated, revealing an improved collision behaviour [32, 33, 34]. A different approach to investigate ship-ship collisions is to consider structural changes of the bulbous bow [35, 36, 37], as was done in a previous project at the TUHH [38, 39, 3]. Using a more collision-friendly bow, i.e. due to a softer or foldable structure, the effects on the collision partner could be mitigated.

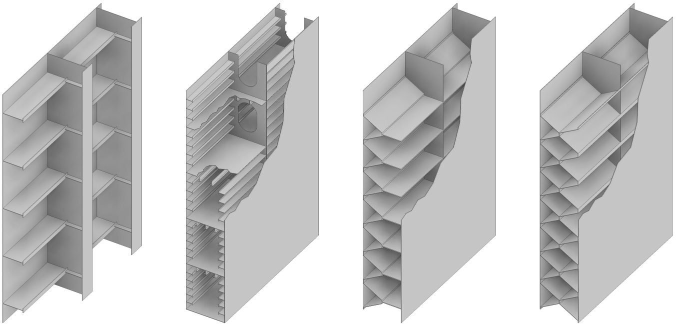

Figure 1.2: Sketch of different hull designs for a ship hull. From left to right: single hull, double hull, Y-Core, and X-Core.

In the framework of the *SideColl* [40] and the *ELKOS* [41] project at the TUHH, experimental tests on side hull structures were performed. Previous work had addressed filled structures covering foams as absorber for bridges [42], as well as collision and grounding behaviour [43]. Using an existing side hull structure and filling the void space with granules showed a better collision resistance [44], and a significant increase in energy dissipation could be observed [3].

In order to describe granules as crash absorbing material, it is possible to use a characterization on particle scale or as a homogeneous material. Single particle tests are necessary, since its parameters cannot be derived from bulk tests [45]. The characteristics of grains can be described starting with spherical particles [46], to more complex shapes such as superellipsoids [47], up to complex agglomerate structures [48]. Using spherical particles, the mechanical behaviour can be described assuming e.g. a linear-elastic or Hertzian contact law [49, 50, 51]. Since the obtained parameters can vary significantly, the introduction of a statistical representation is recommended [52, 53, 54]. For the use of a description based on the bulk behaviour of the granules – as done in this thesis – an overview over elasto-plastic models can be found in [55]. A common choice for granular material in geomechanics or soil analysis is the Mohr-Coulomb material model [56, 57, 58], see also the textbooks [59, 60]. The material behaviour is described using five parameters that can be obtained with laboratory tests [61, 62]. More advanced models, such as the hypoplastic material model, can cover behaviour such as barotropic and pyknotropy effects [63, 64, 65]. This is a non-linear model, based on the deformation rate and void ratio [66]. It has more parameters than Mohr-Coulomb – depending on its implementation – resulting in a more demanding parameter identification [67]. Recent developments include grain crushing for sand [68, 69, 70], as well as improvements regarding high confining pressures [71].

1.3 Purpose and scope of this thesis

This thesis aims at a better understanding of the interaction between granules and a surrounding structure, such as double hull structures in ship building. Since the intended use of granules is a relatively new field of application, it makes sense to start off with a selection procedure to determine the properties of different granules – looking for a material that combines several design criteria deducted in this thesis. In order to characterize the mechanical properties of granules, several tests are performed.

The experimental tests cover a major part of this thesis: from small-scale experiments to larger experimental setups representing a simplified collision scenario. To understand the stress response and breakage behaviour of granules, compression tests are performed for single grains. Based on this, a statistical evaluation is introduced to obtain a particle parameter representation based on statistical variables. This allows for an easier and more realistic modelling using particle-based methods.

To describe the bulk behaviour of the granules, experiments for parameter identification are performed. On the one hand, geotechnical experiments such as oedometer tests and triaxial tests are carried out. In doing so, material parameters for modelling with finite elements are obtained. Here the aim is to compare two different material models used in soil mechanics. In addition to this, a numerical optimization of the obtained parameters is performed, aiming for an adaption of the obtained parameters to an experimental setting with higher compression ratios. On the other hand, the parameters for the collision scenario are determined. This includes material parameters for steel plates and friction coefficients for different material pairings. It is of particular importance to determine the friction coefficients for the granules, using a modified friction test.

With all these tasks, it is possible to model and simulate a collision test. In order to validate the numerical results, experimental tests are performed. To do so, a test rig is designed, considering preliminary numerical results. This setup is built with the purpose of reuseability and comparability between different tests. Thus, the influence of granules as filling material can be determined and compared to tests and simulations without granules. Furthermore, the reuseability of the setup offers the advantage to change the design and consider stiffeners. This experimental data is used to validate the numerical model and show the improvements in collision safety gained by using granules.

Finally, a side hull structure of a vessel is investigated using the numerical data obtained before. Thus, the improvements observed from the experimental tests are transferred to a realistic scenario, also showing possible design optimizations for the use of granules as filling material, resulting in ideas for application in the maritime industry.

1.4 Outline of this thesis

The following chapter serves to summarize the basics for the material modelling. The focus is primarily on the description of the material models, reviewing the underlying constitutive equations. This is followed by an introduction to the FEM, especially to the time integration scheme. For the sake of completeness, a brief introduction to the DEM will give the reader a basic understanding of the work carried out at the project partner in Hannover – and the motivation for the second section of Chapter 3.

The first section of Chapter 3 addresses the selection of granules, regarding the requirements of this thesis. This is followed by the second section, where the properties of single grains are determined and a statistical representation is introduced, followed by a numerical example using the DEM.

Chapter 4 then introduces the experiments carried out for the parameter identification of the material models. This includes an oedometric test, a triaxial test, friction test, and a uniaxial compression test for the granules, as well as a tensile test for steel plates. The parameter identification is obtained using two approaches: on the one hand, in an analytical manner based on the test data, and, on the other hand, using numerical simulation and optimization.

After gathering all necessary data, a simplified side hull structure is introduced in Chapter 5. The experimental setup is motivated and the results are explained in detail. This is followed by the numerical evaluation in the first section of the next chapter. In the second section of Chapter 6, the application to a side hull structure of a vessel is shown. And in the last chapter, the main achievements of this work are summarized and an outlook for further research topics is presented.

2 Constitutive equations and numerical implementation

This chapter serves to summarize the constitutive equations describing the material behaviour. Two different models are used for the granules: on the one hand, the Mohr-Coulomb material model, and, on the other hand, the hypoplastic material model. Both are used in soil mechanics. This is followed by a brief description of the elasto-plastic material model used for steel parts – also focusing on the rupture mechanism, which is relevant to cover the behaviour in the double hull experiments.

The derived constitutive equations are approximated by the finite element method. The governing equations and the numerical implementation are shown in the next section. This order of appearance was chosen since the focus of this thesis lies on the material models. To cover the behaviour of the particles, the project partner in Hannover used the DEM. For the sake of completeness, a brief overview of the implementation will be given. This will help to understand the efforts in Chapter 3.2 to determine the particle properties and the presented simulations.

2.1 Constitutive equations

The modelling and simulation of the different experiments is performed using the finite element suite Abaqus [72]. Thus, the governing equations and the derivation of the material models are presented in line with the representation used in this software [73]. The Mohr-Coulomb material model is widely used in soil mechanics [61, 74, 75] and its material parameters can be derived quite simply. In contrast, the hypoplastic material model is more complex and follows a different approach [76, 77]. Here, it is implemented using user subroutines based on the implementation of [78].

2.1.1 Elasto-plastic material behaviour

The elasto-plastic material model provides the constitutive equations for the modelling of steel with rupture, as well as for the Mohr-Coulomb material – so it will be introduced here. The idea of elastoplasticity is to decompose strains into two parts,

$$\boldsymbol{\varepsilon} = \boldsymbol{\varepsilon}^e + \boldsymbol{\varepsilon}^p \qquad , \tag{2.1}$$

where $\boldsymbol{\varepsilon}^e$ describes the elastic part and $\boldsymbol{\varepsilon}^p$ describes the plastic part of the strain. Equation (2.1) is often formulated in incremental form. This allows to classify the elasto-plastic material either as rate-dependent or rate-independent of the strain rate [6]. The main aspects of plasticity are represented by a yield function f, which describes the boundary between admissible and invalid stress states. This function is dependent on stress and internal variables in general, and it describes the evolution of plastic deformation. The second main aspect is the flow rule, which governs the plastic flow. The direction of the plastic strain is defined through the derivative of the plastic potential. The third aspect is a hardening law, which defines the evolution of the yield function and the internal variables [7].

Thus, the material behaviour is dissipative and the plastic deformation is irreversible. In general, the work is converted to other types of energy such as heat during the deformation process.

As mentioned before, the Equation (2.1) is often formulated in rate form using:

$$\mathbf{D} = \mathbf{D}^e + \mathbf{D}^p = \dot{\boldsymbol{\varepsilon}}^e + \dot{\boldsymbol{\varepsilon}}^p \qquad . \tag{2.2}$$

The rate and direction of the plastic flow is defined by the flow rule:

$$\mathbf{D}^p = \dot{\lambda}\mathbf{r}\left(\boldsymbol{\sigma}, \mathbf{q}\right) \qquad , \tag{2.3}$$

where $\mathbf{r}\left(\boldsymbol{\sigma}, \mathbf{q}\right)$ is the plastic flow direction, often assumed as $\frac{\partial \Psi}{\partial \boldsymbol{\sigma}}$, with the Cauchy stress tensor $\boldsymbol{\sigma}$. Ψ describes the plastic flow potential. The variable $\dot{\lambda}$ is a consistency parameter [79], constrained by the Kuhn-Tucker complementarity conditions. The parameter $\mathbf{q}$ describes a set of internal variables.

The evolution of internal variables – often denoted as hardening law – is given by

$$\dot{\mathbf{q}} = \dot{\lambda}\mathbf{h}\left(\boldsymbol{\sigma}, \mathbf{q}\right) \qquad , \tag{2.4}$$

$\mathbf{h}$ describes the type of hardening. The plastic parameter λ may be part of the internal variables $\mathbf{q}$.

The Kuhn-Tucker complementarity conditions for the loading/unloading case are given by

$$\dot{\lambda} \geq 0, \qquad f\left(\boldsymbol{\sigma}, \mathbf{q}\right) \leq 0, \qquad \dot{\lambda} f\left(\boldsymbol{\sigma}, \mathbf{q}\right) = 0 \qquad , \tag{2.5}$$

also known as loading/unloading conditions, with the yield function $f\left(\boldsymbol{\sigma}, \mathbf{q}\right)$ as the first main aspect of plasticity.

In the case of an elastic stress state, $f\left(\boldsymbol{\sigma}, \mathbf{q}\right) < 0$ remains and, thus, $\dot{\lambda} = 0$ is given from Equation (2.5) resulting in no evolution of the internal variables $\dot{\mathbf{q}} = \mathbf{0}$ and no change in the plastic part of the deformation tensor $\mathbf{D}^p = \mathbf{0}$.

Considering the stress state on the yield surface – e.g. $f\left(\boldsymbol{\sigma}, \mathbf{q}\right) = 0$ – three cases can occur [5]. The first situation is called *elastic unloading* from a plastic state and is described by the following condition:

$$\dot{\lambda}\dot{f} = 0, \qquad \dot{f} < 0 \quad \Rightarrow \quad \dot{\lambda} = 0 \qquad . \tag{2.6}$$

Here, $\dot{\mathbf{q}} = \mathbf{0}$, and $\mathbf{D}^p = \mathbf{0}$ follows as before. Thus, the material response is elastic. The second case is given by

$$\dot{\lambda}\dot{f} = 0, \qquad \dot{f} = 0 \quad \Rightarrow \quad \dot{\lambda} = 0 \qquad , \tag{2.7}$$

and is called *neutral loading*. Even if we are in the plastic region, no plastic strains develop. The last case is given by

$$\dot{\lambda}\dot{f} = 0, \qquad \dot{f} = 0 \quad \Rightarrow \quad \dot{\lambda} > 0 \qquad , \tag{2.8}$$

referred to as *plastic flow*. Here, plastic strains arise. Thus the plastic deformation tensor changes – $\mathbf{D}^p \neq \mathbf{0}$ – as well as the internal variables: $\dot{\mathbf{q}} \neq \mathbf{0}$. The consistency condition

$$\dot{\lambda}\dot{f} = 0 \qquad , \tag{2.9}$$

is contained in these three cases.

With Equation (2.9) the evolution of $f(\boldsymbol{\sigma}, \mathbf{q})$ can be written as

$$\begin{aligned} \dot{f} &= f_{\boldsymbol{\sigma}} : \dot{\boldsymbol{\sigma}} + f_{\mathbf{q}} \cdot \dot{\mathbf{q}} \\ &= f_{\boldsymbol{\sigma}} : \mathbf{C} : [\mathbf{D} - \mathbf{D}^p] + f_{\mathbf{q}} \cdot \dot{\mathbf{q}} \\ &= f_{\boldsymbol{\sigma}} : \mathbf{C} : \mathbf{D} - \dot{\lambda}\,[f_{\boldsymbol{\sigma}} : \mathbf{C} : \mathbf{r} + f_{\mathbf{q}} \cdot \mathbf{h}] \leq 0 \end{aligned} \tag{2.10}$$

using the chain rule, where $\mathbf{C}$ is the elasticity tensor. During plastic loading, i.e. $\dot{\lambda} > 0$, the plastic flow is called *associative* if the flow direction $\mathbf{r}$ is proportional to the normal of the yield surface $f_{\boldsymbol{\sigma}}$. Otherwise it is called *non-associative*. During plastic loading, the stress has to remain on the yield surface. Thus Equation (2.10) can be solved for $\dot{\lambda}$:

$$\dot{\lambda} = \frac{f_{\boldsymbol{\sigma}} : \mathbf{C} : \mathbf{D}}{-f_{\mathbf{q}} \cdot \mathbf{h} + f_{\boldsymbol{\sigma}} : \mathbf{C} : \mathbf{r}} \qquad . \tag{2.11}$$

Taking into account that the elastic response is given by

$$\dot{\boldsymbol{\sigma}} = \mathbf{C} : \mathbf{D}^e = \mathbf{C} : (\mathbf{D} - \mathbf{D}^p) = \mathbf{C} : \left(\mathbf{D} - \dot{\lambda}\mathbf{r}\right) \tag{2.12}$$

it is possible to substitute Equation (2.11) into Equation (2.12) to obtain

$$\dot{\boldsymbol{\sigma}} = \mathbf{C} : \left(\mathbf{D} - \dot{\lambda}\mathbf{r}\right) = \mathbf{C} : \left(\mathbf{D} - \frac{f_{\boldsymbol{\sigma}} : \mathbf{C} : \mathbf{D}}{-f_{\mathbf{q}} \cdot \mathbf{h} + f_{\boldsymbol{\sigma}} : \mathbf{C} : \mathbf{r}}\mathbf{r}\right) = \mathbf{C}^{ep} : \mathbf{D} \qquad . \tag{2.13}$$

The tensor $\mathbf{C}^{ep}$ is the so-called *continuum elasto-plastic tangent modulus*. It can be rewritten with a case distinction to account for elastic as well as elasto-plastic behaviour:

$$\mathbf{C}^{ep} = \begin{cases} \mathbf{C} & \text{if } \dot{\lambda} = 0 \\ \mathbf{C} - \dfrac{(\mathbf{C} : \mathbf{r}) \otimes (f_{\boldsymbol{\sigma}} : \mathbf{C})}{-f_{\mathbf{q}} \cdot \mathbf{h} + f_{\boldsymbol{\sigma}} : \mathbf{C} : \mathbf{r}} & \text{if } \dot{\lambda} > 0 \end{cases} \qquad . \tag{2.14}$$

As can be seen, an additional part is added as subtrahend in the case of plastic flow. If the plastic flow is associative, i.e. $\mathbf{r} \sim f_{\boldsymbol{\sigma}}$, the tensor will be symmetric.

2.1.2 Mohr-Coulomb

The material properties of soils can be very different. For example, there are materials such as wet clay on the one hand – and, on the other hand, dry materials consisting of well-rounded particles, such as sand. The behaviour of the latter is similar to the granular material used in the experiments presented later. A simple approach to describe differences in material behaviour can be expressed using the angle of response [59, 60]. This can be obtained by pouring the bulk material onto a surface to obtain a cone, see Figure 2.1. Clearly, the angle of response depends on the particle shape. Often the angle of response is taken as the angle of internal friction φ. This friction angle is related to inter-grain

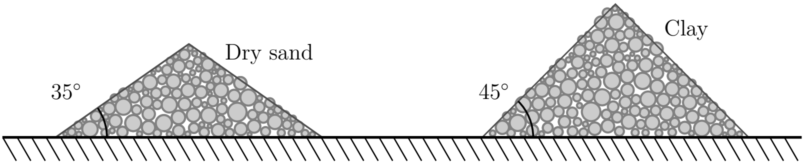

Figure 2.1: Angle of response for different materials.

interactions such as bonding between particles and cohesion due to Van der Waals' forces, capillary forces, and Coulomb forces [80].

A better understanding of the internal friction angle can be derived from an analogy: Assuming a solid material block resting on an inclined surface with the angle φ, the force when sliding occurs is given by

$$F_f = \mu F_n = F_n \cdot \tan\varphi \qquad . \tag{2.15}$$

Here F_n is the normal force and φ is the angle of friction. This can be expressed as a *yield condition*:

$$f = F_t - F_n \cdot \tan\varphi = 0 \qquad , \tag{2.16}$$

giving the force for the onset of sliding for the tangential load F_t, see Figure 2.2.

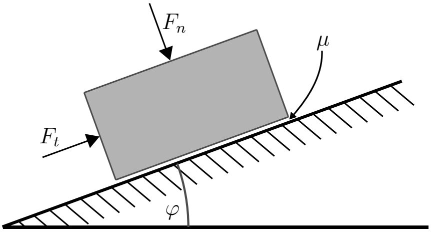

Figure 2.2: Analogy of a sliding object on an inclined surface for the friction angle.

In granules, a similar relationship holds. The yielding occurs if a critical combination of shear stress and normal stress is reached inside the material. The criterion is given by

$$\tau = c - \sigma \cdot \tan\varphi \qquad , \tag{2.17}$$

where σ is the normal stress, τ is the shear stress, and c is the cohesion of the material [81, 82, 83]. The cohesion describes the stress – without any normal pressure – which has to be reached to shear the granules [84, 61]. The criterion can be expressed in a plot of Mohr's circle for different median stresses, see Figure 2.3. The envelope of the Mohr's circles can be used to identify the parameters. In an ideal case, this envelope is a straight line, as assumed in this model, but it can generally also be a curve [85], which is observable for non-ideal materials due to effects such as grain size dependency or crushing.

Another important aspect of granular materials is the so-called *dilatancy* [86, 87]. It describes the effect of volume change due to the influence of shearing. It can be envisioned

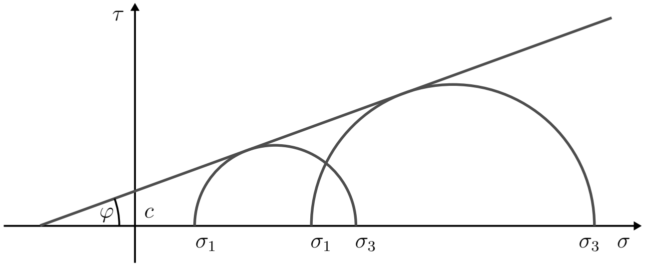

Figure 2.3: Mohr-Coulomb yield criterion obtained using Mohr's circles.

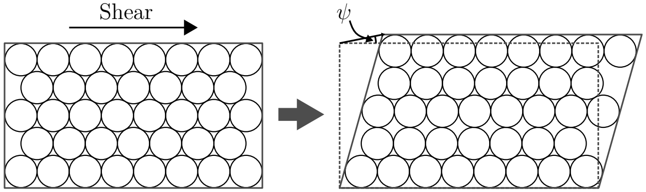

Figure 2.4: Influence of shearing to volume expressed using the dilatancy angle (adapted from [87, 88]).

due to the representation of particles, as depicted in Figure 2.4. In the case of shear stress, the dense package shifts and an expansion of the particles in vertical direction can be observed – leading to an increase in the void ratio. The change is given by the dilation angle ψ.

The model used in Abaqus is based on the Extended Mohr-Coulomb model [57]. It is written in terms of the stress invariants, and the yield surface is given by

$$F = R_{mc}\left(\Theta, \varphi\right) q - p \tan\varphi - c = 0 \tag{2.18}$$

with

$$R_{mc}\left(\Theta, \varphi\right) = \frac{1}{\sqrt{3}\cos\varphi} \sin\left(\Theta + \frac{\pi}{3}\right) + \frac{1}{3}\cos\left(\Theta + \frac{\pi}{3}\right)\tan\varphi \qquad . \tag{2.19}$$

Θ is the deviatoric polar angle defined as $\cos\left(3\Theta\right) = \left(\frac{r}{q}\right)^3$. The friction angle φ is the slope of the failure line or yield surface in the $p - R_{mc}q$ stress plane. The equivalent pressure stress is given by $p = -\frac{1}{3}\mathrm{tr}\left(\boldsymbol{\sigma}\right)$ and the von Mises equivalent stress is given by $q = \sqrt{\frac{3}{2}\left(\boldsymbol{\sigma}^d : \boldsymbol{\sigma}^d\right)}$ with the deviatoric stress tensor $\boldsymbol{\sigma}^d = \boldsymbol{\sigma} + p\mathbf{I}$ and r as invariant of the deviatoric stress tensor [89]. The Mohr-Coulomb yield surface in the principal stress plane and the deviatoric plane can be seen in Figure 2.5. As can be observed, the yield surface is an irregular hexagon in the deviatoric plane. Another point to mention is the rate-independence of this model.

The plastic potential is chosen as a smooth elliptic function in the deviatoric plane and as a hyperbolic function in the meridional stress plane, see Figure 2.6 [57]:

$$\Psi = \sqrt{\left(\varepsilon c|_0 \tan\psi\right)^2 + \left(R_{mw}\left(\Theta, e\right) q\right)^2} - p\tan\psi \qquad , \tag{2.20}$$

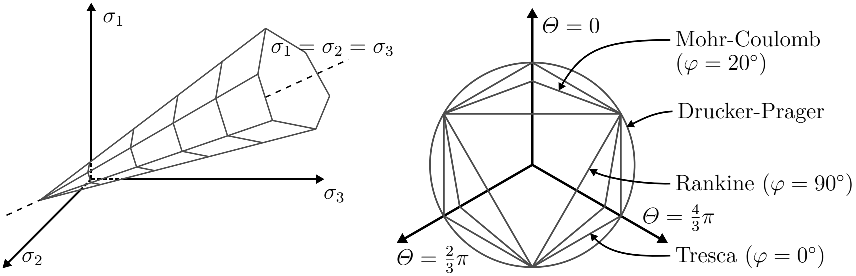

Figure 2.5: Yield surface of the Mohr-Coulomb model in the principal (left) and deviatoric (right) stress plane (adapted from [3, 88]).

where $c|_0$ is the initial cohesion yield stress and ε is a parameter defining the eccentricity, describing the rate at which the function Ψ approaches the asymptote in the meridional stress plane. The function R_{mw} is given by

$$R_{mw}(\Theta, e) = \frac{4\left(1-e^2\right)\cos^2\Theta + (2e-1)^2}{2\left(1-e^2\right)\cos\Theta + (2e-1)\sqrt{4\left(1-e^2\right)\cos^2\Theta + 5e^2 - 4e}} R_{mc}\left(\frac{\pi}{3}, \varphi\right) \quad , \tag{2.21}$$

with the parameter e describing the *out-of-roundness* between the extension meridian and the compression meridian, see Figure 2.6 on the right. Thus, it is ensured that the flow direction is uniquely defined and no numerical issues arise. Further, for high pressures, the function asymptotically approaches a linear flow potential. Since the identification of ε and e is challenging [57], the following default values are chosen in Abaqus [73]: $\varepsilon = 0.1$ is chosen for the meridional eccentricity, and the deviatoric eccentricity is calculated as $e = \frac{3-\sin\varphi}{3+\sin\varphi}$. In general the flow is non-associative, but can become close to associative depending on the variables ε and e.

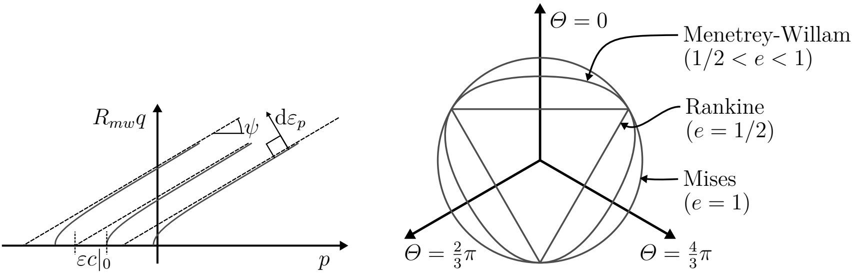

Figure 2.6: Flow potential of the Mohr-Coulomb model in the meridional (left) and the deviatoric (right) stress plane (adapted from [88]).

Furthermore, a hardening law can be formulated by modifying the potential flow [57]. Since it is primarily used to limit the load-carrying capacity near the tensile region, it is not applied here.

Thus, the Mohr-Coulomb material model needs five parameters. In the elastic region, its behaviour is described with the Young's modulus E and Poisson's ratio ν, which can be identified by compression tests. The friction angle φ, dilatancy angle ψ, and cohesion parameter c can be identified using triaxial compression tests with different confining pressures [61] using the resulting Mohr's circles, see Figure 2.3.

2.1.3 Hypoplastic material model

The idea of hypoplasticity, a class of incrementally non-linear models, is described in [64] by *Kolymbas*. The first idea of this concept was presented in [63, 66] and a general introduction can be found in [90, 91, 92].

The main idea is a model with a rate-dependent constitutive equation

$$\mathring{\boldsymbol{\sigma}} = \mathbf{h}\left(\boldsymbol{\sigma}, \mathbf{D}\right) \qquad , \tag{2.22}$$

where $\mathring{\boldsymbol{\sigma}}$ is the objective stress rate. Based on this equation, two different formulations of hypoplasticity have been developed. The first was developed by *Kolymbas* [93], while the second was developed by *Chambon et al.* [94]. Here, the approach presented in [76, 77] is used, with a user subroutine in Abaqus based on the implementation of [78].

The main challenge when developing a material model is the right choice of constraints for Equation (2.22). The constitutive material model has to fulfil the following specifications in order to be a good representation for granular behaviour: First, the material model should be applicable for large deformations. Thus, the choice of the rate of deformation $\mathbf{D}$ and the objective stress rate $\mathring{\boldsymbol{\sigma}}$ have to be chosen properly. This also includes the objectivity of the material model, such that the results are independent from the point of observation. Second, the material law has to be homogeneous in terms of stress. This is motivated by the principle of *Goldschneider* [95]. He proposes that experiments with proportional deformation paths and stress-free initial conditions results in proportional stress paths

$$\mathbf{h}\left(\lambda\boldsymbol{\sigma}, \mathbf{D}\right) = \lambda^n \mathbf{h}\left(\boldsymbol{\sigma}, \mathbf{D}\right) \qquad . \tag{2.23}$$

This also includes an asymptotic convergence to this path, if the initial state is not stress-free.

Another aspect is that the material behaviour is approximately rate- and time-independent, e.g. the strain rate performing a triaxial compression test is negligible. Thus, the material model has to have a positive homogeneity of first order in deformation rate

$$\mathbf{h}\left(\boldsymbol{\sigma}, \lambda\mathbf{D}\right) = \lambda \mathbf{h}\left(\boldsymbol{\sigma}, \mathbf{D}\right) \qquad . \tag{2.24}$$

Considering further aspects observed in the triaxial compression test, the stiffness of the material has to change after changing the load direction, e.g. from loading to unloading, see Figure 2.7. Thus, the model has to be incrementally non-linear

$$\mathbf{h}\left(\boldsymbol{\sigma}, -\mathbf{D}\right) \neq \mathbf{h}\left(\boldsymbol{\sigma}, \mathbf{D}\right) \qquad . \tag{2.25}$$

With these constraints, a first model can be proposed. It can be expressed as sum of a linear and a non-linear expression [97]

$$\mathring{\boldsymbol{\sigma}} = \mathbf{L}\left(\boldsymbol{\sigma}, \mathbf{D}\right) + \mathbf{N}\left(\boldsymbol{\sigma}\right)||\mathbf{D}|| \qquad . \tag{2.26}$$

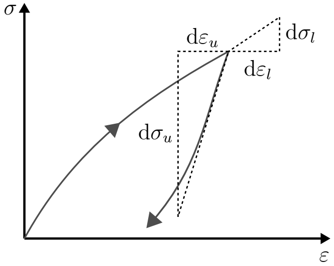

Figure 2.7: Incremental non-linearity for loading/unloading (adapted from [96, 78]).

Using the *Cayley–Hamilton* theorem [98] Equation (2.22) can be expressed using a sum of powers [99]:

$$\begin{aligned}\mathring{\boldsymbol{\sigma}} =& \alpha_0\mathbf{I} + \alpha_1\boldsymbol{\sigma} + \alpha_2\mathbf{D} + \alpha_3\boldsymbol{\sigma}^2 + \alpha_4\mathbf{D}^2 + \alpha_5\left(\boldsymbol{\sigma}\mathbf{D} + \mathbf{D}\boldsymbol{\sigma}\right)\\ &+ \alpha_6\left(\boldsymbol{\sigma}\mathbf{D}^2 + \mathbf{D}^2\boldsymbol{\sigma}\right) + \alpha_7\left(\boldsymbol{\sigma}^2\mathbf{D} + \mathbf{D}\boldsymbol{\sigma}^2\right) + \alpha_8\left(\boldsymbol{\sigma}^2\mathbf{D}^2 + \mathbf{D}^2\boldsymbol{\sigma}^2\right) \qquad ,\end{aligned} \tag{2.27}$$

with the coefficients α_i being mixed invariants of $\boldsymbol{\sigma}$ and $\mathbf{D}$.

Thus, a first variant of a hypoplastic constitutive law was proposed by [97, 100]:

$$\mathring{\boldsymbol{\sigma}} = \underbrace{C_1\left(\mathrm{tr}\boldsymbol{\sigma}\right)\mathbf{D} + C_2\frac{\mathrm{tr}\left(\boldsymbol{\sigma}\mathbf{D}\right)}{\mathrm{tr}\boldsymbol{\sigma}}\boldsymbol{\sigma}}_{\mathbf{L}(\boldsymbol{\sigma},\mathbf{D})} + \underbrace{C_3\frac{\boldsymbol{\sigma}^2}{\mathrm{tr}\boldsymbol{\sigma}}||\mathbf{D}|| + C_4\frac{\boldsymbol{\sigma}^{d^2}}{\mathrm{tr}\boldsymbol{\sigma}}||\mathbf{D}||}_{\mathbf{N}(\boldsymbol{\sigma})||\mathbf{D}||} \qquad , \tag{2.28}$$

with the deviatoric stress $\boldsymbol{\sigma}^d$ as given in Section 2.1.2. By comparing this with Equation (2.27), the coefficients a_i can be found, i.e. $a_1 = C_2\frac{\mathrm{tr}(\mathbf{T}\boldsymbol{\sigma})}{\mathrm{tr}\mathbf{T}}$. In total, four parameter C_i describe the material behaviour.

Considering experimental results, more effects than described before can be observed in soils. The barotropic behaviour – the pressure-dependent response of the soil, e.g. change in friction angle – is already included due to the homogeneity in terms of stress, see Equation (2.23), with $0 < n < 1$. Another aspect is the pyknotropy, which describes the influence of the bulk density on the soil properties. A dense sample has a higher stiffness and a visible dilatancy compared to a loose sample. To account for this behaviour, the governing equation has to be extended with an additional state variable. A suitable choice is the void ratio e, which describes the ratio between the pores and the solid part of a soil. Thus, Equation (2.22) is modified as follows

$$\mathring{\boldsymbol{\sigma}} = \mathbf{h}\left(\boldsymbol{\sigma}, \mathbf{D}, e\right) \qquad . \tag{2.29}$$

This also mitigates the problem of the so-called *ratcheting* effect, such that the accumulation of plastic deformation due to cyclic loading is considered more realistically. This results in the expression from [76]:

$$\mathring{\boldsymbol{\sigma}} = f_b f_e \frac{1}{\mathrm{tr}\left(\hat{\boldsymbol{\sigma}}^2\right)}\left[F^2\mathbf{D} + a^2\hat{\boldsymbol{\sigma}}\mathrm{tr}\left(\hat{\boldsymbol{\sigma}}\mathbf{D}\right) + f_d a F\left(\hat{\boldsymbol{\sigma}} + \hat{\boldsymbol{\sigma}}^d\right)||\mathbf{D}||\right] \qquad , \tag{2.30}$$

with the normalized stress $\hat{\boldsymbol{\sigma}} = \frac{\boldsymbol{\sigma}}{\mathrm{tr}\boldsymbol{\sigma}}$ and the normalized deviatoric stress $\hat{\boldsymbol{\sigma}}^d = \frac{\boldsymbol{\sigma}^d}{\mathrm{tr}\boldsymbol{\sigma}}$.

The parameters are given as follows:

$$a = \frac{\sqrt{3}\,(3 - \sin\varphi)}{2\sqrt{2}\sin\varphi} \tag{2.31}$$

and

$$F = \sqrt{\frac{1}{8}\tan^2\kappa + \frac{2 - \tan^2\kappa}{2 + \sqrt{2}\tan\kappa\cos(3\vartheta)}} - \frac{1}{2\sqrt{2}}\tan\kappa \tag{2.32}$$

with angles given by

$$\tan\kappa = \sqrt{3}||\hat{\boldsymbol{\sigma}}^d|| \qquad \text{and} \qquad \cos(3\vartheta) = -\sqrt{6}\frac{\operatorname{tr}\left(\hat{\boldsymbol{\sigma}}^{d3}\right)}{\left[\operatorname{tr}\left(\hat{\boldsymbol{\sigma}}^{d2}\right)\right]^{3/2}} \qquad . \tag{2.33}$$

These are derived as boundary conditions from critical states in experiments, e.g. given by the critical state surface with $\mathring{\boldsymbol{\sigma}} = \mathbf{0}$ and $\mathrm{tr}\mathbf{D} = 0$ [101, 102, 76, 103]. This can be compared to the yield surface in elastoplasticity. In the factors f_b and f_e effects related to pyknotropy are considered:

$$f_b = \frac{h_s}{n}\left(\frac{e_{i0}}{e_{c0}}\right)^{\beta}\frac{1 + e_i}{e_i}\left(\frac{-\mathrm{tr}\boldsymbol{\sigma}}{h_s}\right)^{1-n}\left[3 + a^2 - a\sqrt{3}\left(\frac{e_{i0} - e_{d0}}{e_{c0} - e_{d0}}\right)^{\alpha}\right]^{-1} \qquad , \tag{2.34}$$

$$f_e = \frac{e_c}{e}^{\beta} \qquad , \tag{2.35}$$

and the factor f_d accounts for effects related to barotropy:

$$f_d = \left(\frac{e - e_d}{e_c - e_d}\right)^{\alpha} \qquad . \tag{2.36}$$

As can be seen, the additional state variable e has an important role. The range of allowed values in a solid is limited due to the lower limit e_d and an upper limit e_i, depending on the pressure level:

$$\frac{e_i}{e_{i0}} = \frac{e_d}{e_{d0}} = \frac{e_c}{e_{c0}} = \exp\left[-\left(\frac{-\mathrm{tr}\boldsymbol{\sigma}}{h_s}\right)^{n}\right] \qquad , \tag{2.37}$$

where e_{d0} and e_{i0} are the initial experimental values of the minimum and maximum void ratio. The parameter e_c describes the critical void ratio, which is asymptotically reached in triaxial tests for different initial void ratios, but with the same lateral stress over a long shear process. The evolution of the void ratio is given by

$$\dot{e} = (1 + e)\,\mathrm{tr}\mathbf{D} \qquad . \tag{2.38}$$

The granule hardness h_s and the exponent n can be determined in oedometric compression tests. h_s represents the stress-dependent stiffness of the granular material. The exponents α and β are also to be determined using basic geotechnical experiments [104, 67, 105].

Concluding, eight material parameters have to be determined: the angle of internal friction φ (which corresponds to the parameter used for the Mohr-Coulomb material model), the granule hardness h_s (which is the only parameter having a dimension) and the related exponent n – plus the initial void ratios for three different states e_{d0}, e_{c0}, and e_{i0} and the two exponents α and β.

2.1.4 Damage modelling for elasto-plastic material

In order to simulate steel parts and their rupture behaviour, a damage model has to be chosen. Here, the *ductile damage* model from Abaqus is used. The damage behaviour can be split into two parts – starting with the damage initiation criterion, describing the onset of damage, followed by the damage evolution, which governs the degeneration of the material.

The idea of the ductile damage model can be described using a stress-strain curve, see Figure 2.8 [73]. In the linear elastic region, the behaviour is described by the Young's modulus E_0 until the yield stress σ_y is reached. If the material starts to yield, the plastic deformation is described using stress-strain values as tabular input, e.g. from tension tests. Here, the stress-strain relationship is described using a power law in the plastic regime [107, 106]:

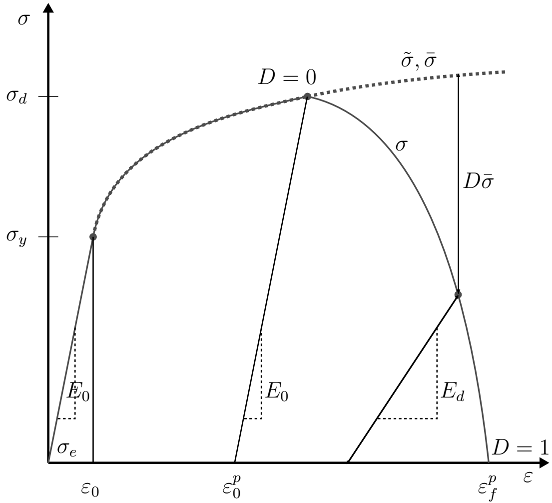

Figure 2.8: Damage modelling in Abaqus (adapted from [88, 106]).

$$\tilde{\sigma}\left(\varepsilon^p\right) = C \cdot \left(\varepsilon_0 + \varepsilon^p\right)^n \qquad , \tag{2.39}$$

where C and n are material-dependent parameters. The initial state ε_0 is given at the yield stress σ_y with $\varepsilon_0 = \sqrt[n]{\sigma_y/C}$. Staying in the plastic region – without damage – the Young's modulus does not change. Thus, unloading in the plastic region results in a parallel path to the linear elastic path. In total, the material response is described as a combination of the elastic part σ_e and the response in the plastic regime, see Equation (2.39) [73].

The strain ε_0^p – measured in the plastic regime – determines the onset of damage. The evolution of the damage is driven by the damage variable D, which decreases the Young's modulus and the stress:

$$E_d = (1 - D)\, E_0 \qquad \text{and} \qquad \sigma = (1 - D)\, \bar{\sigma} \qquad , \tag{2.40}$$

where $\bar{\sigma}$ describes the stress-strain curve, in the elastic and the plastic regime, in the absence of damage. The damage variable increases with developing plastic strain, until the stiffness of a finite element is fully degenerated at ε^p_f. In order to describe the evolution of the damage variable, several options are available, i.e. linear, exponential, polynomial, or user-defined curves can be specified. Here, a polynomial curve is chosen [108, 106]:

$$D = f\left(\bar{u}^p\right) = \frac{1}{\left(\bar{u}^p_f\right)^m} \cdot \left(\bar{u}^p\right)^m \qquad . \tag{2.41}$$

Thus, the failure point is defined by the effective plastic displacement $\bar{u}^p_f$ and the shape of the curve by the exponent m. The term $\bar{u}^p_f$ is introduced as normalized plastic displacement, taking the strain and the element geometry into consideration. Thus, the mesh dependency shall be reduced [73]. Using shell elements, $\bar{u}^p_f$ is a characteristic length in the reference surface. Aspect ratios close to unity are recommended for elements, see [88]. This mitigates a mesh dependency, which may occur anyway.

Ductile damage is mainly described by two phenomena [109]: firstly, failure due to the growth of small voids or inclusions in the crystalline structure of metals, see Figure 2.9 and, secondly, shearing due to localisation of shear stress. The model used here assumes that the equivalent plastic strain $\bar{\varepsilon}^p_D$ is a function of stress triaxiality η and strain rate:

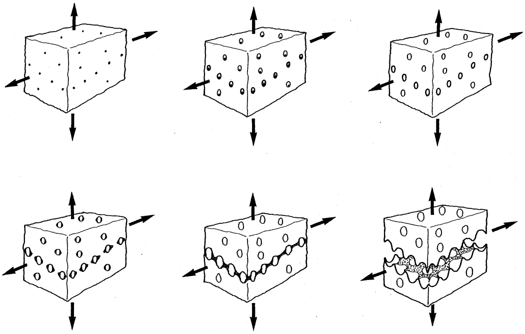

Figure 2.9: Schematic crack growth mechanism using the ductile damage model (from [22]).

$$\bar{\varepsilon}^p_D\left(\eta, \dot{\varepsilon}^p\right) \quad \text{with} \quad \eta = \frac{-p}{q} \qquad , \tag{2.42}$$

with p and q defined in Section 2.1.2. The damage initiation occurs when the following condition is fulfilled:

$$\omega_D = \int \frac{\mathrm{d}\bar{\varepsilon}^p}{\bar{\varepsilon}^p_D\left(\eta, \dot{\varepsilon}^p\right)} = 1 \qquad . \tag{2.43}$$

It is tracked by calculating the increment $\Delta\omega_D$ at each time step and accumulating it over the simulation. To sum up, the following parameters are used to model steel until rupture: the Young's modulus E and Poisson ratio ν in the elastic region, and the factor C and exponent n to describe the behaviour in the plastic regime. For the damage initiation, the equivalent plastic strain $\bar{\varepsilon}^p_D$ drives the onset of damage, while the evolution is regulated by the amount of plastic deformation $\bar{u}^p_f$ and an exponent m for the shape of the damage path.

2.2 Numerical implementation

In order to simulate the experiments, a numerical method has to be chosen. Since the focus in this thesis is on the material behaviour, the constitutive equations were already introduced in the previous section. Using a continuous approach for numerical modelling, the FEM will be introduced in more detail, followed by a very brief overview of the DEM. Further details on the coupling with DEM can be found in [110, 111, 112].

2.2.1 Finite element method

To describe the behaviour of a deformable body, its kinematic relations have to be considered in spatial and temporal discretization – beginning with the governing equations of kinematics, where the motion of a deformable body is described. This is followed by the description of the equilibrium conditions, where effects of external forces on a body are included. This is followed by transforming the equilibrium equations into a weak form. By linearising the weak form, the representation used in the FEM is obtained. As the last aspect, the constitutive equations have to be considered to describe the material response to a load. For a closer and more detailed insight into the derivation of the FEM, please refer to [5, 6], on which this section is based.

Kinematics

In order to describe the kinematic relations of a deformable structure, a body Ω in the three-dimensional space is considered. The domain of its *initial configuration* at the time $t = 0$ is denoted by Ω_0, as depicted in Figure 2.10. To describe the motion of the body, a *reference configuration* is needed. Here, the initial configuration acts as the reference configuration. The domain of the *current configuration* of the body in Figure 2.10 is denoted by Ω. Its boundary is given by Γ. The motion of the body is described by

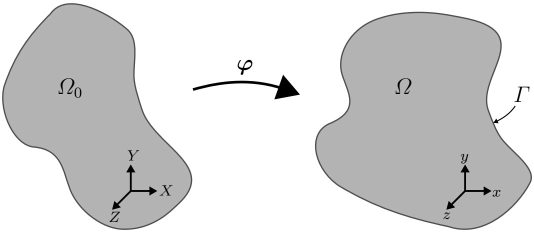

Figure 2.10: Reference configuration Ω_0 and current configuration Ω of a deformable body.

$$\mathbf{x} = \boldsymbol{\varphi}(\mathbf{X}, t) \qquad , \tag{2.44}$$

where $\mathbf{x}$ defines the location of the particle or material point $\mathbf{X}$ at the time t. Thus, the function $\boldsymbol{\varphi}$ maps points in the reference configuration $\mathbf{X}$ to the corresponding points in the current configuration $\mathbf{x}$ at time t. In agreement with the common nomenclature, lowercase variables refer to the current configuration and capital letters are used for the reference configuration.

To describe the local deformation, the *deformation gradient* is introduced:

$$\mathbf{F} = \frac{\partial \mathbf{x}}{\partial \mathbf{X}} \qquad . \tag{2.45}$$

Considering an infinitesimal line element $\mathrm{d}\mathbf{X}$ in the reference configuration, the corresponding element $\mathrm{d}\mathbf{x}$ is given by:

$$\mathrm{d}\mathbf{x} = \mathbf{F}\mathrm{d}\mathbf{X} \qquad , \tag{2.46}$$

and since $\mathbf{F}$ is regular, $\mathrm{d}\mathbf{X}$ can be determined using the inverse of $\mathbf{F}$. Thus, the determinant of the deformation gradient $\mathbf{F}$ will be denoted as J and is called *Jacobian*:

$$J = \det(\mathbf{F}) \neq 0 \qquad . \tag{2.47}$$

The fact that $\mathbf{F}$ is regular implies that $J \neq 0$, which holds since the mapping function $\boldsymbol{\varphi}$ has to be invertible. Also, $J > 0$ has to be fulfilled to avoid self-penetration of the body. A useful application of the Jacobian determinant is the relation of integrals in the two configurations:

$$\int_{\Omega} (\cdot)\, \mathrm{d}\Omega = \int_{\Omega_0} (\cdot)\; J\, \mathrm{d}\Omega_0 \qquad . \tag{2.48}$$

Balance equations

Every physical system has to fulfil the balance equations that arise from conservation laws. Four fundamental equations are considered here. The conservation of mass, balance of linear and angular momentum, as well as the conservation of energy. These equations are often expressed as differential equations.

The first law is given by the conservation of mass. It is assumed that the mass of a body does not change over time, since there is no flow over its boundary and no mass to energy conversion.

$$\frac{\mathrm{D}m}{\mathrm{D}t} = \frac{\mathrm{D}}{\mathrm{D}t}\int_{\Omega} \rho(\mathbf{x},t)\, \mathrm{d}\Omega = \frac{\mathrm{D}}{\mathrm{D}t}\int_{\Omega_0} \rho_0(\mathbf{X})\, \mathrm{d}\Omega_0 = 0 \qquad , \tag{2.49}$$

with $\rho(\mathbf{x},t)$ as the density of the body and $\rho_0(\mathbf{X})$ as the density in the reference configuration. Since there is no change in mass over time, the following applies:

$$\int_{\Omega} \rho(\mathbf{x},t)\, \mathrm{d}\Omega = \int_{\Omega_0} \rho_0(\mathbf{X})\, \mathrm{d}\Omega_0 = \text{const.} \tag{2.50}$$

Applying Equation (2.48) to transform the left-hand side of the equation above to the reference domain leads to:

$$\int_{\Omega_0} \left[\rho(\mathbf{x},t)\, J - \rho_0(\mathbf{X})\right] \mathrm{d}\Omega_0 = 0 \qquad . \tag{2.51}$$

Since this has to hold for any arbitrary subdomain of the body, it can be expressed as:

$$\rho J = \rho_0 \qquad . \tag{2.52}$$

The balance of linear momentum is given by Newton's second law of motion. It states that the change in linear momentum relates to the sum of forces acting on the body. Thus

$$\frac{\mathrm{D}\mathbf{p}(t)}{\mathrm{D}t} = \frac{\mathrm{D}}{\mathrm{D}t}\int_{\Omega} \rho\mathbf{v}(\mathbf{x},t)\, \mathrm{d}\Omega = \int_{\Omega} \rho\mathbf{b}(\mathbf{x},t)\, \mathrm{d}\Omega + \int_{\Gamma} \mathbf{t}(\mathbf{x},t)\, \mathrm{d}\Gamma = \mathbf{f}(t) \qquad , \tag{2.53}$$

where $\mathbf{p}(t)$ is the linear momentum and $\mathbf{f}(t)$ is the sum of external forces – with the body forces $\rho\mathbf{b}$ and the surface tractions $\mathbf{t}$ integrated over the body Ω and surface Γ, respectively, while $\mathbf{v}(\mathbf{x},t)$ is the velocity. Using Cauchy's theorem – $\mathbf{t} = \boldsymbol{\sigma}\mathbf{n}$ – and Gauss's divergence theorem, leads to:

$$\begin{aligned}\frac{\mathrm{D}}{\mathrm{D}t}\int_\Omega \rho\mathbf{v}(\mathbf{x},t)\,\mathrm{d}\Omega &= \int_\Omega \rho\mathbf{b}(\mathbf{x},t)\,\mathrm{d}\Omega + \int_\Gamma \boldsymbol{\sigma}(\mathbf{x},t)\,\mathbf{n}(\mathbf{x},t)\,\mathrm{d}\Gamma \\ &= \int_\Omega \rho\mathbf{b}(\mathbf{x},t)\,\mathrm{d}\Omega + \int_\Omega \operatorname{div}\boldsymbol{\sigma}(\mathbf{x},t)\,\mathrm{d}\Omega \qquad ,\end{aligned} \tag{2.54}$$

with the outer surface normal $\mathbf{n}$ and the Cauchy stress tensor $\boldsymbol{\sigma}$. As before, this must hold for an arbitrary subdomain of the body, resulting in the differential form for the balance of linear momentum in the current configuration:

$$\rho\frac{\mathrm{D}\mathbf{v}}{\mathrm{D}t} = \operatorname{div}\boldsymbol{\sigma} + \rho\mathbf{b} \qquad , \tag{2.55}$$

which is also called *momentum equation*.

The conservation of angular momentum – which means that the change of angular momentum is equal to the total moment of the body and traction forces with respect to the same observation point – is given by

$$\frac{\mathrm{D}}{\mathrm{D}t}\int_\Omega \mathbf{x}(t)\times\rho\mathbf{v}(\mathbf{x},t)\,\mathrm{d}\Omega = \int_\Omega \mathbf{x}(t)\times\rho\mathbf{b}(\mathbf{x},t)\,\mathrm{d}\Omega + \int_\Gamma \mathbf{x}(t)\times\mathbf{t}(\mathbf{x},t)\,\mathrm{d}\Gamma \qquad , \tag{2.56}$$

where $\mathbf{x}(t)$ is the vector to the origin used as observation point. This conservation law leads to the following condition for the Cauchy stress tensor:

$$\boldsymbol{\sigma} = \boldsymbol{\sigma}^T \qquad . \tag{2.57}$$

Thus, the Cauchy stress tensor is symmetric, which implies a reduction to six dependent variables in the three-dimensional space.

Weak form of equilibrium

In order to analyse the mechanical equilibrium using FEM, it is necessary to discretize Equation (2.55). From the physical point of view, the momentum equation has to be fulfilled in the entire body. Discretizing the domain and introducing an approximate solution will result in a remaining residual $\mathbf{r}$:

$$\operatorname{div}\boldsymbol{\sigma} + \rho\mathbf{b} - \rho\frac{\mathrm{D}\mathbf{v}}{\mathrm{D}t} = \mathbf{r} \qquad , \tag{2.58}$$

which is the *strong form* of equilibrium. The residual will be weighted with a test function $\boldsymbol{\eta}$. To do so, Equation (2.58) has to be multiplied with the test function and integrated over the domain. This leads to

$$\int_\Omega \rho\frac{\mathrm{D}\mathbf{v}}{\mathrm{D}t}\cdot\boldsymbol{\eta}\,\mathrm{d}\Omega = \int_\Omega \operatorname{div}\boldsymbol{\sigma}\cdot\boldsymbol{\eta}\,\mathrm{d}\Omega + \int_\Omega \rho\mathbf{b}\cdot\boldsymbol{\eta}\,\mathrm{d}\Omega \qquad . \tag{2.59}$$

Using the product rule, the first term of the right-hand side can be expanded, which gives

$$\int_\Omega \rho\frac{\mathrm{D}\mathbf{v}}{\mathrm{D}t}\cdot\boldsymbol{\eta}\,\mathrm{d}\Omega = \int_\Omega \operatorname{div}(\boldsymbol{\sigma}\boldsymbol{\eta})\,\mathrm{d}\Omega - \int_\Omega \boldsymbol{\sigma}\cdot\operatorname{grad}\boldsymbol{\eta}\,\mathrm{d}\Omega + \int_\Omega \rho\mathbf{b}\cdot\boldsymbol{\eta}\,\mathrm{d}\Omega \qquad , \tag{2.60}$$

taking into account the symmetry of the stress tensor from Equation (2.57). Using the Gauss's divergence theorem, the first term of the right-hand side can be written as

$$\int_{\Omega} \operatorname{div}(\boldsymbol{\sigma}\boldsymbol{\eta})\,\mathrm{d}\Omega = \int_{\Gamma} (\boldsymbol{\sigma}\boldsymbol{\eta}) \cdot \mathbf{n}\,\mathrm{d}\Gamma = \int_{\Gamma} (\boldsymbol{\sigma}\mathbf{n}) \cdot \boldsymbol{\eta}\,\mathrm{d}\Gamma = \int_{\Gamma} \bar{\mathbf{t}} \cdot \boldsymbol{\eta}\,\mathrm{d}\Gamma \qquad , \tag{2.61}$$

taking into account the symmetry of the stress tensor and Cauchy's theorem, where $\bar{\mathbf{t}}$ are the tractions on the boundary. Thus, the *weak form* of the linear momentum equation is obtained:

$$\int_{\Omega} \rho \frac{\mathrm{D}\mathbf{v}}{\mathrm{D}t} \cdot \boldsymbol{\eta}\,\mathrm{d}\Omega + \int_{\Omega} \boldsymbol{\sigma} \cdot \operatorname{grad}\boldsymbol{\eta}\,\mathrm{d}\Omega = \int_{\Omega} \rho\mathbf{b} \cdot \boldsymbol{\eta}\,\mathrm{d}\Omega + \int_{\Gamma} \bar{\mathbf{t}} \cdot \boldsymbol{\eta}\,\mathrm{d}\Gamma \qquad , \tag{2.62}$$

which is also known as the *principle of virtual work*. Since the Cauchy stress tensor is symmetric, the following relation holds:

$$\boldsymbol{\sigma} \cdot \operatorname{grad}\boldsymbol{\eta} = \boldsymbol{\sigma} \cdot \operatorname{sym}(\operatorname{grad}\boldsymbol{\eta}) = \boldsymbol{\sigma} \cdot \boldsymbol{\varepsilon}(\boldsymbol{\eta}) \qquad , \tag{2.63}$$

where $\boldsymbol{\varepsilon}(\boldsymbol{\eta})$ represent the virtual strain. Thus, Equation (2.62) can be written as

$$\int_{\Omega} \rho \frac{\mathrm{D}\mathbf{v}}{\mathrm{D}t} \cdot \boldsymbol{\eta}\,\mathrm{d}\Omega + \int_{\Omega} \boldsymbol{\sigma} \cdot \boldsymbol{\varepsilon}(\boldsymbol{\eta})\,\mathrm{d}\Omega = \int_{\Omega} \rho\mathbf{b} \cdot \boldsymbol{\eta}\,\mathrm{d}\Omega + \int_{\Gamma} \bar{\mathbf{t}} \cdot \boldsymbol{\eta}\,\mathrm{d}\Gamma \qquad . \tag{2.64}$$

Spatial discretization

For the sake of simplicity, the linear case is considered in order to discretize the body, thus assuming $\Omega_0 \approx \Omega$. The domain Ω is divided into non-overlapping finite elements Ω_e. The domain thus consists of n_e finite elements:

$$\Omega = \bigcup_{e=1}^{n_e} \Omega_e \qquad . \tag{2.65}$$

For each element, the displacement is approximated using

$$\mathbf{u}_{exact} \approx \mathbf{u}_{appr} = \mathbf{N}\mathbf{U}_e \qquad , \tag{2.66}$$

with $\mathbf{N}$ defining the matrix of shape functions inside an element in the element local $\boldsymbol{\xi}$-coordinate system. Therefore, the approximated displacement $\mathbf{u}_{appr}$ is given by a matrix-vector multiplication with the vector $\mathbf{U}_e$, which contains the coefficients for the shape functions. The same ansatz can be chosen for the velocity $\mathbf{v}$ and acceleration $\mathbf{a}$, as well as for the test function $\boldsymbol{\eta}$.

For the discretization of the weak form, it is common to apply the *Voigt* notation, writing $\boldsymbol{\sigma}$ as a vector. This simplifies the algorithmic implementation and takes advantage of the symmetry of $\boldsymbol{\sigma}$. Substituting these into the first term of the weak form of Equation (2.64) leads to:

$$\int_{\Omega} \rho \frac{\mathrm{D}\mathbf{v}}{\mathrm{D}t} \cdot \boldsymbol{\eta}\,\mathrm{d}\Omega = \bigcup_{e=1}^{n_e} \mathbf{H}_e^T \underbrace{\left[\int_{\Omega_e} \rho\mathbf{N}^T\mathbf{N} \det\mathbf{J}\,\mathrm{d}\boldsymbol{\xi}\right]}_{\mathbf{M}} \frac{\mathrm{D}\mathbf{V}_e}{\mathrm{D}t} \qquad , \tag{2.67}$$

with the Jacobian matrix **J**, relating to the element local coordinate system, using Equation (2.48). The second term of the left-hand side of Equation (2.64) is given by

$$\int_{\Omega} \boldsymbol{\sigma} \cdot \boldsymbol{\varepsilon}(\boldsymbol{\eta})\, \mathrm{d}\Omega = \bigcup_{e=1}^{n_e} \mathbf{H}_e^T \underbrace{\left[\int_{\Omega_e} \mathbf{B}^T \mathbf{C} \mathbf{B} \det \mathbf{J}\, \mathrm{d}\boldsymbol{\xi}\right]}_{\mathbf{K}} \mathbf{U}_e \qquad , \tag{2.68}$$

with the elasticity tensor **C** for the linear elastic material behaviour from Section 2.1.1. The strain is expressed with $\boldsymbol{\varepsilon}(\mathbf{u}_{appr}) = \mathbf{B}\mathbf{U}_e$ and $\boldsymbol{\varepsilon}(\boldsymbol{\eta}) = \mathbf{B}\mathbf{H}_e$ respectively. The matrix **B** is called strain-displacement matrix. The right-hand side of Equation (2.64) can be expressed as

$$\int_{\Omega} \rho \mathbf{b} \cdot \boldsymbol{\eta}\, \mathrm{d}\Omega + \int_{\Gamma} \bar{\mathbf{t}} \cdot \boldsymbol{\eta}\, \mathrm{d}\Gamma = \bigcup_{e=1}^{n_e} \mathbf{H}_e^T \underbrace{\left[\int_{\Omega_e} \mathbf{N}^T \rho \mathbf{b} \det \mathbf{J}\, \mathrm{d}\boldsymbol{\xi} + \int_{\Gamma_e} \mathbf{N}^T \bar{\mathbf{t}}\, \mathrm{d}\Gamma\right]}_{\mathbf{f}} \qquad . \tag{2.69}$$

To obtain a better physical interpretation, the time-independent terms of the equations above can be summarized as mass matrix **M**, stiffness matrix **K**, and load vector **f**. For further details, the reader is referred to the textbooks mentioned in the introduction of this chapter. It is also possible to include damping effects to obtain the standard FEM representation:

$$\mathbf{M}\ddot{\mathbf{u}} + \mathbf{C}\dot{\mathbf{u}} + \mathbf{K}\mathbf{u} = \mathbf{f} \qquad , \tag{2.70}$$

where $\ddot{\mathbf{u}} = \mathbf{a}$, $\dot{\mathbf{u}} = \mathbf{v}$, and with the damping matrix **C**. For the non-linear case, a detailed introduction is given in the textbooks mentioned at the beginning of this section.

Time integration

There are different approaches to solve the equation of motion in the temporal domain. In this thesis, the explicit time integration method is used. For details other methods, such as implicit time integration or modal analysis, the interested reader is referred to the textbooks [7, 5, 6].

The equation of motion (2.70) will be evaluated at distinct time points t_i to obtain the displacement at the next time step $\mathbf{u}_{i+1}$ at time t_{i+1}:

$$\mathbf{M}\ddot{\mathbf{u}}_i + \mathbf{C}\dot{\mathbf{u}}_i + \mathbf{K}\mathbf{u}_i = \mathbf{f}_i \qquad . \tag{2.71}$$

For the sake of simplicity, it is assumed that the time increment Δt will be constant over the solution, $t_{i+1} = t_i + \Delta t$, allowing to express the velocity and acceleration as central differences:

$$\dot{\mathbf{u}}_i = \frac{1}{2\Delta t}\left(\mathbf{u}_{i+1} - \mathbf{u}_{i-1}\right) \tag{2.72}$$

$$\ddot{\mathbf{u}}_i = \frac{1}{\Delta t^2}\left(\mathbf{u}_{i+1} - 2\mathbf{u}_i + \mathbf{u}_{i-1}\right) \qquad . \tag{2.73}$$

Inserting these into Equation (2.71) and rearranging terms leads to:

$$\left(\frac{1}{\Delta t^2}\mathbf{M} + \frac{1}{2\Delta t}\mathbf{C}\right)\mathbf{u}_{i+1} = \mathbf{f}_i - \left(\mathbf{K} - \frac{2}{\Delta t^2}\mathbf{M}\right)\mathbf{u}_i - \left(\frac{1}{\Delta t^2}\mathbf{M} - \frac{1}{2\Delta t}\mathbf{C}\right)\mathbf{u}_{i-1} \qquad . \tag{2.74}$$

Thus, the new displacement can be calculated based on data from previous time steps, followed by the calculation of the velocity and acceleration. The damping matrix $\mathbf{C}$ is often represented using a combination of $\mathbf{M}$ and $\mathbf{K}$ – called Rayleigh damping – as a mathematical approach. This results in a simplification in the numerical solution process and is therefore favourable in FEM. In a non-linear system, the stiffness of the system has to be evaluated in every time increment which is included in the internal load vector. The internal load vector $\mathbf{f}_a$ is assembled in such a way that the contributions from the individual elements are taken into account, so that it is not necessary to calculate a global stiffness matrix $\mathbf{K}$. This leads to

$$\mathbf{M}\ddot{\mathbf{u}}_i = \mathbf{f}_i - \mathbf{f}_{a,i} \tag{2.75}$$

in correspondence with Equation (2.71). Using a diagonal lumped mass matrix, the inversion of $\mathbf{M}$ is computationally efficient to obtain the new acceleration

$$\ddot{\mathbf{u}}_i = \mathbf{M}^{-1}_{lumped}\left(\mathbf{f}_i - \mathbf{f}_{a,i}\right) \qquad . \tag{2.76}$$

The new velocity and displacement can then be calculated using a central difference scheme with variable time step size Δt_i and half steps for the velocity from the previous increment for improved performance. Thus, the velocity is given by

$$\dot{\mathbf{u}}_{i+\frac{1}{2}} = \dot{\mathbf{u}}_{i-\frac{1}{2}} + \frac{\Delta t_{i+1} + \Delta t_i}{2}\ddot{\mathbf{u}}_i \tag{2.77}$$

and the displacement is given by

$$\mathbf{u}_{i+1} = \mathbf{u}_i + \Delta t_{i+1}\dot{\mathbf{u}}_{i+\frac{1}{2}} \qquad . \tag{2.78}$$

For the start of the central difference method, the mean velocity $\dot{\mathbf{u}}_{0-\frac{1}{2}}$ needs to be defined. This is obtained inserting the initial conditions $\dot{\mathbf{u}}_0$ and $\ddot{\mathbf{u}}_0$ into a backward step:

$$\dot{\mathbf{u}}_{0-\frac{1}{2}} = \dot{\mathbf{u}}_0 - \frac{\Delta t_0}{2}\ddot{\mathbf{u}}_0 \qquad . \tag{2.79}$$

The time step size Δt is determined using

$$\Delta t \leq \frac{2}{\omega_{max}}\left(\sqrt{1+\zeta^2} - \zeta\right) \qquad , \tag{2.80}$$

where ω_{max} is the highest eigenvalue in the system and ζ is an artificial damping factor to control high frequency oscillations.

Constitutive equations

In order to solve a problem in continuum mechanics, the material response of the body to its loads has to be known. The constitutive equations take part of this. Since the material behaviour can vary from simple to complex – also depending on the scale of interest – constitutive equations are an approximation to real physical behaviour. Thus, the stress inside the body can depend on various contributing factors such as strain, deformation rate, stress, etc. The constitutive equations used in this thesis have already been introduced in Section 2.1.

2.2.2 Discrete element method

In order to provide an overview of the work done in the underlying project, a brief introduction on the concept of the discrete element method will be given. The interested reader is referred to [113, 114, 50, 115] for a general overview of the DEM. The method used in Chapter 3.2.3 is described in detail in [110, 74, 58].

The behaviour of the granules is modelled at grain scale, each of them is represented by a particle. The particles are assumed to be rigid elements and can interact with surrounding particles, while the translational and rotational degrees of freedom are assigned to the centre of their mass. The interaction of particles is governed by their distance to their neighbour particles. An overlap results in contact forces, such as normal and tangential forces and torque in the case of frictional contact. The balance of linear momentum for a particle i is given by

$$m_i \ddot{\mathbf{x}}_i = \sum_{j=1}^{N_C^i} \mathbf{f}_{ij} + \mathbf{g}_i \qquad , \tag{2.81}$$

where m_i is the mass of a particle, $\ddot{\mathbf{x}}_i$ its acceleration, $\mathbf{g}_i$ the gravitational force, and $\mathbf{f}_{ij}$ the force exerted on particle i by particle j, with the amount of contacts N_C^i for the considered particle. The balance of angular momentum is given by

$$\sum_{j=1}^{N_C^i} \mathbf{m}_{ij} = \mathbf{J}_i \dot{\boldsymbol{\omega}}_i \tag{2.82}$$

in the case of spherical particles. The moment is given by $\mathbf{m}_{ij}$ due to the inertia tensor $\mathbf{J}_i$ and the rotational velocity $\boldsymbol{\omega}_i$.

The choice of a contact model to calculate $\mathbf{f}_i$ has a high impact on the accuracy and computational cost. The force acting on a particle can be divided into a normal and a tangential part:

$$\mathbf{f}_i = \mathbf{f}_i^n + \mathbf{f}_i^t \qquad . \tag{2.83}$$

Simple methods such as a linear relation between the penetration depth and force are not able to cover the material behaviour exactly [116]. Thus, more advanced methods such as the Hertzian contact law are more suitable, which is also be used in this DEM implementation and in the characterization of particles – see Section 3.2, Equation (3.1). Additionally, a model for rolling resistance has to be chosen and crushing and damping has to be considered. The governing equations are integrated in the time domain using an explicit time integration method, with a global-local framework to increase the computational efficiency [111].

In the concurrent work by the project partner, a DEM framework based on the work of [74] is used. For more details regarding the DEM implementation, please refer to [116, 111, 112].

3 Selection of granules and description of single grains

The main emphasis of this chapter is on the granules. The first section deals with the choice of granules. After applying the given requirements, the focus will be on the second section. There, a reduced amount of granules are investigated in detail. In doing so, particle parameters are determined using a single particle compression test. Thereafter, a statistical model is derived to represent the variety of the observed parameter distribution. The chapter concludes with a numerical example showing the capabilities of the DEM from the project partner.

3.1 Selection of granules

The material used inside a double hull structure has to fulfil mechanical, environmental, and economical requirements. The work of Schöttelndreyer [3] contains a list of requirements – including the following points, in order of importance: toxicity; fire, explosion, and health protection; pumpability; hydrophobicity; and bulk density. For a detailed discussion about these parameters, see [3]. Considering further aspects, the following list is obtained:

1. toxicity
2. price per m^3
3. fire, explosion, and health protection
4. pumpability
5. chemical interaction (e.g. hydrophobicity)
6. bulk density
7. buoyancy
8. recyclability and environmental friendliness of production process

An additional factor to be taken into account is the price per volume. Comparing the filling of the structure with other approaches to increase the collision safety, it has to be economically worthwhile. The costs for installation – as well as the maintenance costs – are dependent on the purpose of use. On the one hand, it would be possible to fill the entire structure. In this case, an enormous amount of granules would be needed – and the price, and other aspects such as the bulk density, would become critical. On the other hand, it is possible to fill only the important parts of the structure, reducing the importance of this aspect.

Additional environmental aspects are considered in the last two points. The buoyancy is coupled with point 4 and 5. In the case of an accident, the particles create an uplift and can be collected from the surface if they are discharged from the double hull.

Although this was already discussed in [3], it makes sense to consider the aspect of pumpability here too, as it is one of the main reasons for choosing granules as filling material. This is due to two factors. First, the material should be applicable to existing ships. Secondly, the material has to be removable for inspection purposes.

In view of this catalogue of requirements, the most promising granules can be found in geoengineering. More specifically, they are expanded granules made of clay and glass, as well as perlite and diatomaceous earth. Due to the exclusion of organic materials, Advanced Pore Morphology foam [117] is considered as an additional example for a material that is already used as crash absorber in other application fields [118, 119].

To reduce the expenses for the experiments, a uniaxial compression test is used to break down the selection to one granular material of primary interest. The setup is shown in Figure 3.1. The particles of interest are subjected to a uniaxial compression load in a cylinder with a diameter of 181 mm. The diameter/height ratio is 1, so the particles are filled into the cylinder up to a height of 181 mm. Two forces are measured. First, the applied force at the upper stamp – which can be interpreted as the force applied to the structure of a ship by the bulbous bow of a colliding ship. Secondly, the force is measured at the supporting stamp at the bottom. As can be seen in the Figure 3.1, part of the applied force can be transmitted to the housing via the aluminium cylinder. Thus, the two measured forces may not be equal. The difference can be interpreted as an indicator of how well the granules can distribute and dissipate the load. The less force is transferred

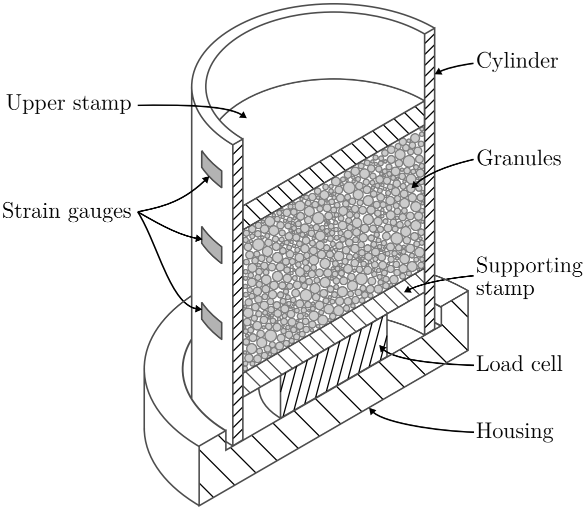

Figure 3.1: Sketch of uniaxial compression test.

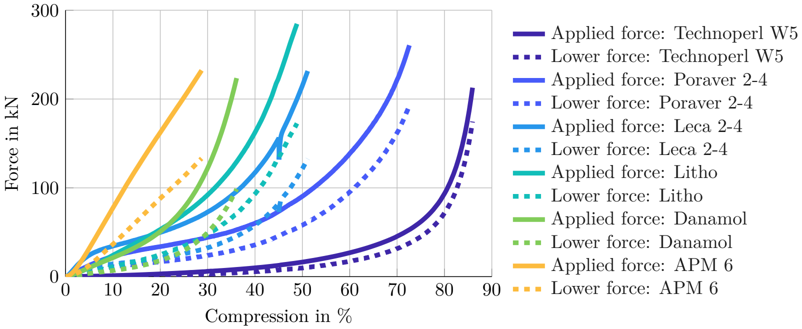

Figure 3.2: Force-displacement curves for different granules.

directly to the lower stamp, the more load is distributed to neighbouring particles and to frictional contact with the aluminium cylinder.

Figure 3.2 shows the resulting force-displacement curves for some selected granules. Two curves are shown for each of the granular materials. The solid line is the applied force on the top, while the dashed line represents the force at the lower stamp. Besides the difference in force, the general behaviour of the granules is a selection criterion. For example, the granule *Technoperl* is too soft. Materials are recommended that create a constant force plateau within a short displacement period, allowing the particles to carry and distribute a large part of the load. The granules show a good compressibility and are able to hold the plateau for a long time. This is important because the force acting on the lower stamp should not increase too rapidly, as this could potentially lead to an early rupture of the inner hull. Thus, granules like *Danamol* and *APM Foam* are considered too stiff. At the end, *Poraver* and *Leca* show a good compromise within these requirements. Due to its chemical advantages, the expanded glass granule *Poraver* is chosen as the primary material of interest. A study, with a closer look on the selection procedure, can be found in [120]. In Section 4.4.2, this experiment is used to derive material parameters. For a detailed discussion about the influence of particle properties, other granules will be investigated in the following chapters as well,for validation purposes.

3.2 Determination of grain properties

The scope of using DEM to model the granules in the near field of the collision requires detailed information about the particles. To obtain the parameter of interest – in particular Young's modulus, crushing strength, and diameter – single particle tests have to be performed [45]. The resulting parameters can vary widely, which is why a statistical representation is derived that can be used to create parameter tuple as input values for DEM [121]. Then, a possible application of the derived model is presented.

3.2.1 Single particle tests

To obtain the grain parameters, the particles are compressed between two flat surfaces, as shown in Figure 3.3. In doing so, a Hertzian contact can be assumed. This means that the deformation of the contact area is assumed as a circle. Then, the relation between the deformation s and the elastic contact force $F_{el,w-p}$ is given by [46, 122]:

$$F_{el,w\text{-}p} = \frac{4}{3} E^* \sqrt{R^* \left(\frac{s}{2}\right)^3} \tag{3.1}$$

with the indices *el* for elastic, *w* for wall, and *p* for particle, as shown in Figure 3.3. E^* is the effective modulus and is described as follows:

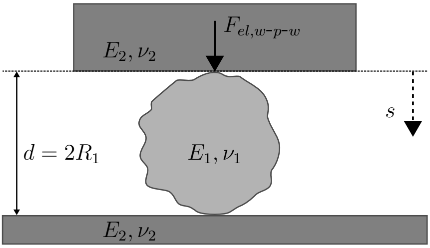

Figure 3.3: Compression of a particle between two plates.

$$E^* = 2\left(\frac{1-\nu_1^2}{E_1} + \frac{1-\nu_2^2}{E_2}\right)^{-1} \approx 2\left(\frac{E_1}{1-\nu_1^2}\right) \tag{3.2}$$

with the assumption $E_2 \gg E_1$. The effective radius R^* is given by:

$$R^* = \left(\frac{1}{R_1} + \frac{1}{R_2}\right)^{-1} \approx R_1 = \frac{d}{2} \tag{3.3}$$

for $R_2 \to \infty$. These assumptions, and taking into account that there is a wall on each side of the particle, lead to:

$$F_{el,w\text{-}p\text{-}w} = \frac{1}{3}\left(\frac{E_1}{1-\nu_1^2}\right)\sqrt{ds^3} \tag{3.4}$$

with E_1 the Young's modulus, ν_1 the Poisson's ratio, and d the diameter of the particle. In doing so, a constant cross-section area of the particle is assumed during the test. To determine the initial area, radius R_1 is used at the beginning of the compression. This may introduce a small error, and the particles will not be well-rounded, but this can be neglected compared to the varying parameters. The Poisson's ratio is set to a constant value of 0.3. This value is taken from the literature, see [123], because it is difficult to identify exact values for the expanded glass granules and the direct relation to the effective Young's modulus in Equation (3.2).

The single particles are compressed using the *Texture Analyser TA.XTPlus*. A load cell with a maximum capacity of 50 N and a sensitivity of 0.001 N is used. The data was acquired with a sampling rate of 400 Hz and a spatial resolution of 1 μm. Figure 3.4 shows

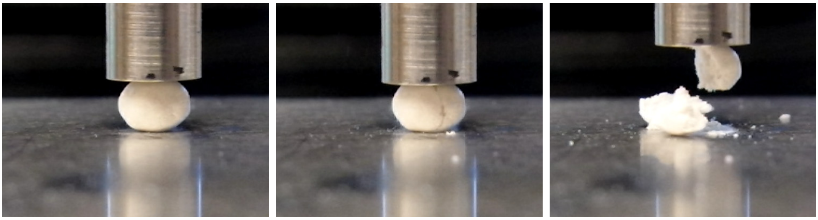

Figure 3.4: Loading states (from left to right): start of compression, breakage, and after unloading for a single particle of *Poraver*.

a particle under loading. The punch is driven into the particle with a constant velocity of 50 μm/s. In the first image, the start of the compression is shown. After contact detection, the initial height is measured to calculate the cross-section area. The probes are compressed until breakage, as shown in the last image.

To minimize the scatter in the measurement data, the granules are divided into smaller fractions with respect to their diameter, containing at least 100 particles to be tested.

The following sections serves to exemplarily show the results for *Poraver*. Other results can be found in [124, 121], while the results for *Poraver* are listed in Table 3.1. There, the material is divided into three fractions with the given diameter ranges. For the estimation of the crushing strength, the following relation is assumed for the stress:

$$\sigma = \frac{F_{el,w\text{-}p\text{-}w,crushing}}{\pi R_1^2} \quad . \tag{3.5}$$

Figure 3.5 shows the resulting stress-strain curves of four particles. The first thing to notice is the wide range of results for the crushing stress, which is marked with a square. Further, a lot of micro-cracks can be observed during the compression. This is due to the fact that the material is very brittle and consists of multicellular pores. These pores collapse under compression, especially in the contact areas. Whereas the crushing stress and force vary widely in a fraction, the crushing strain is approximately at 15 % over all

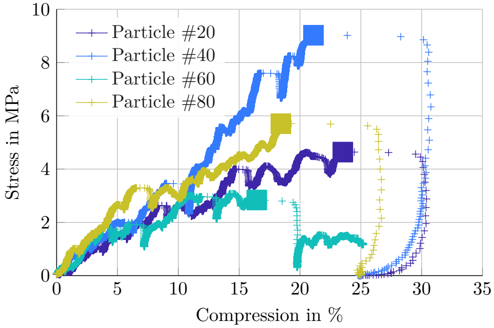

Figure 3.5: stress-strain curves of four different particles of *Poraver*.

Table 3.1: Experimental results for crushing stress and Young's modulus of *Poraver* and its fractions.

Fraction [mm]	Diameter [mm]	Cr. force [N]	Cr. stress [MPa]	Cr. strain [%]	E-Modulus [MPa]	Tests [-]
2.0 – 2.5	2.16 ± 0.15	14.81 ± 5.19	4.05 ± 1.45	16.49 ± 4.12	564.26 ± 260.60	94
2.5 – 3.125	2.68 ± 0.18	17.88 ± 5.45	3.19 ± 0.99	16.01 ± 4.98	453.79 ± 158.65	102
3.125 – 4.0	3.28 ± 0.22	21.62 ± 6.82	2.59 ± 0.87	14.66 ± 4.91	364.84 ± 127.85	106

fractions. Compared to the diameter, there seems to be a negative relation to the crushing stress. Smaller particles can resist higher stresses than bigger ones. This may be due to more initial defects in larger particles [52]. The identification of the Young's modulus is a bit more challenging. As already mentioned, the material of the particles is very brittle and it is difficult to read the Young's modulus from the stress-strain curves. This is followed by performing a least-square fit to the Hertzian model Equation (3.4). In doing so, it is necessary to assume an elastic region, which was found to be reasonable up to 2 %. This procedure is described in detail in [121] with all subsequent steps needed to get reasonable results. The corresponding Young's modulus for each fraction is shown in Table 3.1. Further – as for the crushing strength – a diameter dependency is observed, as shown in Figure 3.6. For larger particles, the Young's modulus decreases. In the next section, the observed diameter dependency – for both the crushing strength and the Young's modulus – will be used to develop a statistical model.

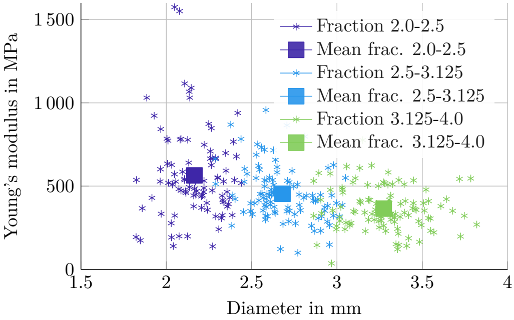

Figure 3.6: Distribution of the Young's modulus over the diameter for *Poraver*.

3.2.2 Statistical representation

In order to describe the parameter distribution, it is necessary to choose a function [52, 125]. For the diameter, a normal distribution is assumed. This leads to a diameter mean value of $\mu = 2.73$ mm with the standard deviation $\bar{\sigma} = 0.49$ mm for *Poraver*. For the Young's modulus and crushing strength, a logistic distribution is assumed. This choice is based on the work in [53, 54], which was extended in [121], as will be outlined here. The cumulative distribution function (CDF) of the logistic distribution is given by:

$$F_X(x) = 1 - \left[1 + \left(\frac{x}{X_{50}}\right)^S\right]^{-1} \quad . \tag{3.6}$$

The parameter X_{50} describes the mean value, while the parameter S describes the shape of the CDF. For bigger values of S, the distribution becomes narrower, see [121]. In the following, the model will be derived in subsequent steps. First, the crushing strength is considered and combined with the diameter distribution. Second, a similar approach is used for the Young's modulus. Finally, the models are combined to a three-dimensional representation to cover the parameter distribution of a granular material. Therefore, a total number of nine parameters are needed to describe the mechanical properties of the granules.

Crushing strength

Figure 3.7 shows the cumulative distribution of the crushing strength for the different fractions. Using the variables from the previous section, Equation (3.6) can be rewritten to

$$F_\sigma(x_\sigma) = 1 - \left[1 + \left(\frac{x_\sigma}{\sigma_{50}}\right)^S\right]^{-1} \quad , \tag{3.7}$$

with the mean breakage stress σ_{50} and shape parameter S for each fraction. The thick lines in Figure 3.7 represent the least square fit for these two parameters to the corresponding experimental results. The shape factor S was found to be relatively insensitive for a given granular material. Therefore, it is set to a constant value over all fractions, resulting in the mean value $S = 5.18$. As the next step, the observed diameter dependency – see the previous section – is taken into account. Reconsidering Equation (3.4), the equation can be stated as:

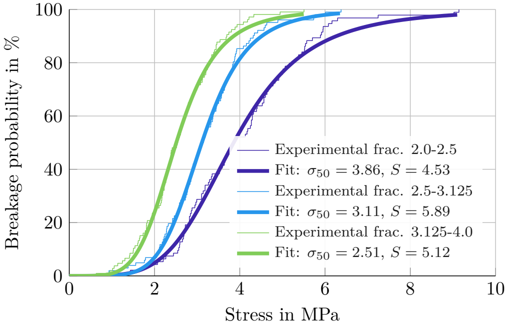

Figure 3.7: Distribution of the breakage probability depending on the applied stress for Poraver and the corresponding fits using Equation (3.7).

$$F_{el,w\text{-}p\text{-}w} \propto \sqrt{ds^3} = \sqrt{d^4\varepsilon^3} \quad \text{with} \quad s = d\varepsilon \quad . \tag{3.8}$$

Remembering, that the crushing strain is nearly constant over a granular material, it follows that the elastic contact force is proportional to d^2. This linear dependency of the force and square of the diameter was also found in [53]. Thus, they used the following ansatz to represent the elastic contact force:

$$F_{el,w\text{-}p\text{-}w} = A + Bd^2 \qquad . \tag{3.9}$$

Combined with Equation (3.5), the following model is obtained for the diameter-dependent mean breaking stress, now denoted as $\hat{\sigma}_{50}$:

$$\hat{\sigma}_{50}(d) = \frac{F_{el,w\text{-}p\text{-}w}}{A} = \frac{A + Bd^2}{\pi \left(d/2\right)^2} \qquad . \tag{3.10}$$

Using a least square fit, where all three fractions are considered, the following values are obtained for the introduced parameters: $A = 8.71$ N and $B = 1.18$ N/mm^2. The resulting CDF is visualized in Figure 3.8. As can be seen, the model fits the experimental results very well. Inserting the Equation (3.10) into Equation (3.7) leads to the final distribution function:

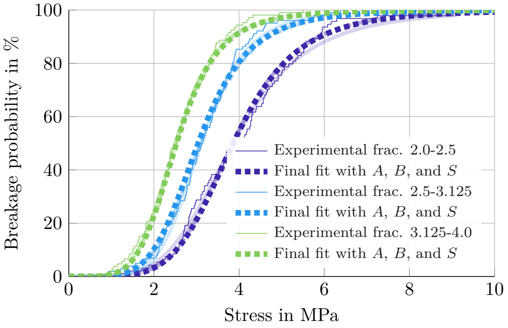

Figure 3.8: Distribution of the breakage probability depending on the applied stress for Poraver and the corresponding fits using the diameter relation given in Equation (3.10).

$$F_\sigma(x_\sigma; d) = 1 - \left[1 + \left(\frac{x_\sigma}{\frac{A+Bd^2}{\pi(d/2)^2}}\right)^S\right]^{-1} \tag{3.11}$$

with the three material-dependent parameters A, B, and S. With this equation, it is possible to plot the breakage probability in dependency of the applied stress and diameter, as shown in Figure 3.9.

Young's modulus

The same approach can be used to derive the distribution of the Young's modulus. By rewriting the logistic distribution function with respect to the Young's modulus, the following is obtained:

$$F_E(x_E) = 1 - \left[1 + \left(\frac{x_E}{E_{50}}\right)^{\tilde{S}}\right]^{-1} \qquad . \tag{3.12}$$

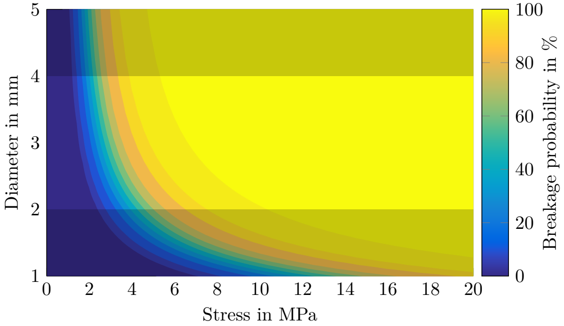

Figure 3.9: Two-dimensional distribution of the breakage probability depending on the applied stress and diameter for Poraver using Equation (3.11).

Fitting this equation to the experimental results using a least square method leads to the parameters given in Figure 3.10. As for the crushing strength, the shape parameter $\tilde{S}$ is set to a constant value for a granular material. Performing the same steps, but with a different ansatz to model the diameter dependency [54]:

$$\hat{E}_{50}(d) = \tilde{A}e^{-\tilde{B}d} + \tilde{C} \qquad , \tag{3.13}$$

which leads to the following equation for the CDF:

$$F_E(x_E; d) = 1 - \left[1 + \left(\frac{x_E}{\tilde{A}e^{-\tilde{B}d} + \tilde{C}}\right)^{\tilde{S}}\right]^{-1} \qquad . \tag{3.14}$$

The following parameters are obtained: $\tilde{S} = 4.82$, $\tilde{A} = 1152.6\,\mathrm{MPa}$, $\tilde{B} = 0.47\ \mathrm{mm}^{-1}$, and $\tilde{C} = 100.7\,\mathrm{MPa}$. For detailed information on all the steps, please refer to [121].

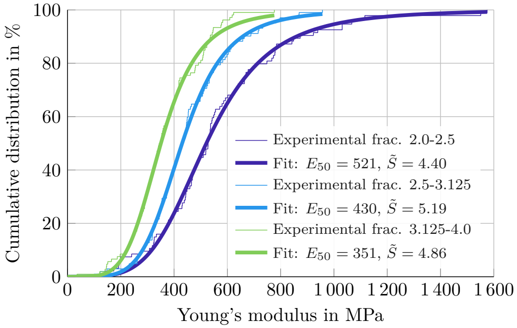

Figure 3.10: Distribution of the Young's modulus for *Poraver*.

Multidimensional representation

The derived models lack the inclusion of the diameter distribution. Therefore, the aim is to create a multidimensional distribution. In a first step, the diameter and the crushing strength distribution are combined. Then, the same is done for the Young's modulus. As the last step, all three parameters are considered in one model, in order to approximate the parameter distribution of a granule with nine parameters in total.

Figure 3.11 shows the kernel density function of the experimental results for the diameter and crushing strength. Representations of kernel density functions are similar to histograms. Here, a normal distribution is used as kernel function [126, 127]. To obtain the two-dimensional model, it is necessary to combine the probability density functions (PDF). For the diameter distribution, the PDF of a normal distribution is:

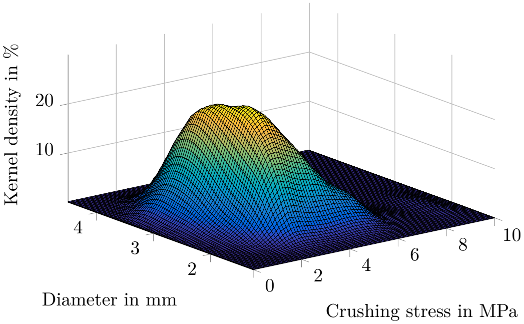

Figure 3.11: Kernel density function for diameter and crushing strength for *Poraver*.

$$f_d(x_d) = \frac{1}{\sqrt{2\bar{\sigma}^2\pi}} \exp\left(-\frac{(x_d-\mu)^2}{2\bar{\sigma}^2}\right) \quad . \tag{3.15}$$

To obtain the PDF of the crushing strength distribution, the CDF has to be derived from Equation (3.11). This results in the following equation:

$$f_\sigma(x_\sigma; d) = \frac{d^2\left(\frac{\pi}{4}\right)^S S\left(\frac{d^2 x_\sigma}{A+Bd^2}\right)^{S-1}}{(A+Bd^2)\left[\left(\frac{\pi}{4}\right)^S\left(\frac{d^2 x_\sigma}{A+Bd^2}\right)^S+1\right]^2} \quad . \tag{3.16}$$

These two PDF have to be combined:

$$f_{\sigma,d}(x_\sigma, x_d) = f_d(x_d)\cdot f_\sigma(x_\sigma; x_d) \quad , \tag{3.17}$$

resulting in a two-dimensional representation for the crushing strength.Figure 3.12 shows the resulting contour plot of this model, based on the parameters derived in the previous section. Thus, the diameter and crushing strength distribution can be described with five parameters: μ, $\bar{\sigma}$, A, B, and S. A good agreement with the experimental data is observed, as plotted in Figure 3.11 using the kernel density function.

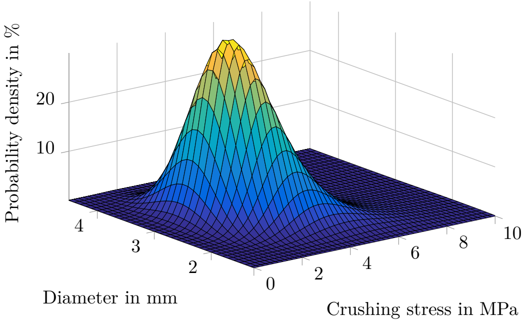

Figure 3.12: Probability density distribution for the diameter and crushing strength of *Poraver*.

The same approach is used for the Young's modulus. The PDF for Equation (3.14) is given by:

$$f_E(x_E;d) = \frac{\tilde{S}\left(\frac{x_E}{\tilde{A}e^{-\tilde{B}d}+\tilde{C}}\right)^{\tilde{S}-1}}{\left(\tilde{A}e^{-\tilde{B}d}+\tilde{C}\right)\left[\left(\frac{x_E}{\tilde{A}e^{-\tilde{B}d}+\tilde{C}}\right)^{\tilde{S}}+1\right]^2} \quad . \tag{3.18}$$

The multiplication of this Equation with Equation (3.15) leads to the results shown in Figure 3.13 on the right. This representation is in a good agreement with the experimental results – using the kernel density representation – on the left. For this two-dimensional model, six parameters are needed: μ, $\bar{\sigma}$, $\tilde{A}$, $\tilde{B}$, $\tilde{C}$, and $\tilde{S}$.

As the last step, all three distributions have to be combined. Thus, it is possible to get the particle parameters as input values for the DEM. Here, two models are compares. On the one hand, a multidimensional normal distribution is considered, obtained directly from the experimental results using a basic statistical approach [128] – and on the other hand, the approach presented beforehand is combined taking the diameter-dependency of the particles into account.

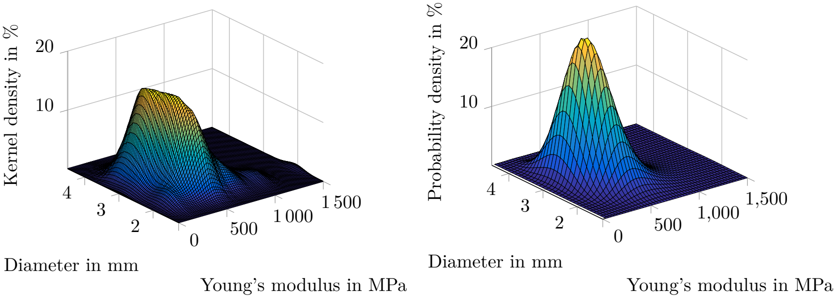

Figure 3.13: Kernel density function (left) and probability density distribution (right) for the diameter and Young's modulus of *Poraver*.

Normal distribution The three-dimensional normal distribution is chosen as a reference. Its PDF is given by:

$$f_{\mathbf{X}}(\mathbf{x}) = \frac{1}{\sqrt{(2\pi)^3 \det(\Sigma)}} e^{\left[-\frac{1}{2}(\mathbf{x}-\boldsymbol{\mu})^T \Sigma^{-1} (\mathbf{x}-\boldsymbol{\mu})\right]} \tag{3.19}$$

where $\boldsymbol{\mu}$ describes the mean vector and Σ represents the covariance matrix. For the granular material *Poraver*, the following parameters are obtained: $\boldsymbol{\mu} = [2.73; 3.25; 456.95]$ and

$$\Sigma = \begin{bmatrix} 0.24 & -0.32 & -41.38 \\ -0.32 & 1.59 & 103.80 \\ -41.38 & 103.80 & 41717.27 \end{bmatrix} \quad . \tag{3.20}$$

The entries in the vector/matrix are in the following order: $\{d; \sigma; E\}$. Figure 3.14 shows the experimental results as dots in the parameter space. For comparison, different bounds for the normal distribution are plotted. Most of the experimental data is within the 95.4 % confidence bound. Nevertheless, this model has a big drawback: Due to its definition, there is no restriction in negative axis direction [129]. Thus, negative values are possible. If it is used as a model to create particle parameters for the DEM within a 95 % confidence bound, this can lead to unphysical values. This can be seen in Figure 3.14 due to the cut sphere of the 95 % confidence bound at a crushing strength of 0 MPa. A possibility to overcome this is to use other distributions, as shown by the derived model in the next paragraph.

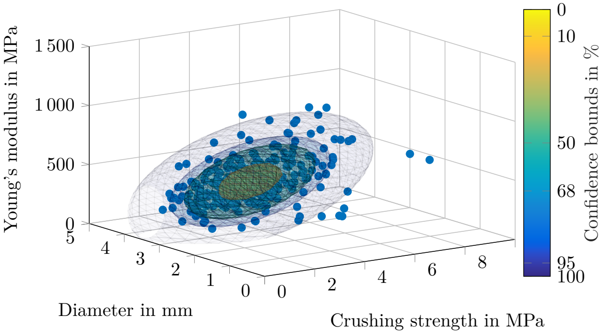

Figure 3.14: Three-dimensional distribution of the particle properties using a multidimensional normal distribution for *Poraver*.

Combined logistic distribution Combining different margin distributions can be challenging. The correlation of the parameters can play an important rule and alter the resulting distribution. There exist different approaches to take this into account [130]. For the granules under consideration, these steps lead to the following correlation coefficient matrix for the fraction 2.0 mm to 2.5 mm:

$$\mathbf{R} = \begin{bmatrix} 1.00 & -0.24 & -0.06 \\ -0.24 & 1.00 & 0.22 \\ -0.06 & 0.22 & 1.00 \end{bmatrix} \quad . \tag{3.21}$$

The values reflect the noisiness and direction of a linear relationship between the three parameters. Thus, the off-diagonal entries show the dependency for two different parameters in the following order: $\{d; \sigma; E\}$. Values closer to zero indicate a smaller linear relationship. Due to the small correlation coefficients, the correlation between the Young's modulus and the crushing strength is neglected. Thus, it is assumed that the correlation is only given due to the derived models taking the diameter-dependency into account. Therefore, the probability density function is a product of the diameter-dependent distribution of the crushing strength and Young's modulus and the diameter distribution:

$$f_{d,\sigma,E}(x_d, x_\sigma, x_E) = f_d(x_d) \cdot f_\sigma(x_\sigma; x_d) \cdot f_E(x_E; x_d) \qquad . \tag{3.22}$$

Figure 3.15 shows the resulting multidimensional contour plot. As for the normal distribution, the same confidence bounds are introduced. Compared to the normal distribution in Figure 3.14, the experimental data is covered more realistically. Only positive values are obtained, which is physically reasonable. Furthermore, it is a non-symmetric distribution that represents the tuples at higher stress/Young's modulus more accurately. To create this model, the parameters obtained in the previous steps are required, but no additional effort has to be done. Therefore, the model consists of the parameters μ, $\bar{\sigma}$ from the distribution of the diameter, A, B, S from the distribution of crushing strength dependent on the diameter, and $\tilde{A}, \tilde{B}, \tilde{C}, \tilde{S}$ from the distribution of Young's modulus.

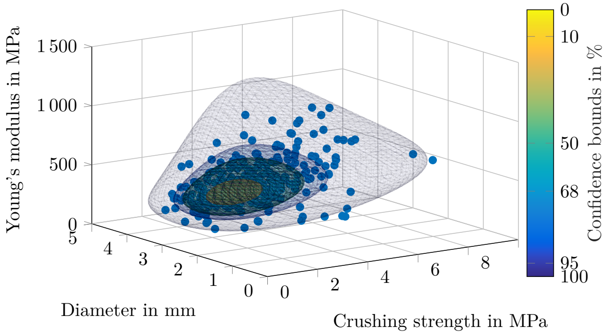

Figure 3.15: Three-dimensional distribution of the particle properties using the derived representation for *Poraver*.

Then, this model can be used to derive sample points as input parameters for DEM. This is described in detail in [121].

3.2.3 Numerical example

The derived representation for the particle parameters is used in the DEM. This section serves to present the numerical results that were obtained in the scope of the cooperation with the project partner. A detailed overview over the DEM is given in [110]. The numerical simulations of the experiments shown in this section are presented in detail in [116]. Next follow the abilities developed throughout the project, including the results for a simplified side hull structure filled with particles [111].

In order to be able to model this, several tasks have been performed, which will be briefly shown here. For more details, see the publications related to this project considering the particle parameters [124, 121, 116] as well as the numerical implementation [131, 110, 111].

The granules used are not perfectly round, and they interact with each other. Therefore a rolling resistance model is included in the DEM. In addition to this, it is not possible to assume rigid particles. Thus, aside of elastic and plastic deformations, it is necessary to include particle failure criteria. The crushing of particles is a major challenge in DEM, due to problems in mass conservation and reduction in time step size. Figure 3.16 shows the scheme of splitting particles, see [116]. It is obvious that there is a loss of mass. This is addressed using an iterative scheme, which recovers the mass of a particle. Furthermore, a framework is used to mitigate unstable motions of particles and therefore increase the computational efficiency. A meshless interpolation is used for numerical homogenization. This is based on particle dynamics and related stress [132, 133]. To achieve a further increase in computational efficiency, coarse graining is implemented in [112, 111]. The applied principle is based on scale-independent contact constitutive laws [134]. To use the DEM in combination with FEM, a coupling strategy is implemented that is based on the Arlequin method. An overlapping domain is considered where both models are applied and combined by means of a weight function. Thus, an interpolation between the DEM and the FEM is applied [58].

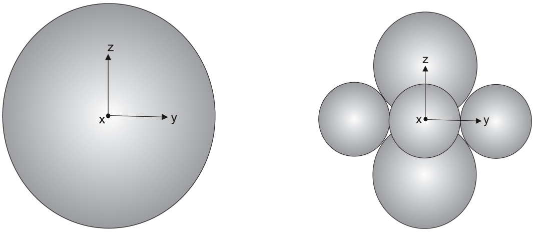

Figure 3.16: Splitting of particles into several smaller pieces after crushing (from [116]).

With all this work, a simplified side hull structure can be simulated within reasonable time using the DEM. The experimental setup is shown in Chapter 5.1. Next follow the numerical results of using granules as filling material and considering them as particles. The initial configuration for the double hull can be seen in Figure 3.17. Realistically sized particles are represented in grey, while the red particles are enlarged using coarse graining. Due to the fact that there is no crushing, the crushing model is only activated for the realistically sized particles. Closer to the boundary, FEM is used for the particles. The material properties are taken from the homogenization method mentioned earlier. The FEM is coupled with the coarsely grained particles using the Arlequin technique. The surrounding steel structure is modelled using shell elements with an enhanced strain-based element formulation [135]. To take into account the interaction between the indenter and steel parts, a contact model based on the mortar method with friction is used [136].

Figure 3.18 shows the deformed structure after the indentation process. To avoid very small time steps, the crushing is only allowed up to a minimal radius of the particles. The error introduced in doing so can be neglected, see [111]. At the end of the simulation, 523601 particles were present, while the simulation started with 300800 particles, see Figure

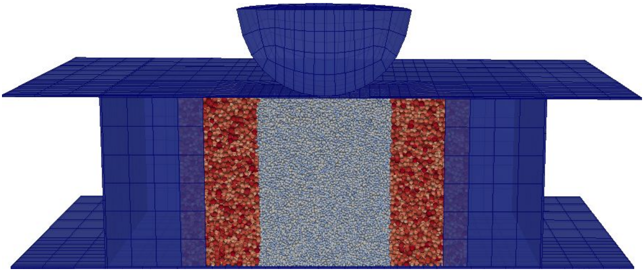

Figure 3.17: Model of the simulation using the coupled approach with DEM (from [111]).

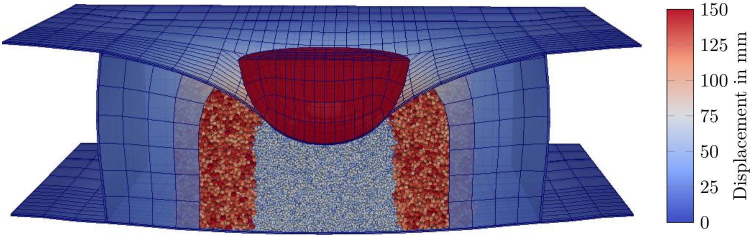

Figure 3.18: Deformation of a double hull using particles (from [111]).

3.17. The crushing of the particles can be seen in more detail in Figure 3.19. It can be seen that most of the particles close to the top surface are crushed. Compared to experimental data, the DEM performs very well. In Figure 3.20, a comparison is made between simulation and experiment with and without granules. The simulation without granules shows the correctness of the used model for the steel structure. An initial elastic behaviour of up to 20 mm is observed. After this, plasticity initiates for the part which is in direct contact with the indenter. Fracture occurs after approximately 145 mm, and the force decreases suddenly. This point is captured very well in the simulation.

The box with granules is also in good agreement with the experimental results. The increased stiffness of the whole structure is captured, while the rupture of the shell is

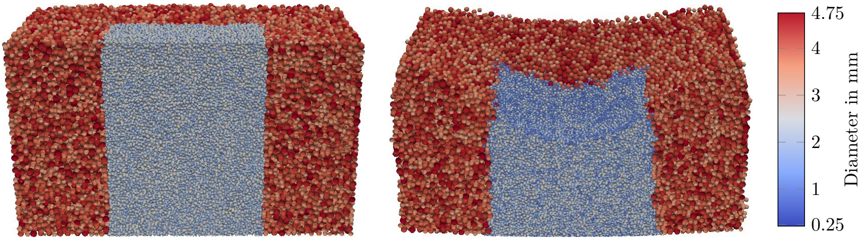

Figure 3.19: Grain sizes before and after the crushing of particles (from [111]).

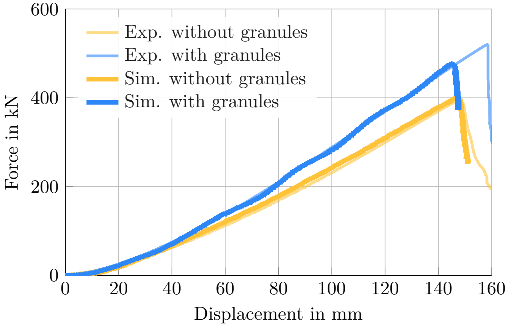

Figure 3.20: Comparison using DEM for modelling with experimental results from Chapter 5 (from [111]).

almost at the same displacement as for the empty structure. Reasons for this will be explained in later chapters. Overall, the use of this two-scale model is suitable to reduce the computational effort without altering the results.

4 Determination of bulk particle properties

This chapter focuses on tests to characterize the granules as bulk material. On the one hand, this is done to determine the material parameters from the test results, using the analytical description of the material models. Therefore, geomechanic tests are conducted. This approach is called direct identification [137]. On the other hand, a numerical optimization is performed to adjust the material parameters with respect to compression ratios for the uniaxial compression used in the previous chapter for the selection of granules. In this inverse problem, the parameters in the finite element model are adjusted until the calculated quantities match the measured quantities [137, 138].

In addition to the tests needed to characterize the granules, it is necessary to investigate the interaction of the granules with the surrounding structure. This mainly results in friction tests to determine the contact interaction of the particles with the steel structure.

To model the side hull structure, the steel parameters for an elasto-plastic material model with damage initiation have to be determined. Therefore, tensile tests are performed, serving as a basis for the parameter identification.

Due to the approach of a direct parameter identification, followed by a numerical correction, there is a loop within the procedure. This is depicted in Figure 4.1. Thus, the tests

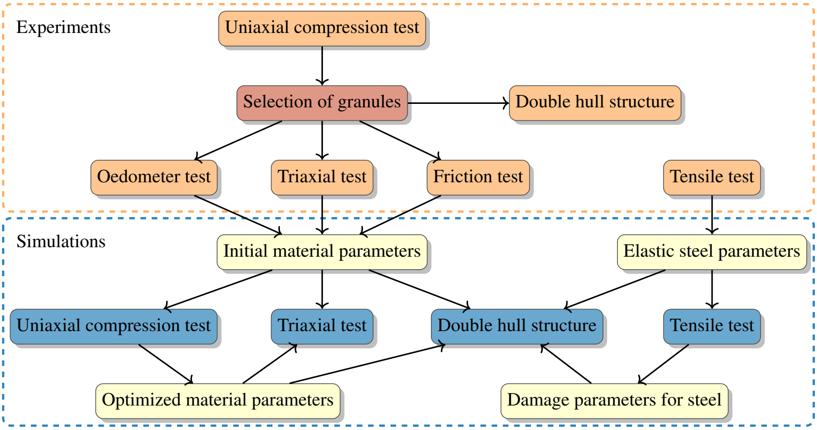

Figure 4.1: Schematic view of experimental and numerical relations between the different tests and experiments. The initial material parameters are used as input parameters for an optimization loop with the performed experiments.

are presented in the order of determining the granular material properties. And therefore, the numerical results for the triaxial tests with the obtained material parameters will be presented in a later section.

4.1 Oedometer test

The oedometer test is a standard test in geomechanics, and is easy to set up [61]. Therefore, its boundary conditions are simple to implement in the FEM, and it can be performed without great cost. Here, it will be used to get a closer insight in the particle size distribution at different stress levels.

The test is described in detail in DIN 18135, and a sketch of the setup is shown in Figure 4.2. A cylindrical probe with a diameter of 70 mm and a height between 20 mm and 25 mm is confined in a rigid ring. The top plate compresses the probe with a constant velocity of 0.1 mm/min and the stress-strain curves are determined.

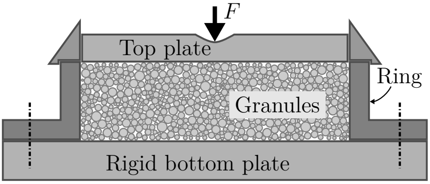

Figure 4.2: Oedometer test setup.

Before examining the particle size distribution at different stress levels, it is helpful to show the influence of the particle packing. Two different packings are created in order to do so: a loose package, with a bulk density of 205.2 kg/m^3, and a dense packing with a bulk density of 234.2 kg/m^3 [116]. Thus, the relative difference in density is 14 %. The strain-stress curves for these two configurations are shown in Figure 4.3. As can be seen, the two packages result in notable difference in the response of the material. The loose package exhibits almost twice the compression strain. Thus, it will be necessary to take care of the packing/filling process in the later experiments. Since the dense package is created due to small vibrations and movements during the pouring, this will be considered as a realistic boundary situation. These vibrations result in a homogeneous distribution

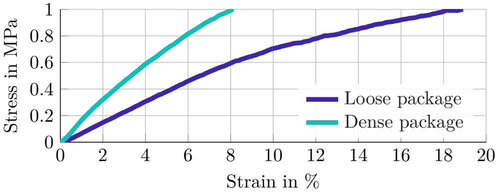

Figure 4.3: Comparison of the stress-strain response for a loose and a dense package of *Poraver*.

of the void ratio in the specimen, while the change in void ratio due to the compression is inhomogeneous. Thus, the two curves cannot be transformed into each other with an offset. A careful filling process – layer by layer, as for the loose package – is not a realistic situation.

To identify the breakage behaviour, the oedometer test is performed at different stress levels with a dense packing. Thereafter, the granules are sieved to obtain the grain size distribution. Figure 4.4 shows the resulting sieve distributions. Since the particle range is from 2 mm to 4 mm, only a few of the particles pass the 2 mm sieve for low stress levels. The amount of approximately 8% is in agreement with the data given by the manufacturer [139]. Up to a stress level of 400 kPa, no change in sieve distribution can be observed. Particles start to pass the smaller sieves at 600 kPa, which means that some breakage can be assumed – and even smaller sieves are passed as the stress level is increased further. This indicates that some of the particles are almost pulverized.

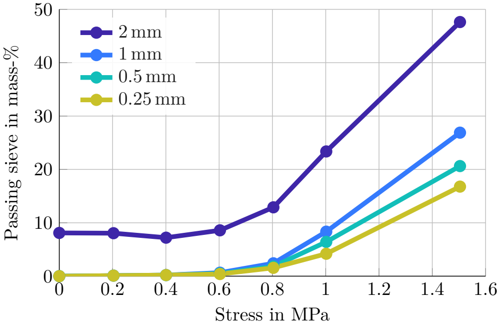

Figure 4.4: Sieve distribution for *Poraver* depending on the applied normal stress in the oedometer test.

Summarizing, a stress level over 400 kPa leads to crushed particles. Compared to the results in Chapter 3.2.1 Table 3.1, this is about a magnitude smaller than the crushing strength for single particles. This indicates that the crushing behaviour due to a different contact situation inside of a bulk material is different – and that the single particle tests result cannot be assumed for the bulk behaviour [116].

4.2 Triaxial test

The triaxial compression is a standard test in geomechanics, and it is commonly used for dry or saturated soils [61]. It is based on DIN 18 137 - D and its successor DIN 17892-8 [140]. The aim of this experiment is to determine the initial material parameters. Next, the experimental setup will be described, followed by the experimental results and, then, a numerical simulation based on the final material parameter obtained from Section 4.4.3.

4.2.1 Experimental setup

A cylindrical probe is submerged in a testing device, as shown in Figure 4.5. The probe is

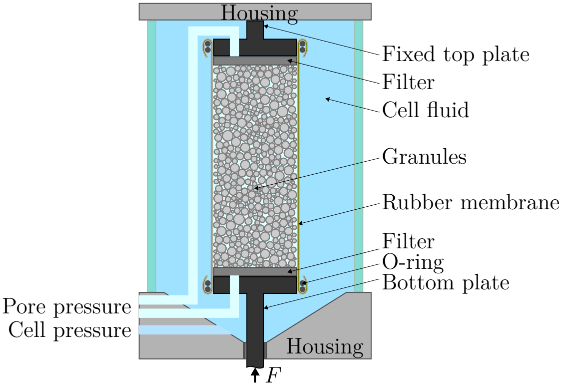

Figure 4.5: Setup of the triaxial compression test.

surrounded by a rubber membrane, to separate the granules from the cell fluid in the test chamber. At the top and the bottom, two plates with a filter enclose the probe in axial direction. The probe has a diameter of 50 mm and a height of approximately 120 mm. The cell fluid allows to apply different pressures in radial direction, which is necessary to identify the Mohr-Coulomb material parameters, see Chapter 2.1.2. The pressure inside the specimen can be regulated using the pore pressure valve. Due to the intended use as a filling material in an open space, atmospheric pressure is maintained using an open valve.

During the test, the specimen is compressed in axial direction. As granules with large diameters are used (compared to soils) air can circulate inside the specimen. Thus, the experiment can be performed with a compression speed of 1 mm/min without having to introduce artificial pressure states inside the probe. The experiment ends if shearing occurs or if a maximum strain of 20 % is reached [61].

Depending on the bulk density of the probe, different failure mechanisms can be seen. For dense specimens, characteristic shear lines are a likely outcome. Loose specimens, however, often result in a bulge, as shown in Figure 4.6. The conducted experiments only produced the shape shown in Figure 4.6 on the right. As mentioned before, different radial pressures have to be examined for each granule. Thus, at least three experiments have to be conducted.

4.2.2 Experimental results

The preparation of the specimen is an important aspect with regard to the experimental results. Usually, there are two ways to prepare the cylindrical probe: first, with a loose packing, for which the soil is poured into the membrane very carefully – and secondly, it is possible to use a dense packing, where the material is compacted inside the membrane. In the case of the granules, it is crucial not to damage the particles during the process. Thus, only a slightly compacted specimen can be obtained.

In total, the tests comprised eight different radial pressure levels with a dense packing for the identification of the Mohr-Coulomb material model. The results can be seen in Figure 4.7, where, the shear stress over the effective normal stress is shown. Since there

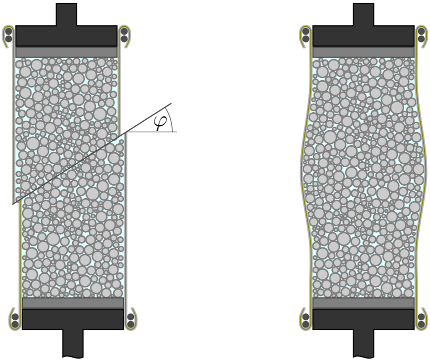

Figure 4.6: Typical failure types during triaxial compression: clear shear line (left) and bulge (right) (adapted from [61]).

is no pore pressure inside the specimen, due to the open valve, the effective normal stress equals the normal stress applied in the experiment.

Compared to the ideal behaviour of a Mohr-Coulomb material, as described in Chapter 2.1.2, the envelope of the circles is not a straight line. For small and large pressures, the absolute value of the maximum shear stress – the radius – is smaller than might be expected. This has different reasons. For small pressures, the influence of the membrane becomes more important, while the granules undergo significant crushing if subjected to larger pressures. Thus, only circles with a pressure between 100 kPa and 400 kPa are considered for the direct parameter identification of the Mohr-Coulomb material data. Eventually, this leads to the parameters given in Table 4.1. The parameters for Young's modulus and Poisson's ratio are taken from Section 4.4.2. The parameters φ, c, and ψ are determined using a common procedure based on the literature [61, 141]. The parameters φ and c are obtained using the envelope in the plot of the Mohr's circles, see Section 2.1.2. The dilatancy angle ψ is given by the change in volume in the triaxial test, which is zero.

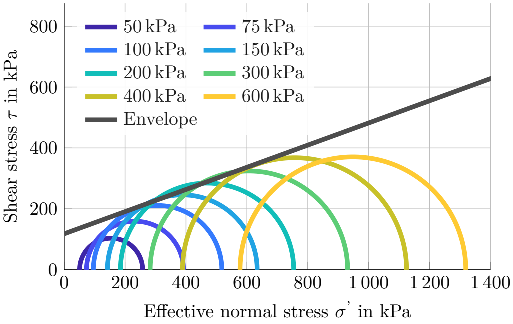

Figure 4.7: Mohr's circles for radial pressures from 50 kPa to 600 kPa and the corresponding envelope for the material *Poraver*.

Table 4.1: Material parameters for the Mohr-Coulomb material model, determined by experiments.

Material	E [MPa]	ν [-]	φ [°]	c [kPa]	ψ [°]
Poraver	4.18	0.28	20.0	118	0
Danamol	2.72	0.37	31.5	33	0

This experiment, in combination with an oedometer test, is also used for the hypoplastic model. The identification of the material parameters is shown in [104, 142]. In doing so, the material parameters obtained for *Poraver* are given in Table 4.2.

The parameters for the second granular material used in the simplified collision tests are also given in Table 4.1, for the Mohr Coulomb material model, and in Table 4.2 for the hypoplastic material model. The corresponding Mohr's circles are shown in the Appendix, Figure A.1, where the envelope is fitted in the same range as for *Poraver*. Compared to *Poraver*, the Mohr's circles for higher pressures are on the envelope, which indicates that the crushing of particles is not as strong as for *Poraver* with the considered radial pressures.

Table 4.2: Experimental results for the hypoplastic material model.

Material	h_s [MPa]	n [-]	φ [°]	α [-]	β [-]	e_{d0} [-]	e_{i0} [-]	e_{c0} [-]
Poraver	6.67	0.95	20.0	0.017	1.4	0.3475	0.7096	0.6170
Danamol	17.26	0.71	37.9	0.112	5.61	2.009	3.160	2.748

4.2.3 Numerical simulation

Using the material parameters obtained directly from the experiments in the section above, the numerical results will be discussed briefly, based on the two different material models. In doing so, the optimized parameter sets obtained in Section 4.4.3 will be considered as well. Thus, the numerical results for the triaxial compression test are in the same section as the description of the test.

For this purpose, a model consisting of 2400 elements is used, after performing a convergence study regarding mesh and time step size. To show the pure material model response, only the granules are modelled using eight-noded hexahedral elements with reduced integration. A geometrically non-linear analysis with an explicit time stepping scheme was chosen. The surrounding membrane can be neglected, since its already marginal influence gets smaller with higher radial pressure. Exemplarily, results for a pressure in the middle range of the parameter estimation will be shown. Thus, Figure 4.8 depicts the experiment and simulations for 200 kPa. The bilinear behaviour of the Mohr-Coulomb material model is clearly identifiable, resulting in a kink for each of the two curves [130, 88]. The parameters derived directly from the experiment in this section show a good overall agreement – considering the limitations of the material model – and match the force at the end of the

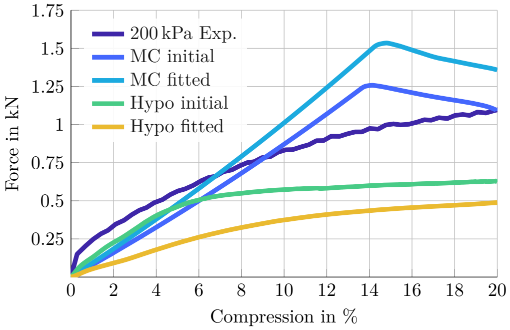

Figure 4.8: Simulation of triaxial compression test with a radial pressure of 200 kPa for *Poraver*.

experiment. The optimized parameter set shows a better agreement for the lower compression range – which was to be expected, since the optimization was performed for a compression ratio in this range.

Looking at the hypoplastic material model, two things stand out. First, both curves – the initial material parameters as well as the optimized parameter set – underestimate the force in the triaxial compression test. And, secondly, the general behaviour of the material model seems to be more suitable to match the loading path [104, 71]. Contrarily to the Mohr-Coulomb material model, the optimized parameter set performs – even for the beginning of the compression – inferior compared to the initial parameters. Nonetheless, the deformation shape using the hypoplastic material model looks more realistic. Figure 4.9 shows the shape of the specimen at the end of the experiment and simulation. Taking a look at the experiment – shown in the middle – a bulge shape can be observed – compare Figure 4.6. Using the Mohr-Coulomb material model – shown on the left – a clear shear line is visible, while the hypoplastic material model results in a bulge shape. Thus, this material model covers the granular behaviour of this soil better.

Using the material parameters for *Danamol*, a similar behaviour can be observed. The bulge shape that occurred in the experiments, see Figure A.2, is covered using the hypoplastic material model. This can be seen in Figure A.3 in the Appendix.

4.3 Friction test

After determining the material properties regarding only the granules, it is necessary to consider their interactions with other structures. Thus, the friction coefficients have to be determined for all material parings occurring in the simulation. For particle-particle interaction in the DEM, it is necessary to determine the coefficient for a granule with itself. This is done by setting up a friction test as shown in Figure 4.10, which is adapted from [3]. The granular material is attached to a sliding sledge (rotated in the image) before driving it over a surface while measuring the applied drag force. Different sliding speeds, normal forces, and connections between the sledge and the actuator were determined in [120]. A spring is used to determine the static friction coefficient. For the sliding friction

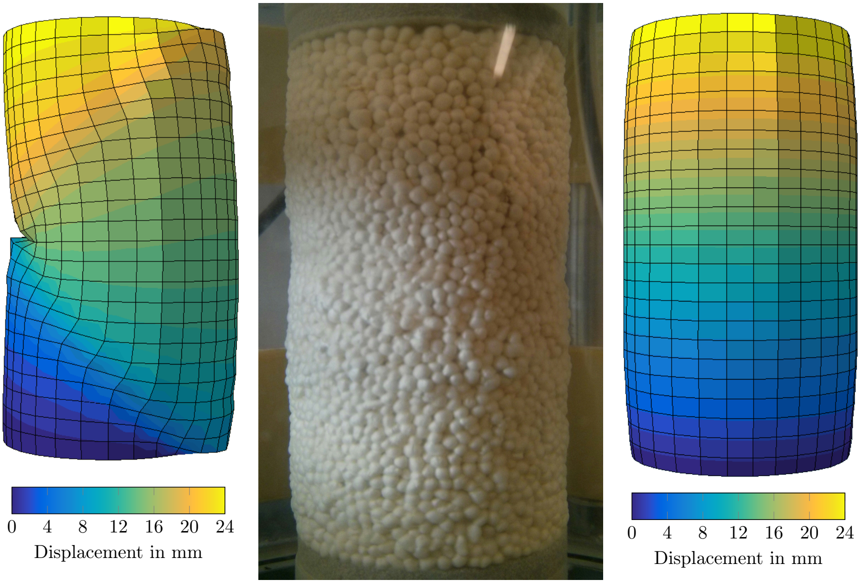

Figure 4.9: Displacement of Poraver during the triaxial compression. Left: Mohr-Coulomb material model. Right: Hypoplastic material model. Middle: Compression in the experiment.

coefficient, a rigid connection was found to be the best option. In [116] a sliding speed of 10 mm/s and a normal force of 80 N resulted in the smallest standard deviation regarding the measurement results. An example can be seen in Figure 4.11. To reduce experimental errors, the start and end sequence were cut off. Additionally, a low pass filter was applied to remove the high frequency measurement noise, resulting in the green line.

These steps lead to the static friction coefficients shown in Table 4.3. To determine the mean value and standard derivation, at least four experiments were conducted. As can be seen, the friction for the pair granule-granule is greater than 1. In this setup, probe plates are used as a sliding surface, which may result in an uneven contact zone. This can lead

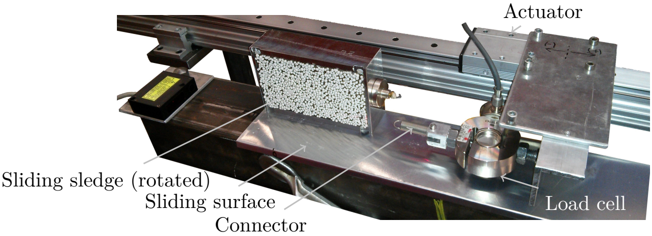

Figure 4.10: Setup of the friction test for different material pairings.

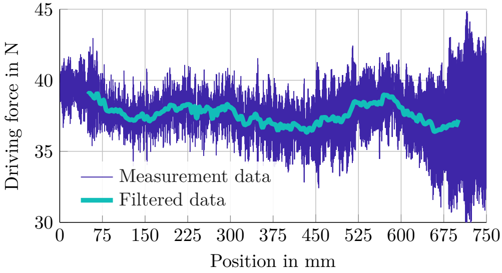

Figure 4.11: Determination of the driving force with an applied normal force of 80 N.

Table 4.3: Experimental results for the static friction coefficient of *Poraver*.

Material partner	Friction coefficient
Aluminium	0.704 ± 0.033
Steel	0.597 ± 0.015
Granule	1.078 ± 0.048

to physical locking of granules in the contact area. Table 4.4 shows the sliding friction coefficients.

Again, at least four experiments were performed for each pairing. The friction coefficients for steel and aluminium differ only slightly, compared to the static coefficients. Again, the granule-granule paring has the highest friction coefficient. Due to the uneven contact zone, stick slip effects occur, resulting in a higher deviation of the results. Thus, the results of this pair have to be treated with caution, but can be used as an indicator for the range of this parameter.

Table 4.4: Experimental results for the sliding friction coefficient of Poraver

Material partner	Friction coefficient
Aluminium	0.475 ± 0.036
Steel	0.483 ± 0.014
Granule	0.873 ± 0.090

4.4 Uniaxial compression test

In Section 3.1, this test was already briefly introduced. There, the purpose was to determine granules that meet the requirements. As already mentioned in the introduction of this chapter, the test is also used for the numerical identification of the material parameters.

Thus an optimization routine serves to adapt the parameters derived in the previous sections to the planned simulations. As additional measurement data are used, the experiment and identification scheme will be described in more detail.

4.4.1 Experimental setup

A simplified sketch of the experiment is shown in Figure 3.1. A more detailed plot is shown in Figure 4.12. The aluminium cylinder has an inner diameter of 181 mm and a wall thickness of 9 mm. The cylinder is placed on a support plate, and a gap allows for movement in horizontal direction – enabling free deformation if bulging occurs. Inside the cylinder, a load cell is installed to measure the force transmitted through the granules to the support stamp. On this stamp, the granules are poured into the cylinder until a granule column of 181 mm in height is reached. Then, a stamp is moved into the cylinder with a constant velocity of 1 mm/s. An additional force sensor is attached to the stamp. This setting allows to measure the difference in force applied at the top of the granules and transmitted to the bottom of the granule column. The difference reflects the force that is transferred, due to friction, to the cylinder wall directly into the housing. In total, it is possible to apply a force of up to 250 kN at the stamp, resulting in a maximum average stress of 9.72 N/mm^2. Revising the maximum stress before particle crushing – see Section 4.1 – it is exceeded by a factor of approximately 20.

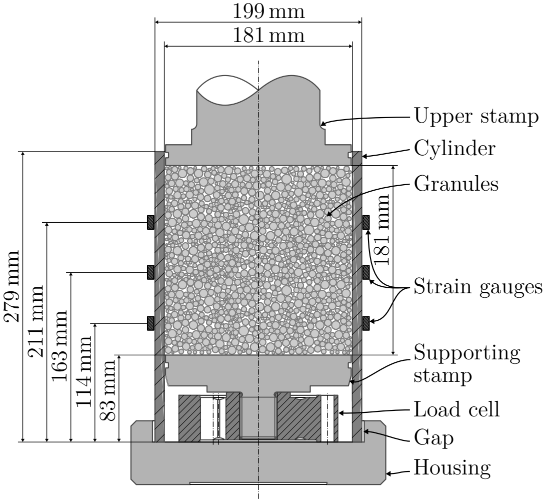

Figure 4.12: Dimensions of the setup of the uniaxial compression test.

Strain gauges are applied to the outside of the aluminium cylinder at three different heights in circumferential direction. The thickness of the aluminium cylinder allows small radial extensions without going into the plastic regime. Thus, the strain can be measured similar to a soft oedometer in geomechanics [143], providing additional data for validation and identification purposes. Due to the characteristics of the hydraulic system, the maximum stroke length is 100 mm. Thus, an extension is installed, resulting in an unloading and reloading during the experiment.

4.4.2 Experimental results

Figure 3.2 showed the force-displacement curves of several granules. Based on these results, several quantities of interest are derived. First, it makes sense to take a closer look at the dissipated energy, which was one selection criterion in Section 3.1. Next, the focus will be on the Young's modulus and Poisson's ratio – followed by a description of how to estimate the friction coefficient in order to compare it with the values derived in the previous section.

Dissipated energy

As mentioned in Section 3.1, the ability to carry and distribute load is a main requirement of the granules. With regard to a collision, the dissipated energy is a favourable quantity. Figure 4.13 shows the two types of energy that can be identified with the proposed setup. On the one hand, there is the total amount of energy introduced in the system – the crosshatch lines. On the other hand, there is the energy transmitted through the granules to the supporting stamp, represented by the green area. The difference between these – marked as an orange area – describes the energy dissipated due to friction at the cylinder wall. This is an indicator for the friction angle and for how well the granules can distribute the load. As was observed in unloading/reloading situations, elastic energy is almost non-existent during compression. Figure 4.14 shows the corresponding curves, derived from the force-displacement curves in Figure 3.2 by integrating the difference in forces. The curves are plotted until a maximum load of 100 kN is measured at the supporting stamp, which can be considered as the load capacity limit. This idea is based on an analogy to a ship hull, assuming a maximum load capacity for the inner hull before rupture. In doing so, *Poraver* and *Leca* provide the highest energy dissipation. Softer materials, such as *Technoperl*, are not able to distribute the load to the surrounding structure. Harder materials, such as *Danamol*, show a lower energy dissipation. As mentioned in Chapter 3, *Poraver* was chosen over *Leca* due to its chemical advantages. Another reason is its higher indentation depth at the same energy dissipation, allowing for larger deformations of the outer hull before a critical point for the inner hull is reached.

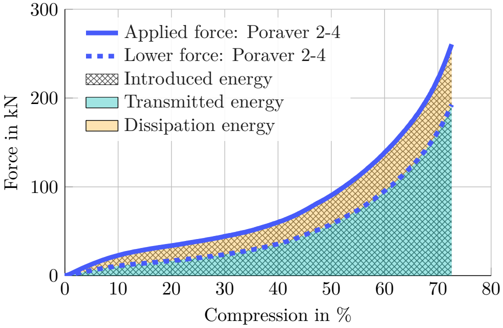

Figure 4.13: Categorisation of the energy introduced in the system of the uniaxial compression test.

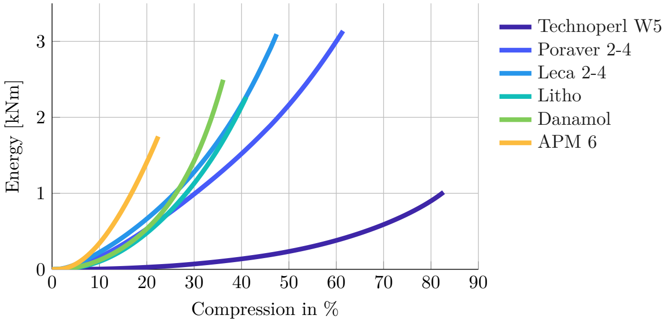

Figure 4.14: Dissipated energy due to friction in the uniaxial compression test: The curves are drawn until a force of 100 kN at the supporting plate is reached.

Young's modulus and Poisson's ratio

The Young's modulus of the granules is not constant, but strongly depends on the integrity of the grains and therefore on the compression. Nevertheless, a linear elastic relation is assumed for the Young's modulus, obtained through the following relation:

$$E = \frac{\sigma}{\varepsilon} \quad . \tag{4.1}$$

This assumption is made in order to describe the complex behaviour of these particles with material models that do not cover crushing. Thus, an elastic behaviour until a certain point for a bulk of particles has to be assumed. In Section 3.2.1, where single particles were tested, an elastic region up to 2% was assumed. In this section, this is not possible, since the measured forces and strains up to 2% are too small and noisy. Thus, an elastic range up to 10% is assumed. A Young's modulus of 4.18 MPa for *Poraver* is obtained. This is two magnitudes smaller than for single particles, see Table 3.1, which emphasizes the difference in behaviour between single grains and bulk materials. A value of 2.72 MPa is obtained for granules of *Danamol*.

The formula from [144] serves to determine the Poisson's ratio – neglecting the strain in radial direction, since it is very small compared to the compression in axial direction:

$$\sigma_r = \frac{E \cdot \nu \cdot s}{(1+\nu) \cdot (1-2\nu) \cdot h_0} \quad , \tag{4.2}$$

which relates the radial pressure σ_r and the axial displacement s with the material parameters. The radial pressure is assumed as the pressure at the cylinder wall. The pressure can be computed using Barlow's formula [145]

$$\sigma_r = p_i = \frac{\sigma_t \cdot 2t}{D_m} = \frac{E_A \cdot \varepsilon_A \cdot 2t}{D_m} \tag{4.3}$$

with σ_r the pressure in radial direction, t the wall thickness of the cylinder, D_m the mean diameter of the cylinder, and E_A, ε_A the Young's modulus of the cylinder and the strain on the cylinder, respectively. Inserting this into Equation (4.2) and rearranging leads to

$$\nu = -\frac{\sigma_r \cdot h_0 + E \cdot s}{4 \cdot \sigma_r \cdot h_0} + \frac{\sqrt{9 \cdot \sigma_r^2 \cdot h_0^2 + 2 \cdot \sigma_r \cdot E \cdot h_0 \cdot s + E^2 \cdot s^2}}{4 \cdot \sigma_r \cdot h_0} \quad , \tag{4.4}$$

while neglecting the solution with the negative root during the rearranging procedure. A Poisson's ratio of 0.28 is obtained for *Poraver*, which is close to the value of 0.3 used in Section 3.2 to estimate the single grain properties. A Poisson's ratio of 0.37 is obtained for *Danamol*.

Friction coefficient

To determine the friction coefficient, it is necessary to relate the normal force acting on the inside of the aluminium cylinder with the force transmitted through the cylinder. Using an ansatz based on the dissipated energy, it can be related as follows:

$$E_{fric} = \int F_{fric} ds = \mu_{g-a} \cdot \int F_N ds \quad , \tag{4.5}$$

where E_{fric} is the dissipated energy due to friction, F_{fric} is the force transferred via the cylinder, F_N is the normal force acting on the inside of the cylinder, μ_{g-a} is the friction coefficient between the granules and the aluminium, and s the displacement of the stamp. This ansatz leads to an averaged friction coefficient, which is an assumption made in accordance with the chosen friction model used in finite element simulation.

The normal force F_N can be calculated using the Barlow's formula Equation (4.3). The inner pressure p_i is related to the normal force and the surface area:

$$p_i = \frac{F_N}{\pi \cdot D_i \cdot h} \quad . \tag{4.6}$$

D_i is the inner diameter of the cylinder and h the height of the granule column. h can be expressed using the displacement of the stamp s and the initial height of column h_0 with $h = h_0 - s$. Inserting Equation (4.6) into Equation (4.3) leads to the following relation:

$$F_N = 2\pi \cdot E_A \cdot \varepsilon_A \cdot (h_0 - s) \cdot t \cdot \frac{D_i}{D_m} \quad . \tag{4.7}$$

By inserting this into Equation (4.5) and by rearranging, the following is obtained:

$$\mu_{g-a} = \frac{\int F_R ds}{2\pi \cdot E_A \cdot t \cdot \frac{D_i}{D_m} \int \varepsilon_A(s) \cdot (h_0 - s)\, ds} \quad . \tag{4.8}$$

This yields a friction coefficient of 0.54 for the material pair of aluminium and *Poraver*, and a friction coefficient of 0.52 for the pair of aluminium and *Danamol*. These values are slightly higher than the ones obtained with the friction test in Section 4.3.

4.4.3 Numerical simulation and parameter fitting

The uniaxial compression test is used to adapt the derived material parameters, and the following steps are carried out: to begin with, the model representing the experimental setup will be introduced, followed by a validation based on the derived material parameters. After this, the optimization procedure is explained in detail. Finally, the results are discussed and the final material parameters for the later studies are obtained.

Numerical modelling

The model is created and simulated with the finite element software *Abaqus* [72]. The investigations are based on a three-dimensional model, since the same elements will be used for the double hull structure as well. A similar approach was used in [146, 147], with a rotationally symmetric model. There, a comparison was made to the model presented here, and the advantages and drawbacks of using a rotationally symmetric formulation were discussed. The biggest advantage is the reduction in computational cost, while the reduced complexity does not cover nonsymmetric buckling of the aluminium cylinder.

The model is shown in Figure 4.15. Here – in concordance to the experimental setup, see Figure 4.12 – all relevant parts that are in contact with the granules are modelled. All parts are modelled using eight-noded hexahedral reduced integration continuum elements with hourglass control [88]. To save computational cost, a mesh study was performed and a coarse mesh was chosen, still maintaining numerical precision. This was done for the continuum elements representing the granules, as well as for the aluminium cylinder, which

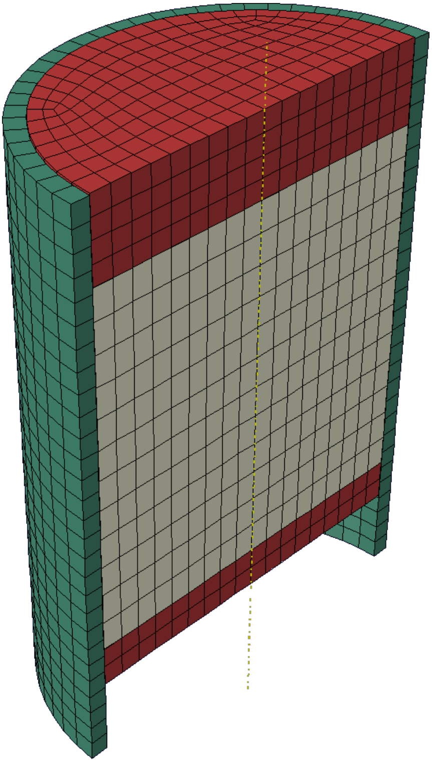

Figure 4.15: Finite element model of the uniaxial compression test: aluminium cylinder (green); stamps (red), granules (grey).

gives reliable results with only one element over thickness. Frictional contact is assumed between the parts, and boundary conditions matching the experimental setup are applied.

Linear elastic behaviour is assumed for the aluminium cylinder, since no plastic deformation occurred during the experiments. The material parameters are taken from the literature [148]. Thus, $E_A = 70$ GPa, $\nu_A = 0.3$, and $\rho_A = 2.7$ g/cm^3 are used in the simulation. The material data for the steel parts – the pressure plate at the bottom and the stamp at the top – are also taken from the literature, since they can be assumed as rigid. In doing so, the simulation is based on $E_S = 206$ GPa, $\nu_S = 0.3$, and $\rho_S = 7.85$ g/cm^3.

The granules are modelled as a homogeneous block using one of the proposed material models. The according implications and challenges are summarized in the following. First, the simulation might exhibit a tension state, which cannot occur in the experiment due to single grains. In this setup, however, this situation is unlikely. Second, the material parameters remain constant over the entire simulation. This implies the absence of grain damage. The idea of using voids or other geometrical imperfections in the mesh to account for this was not pursued any further, since it would contradict the aim of creating a simple mesh for the FEM calculation. The modelling of this complex behaviour is intended to be performed with DEM as part of the project. There are 3696 elements in total, as shown in Figure 4.15. The material parameters for the granules were determined in the previous sections. Since calculations with these parameters leave room for improvement regarding the simulation quality, the material parameters are fitted to the experimental results using the preliminary values as initial quantities.

Parameter fitting

A minimization problem is applied to determine the quantities of interest. For this, the software *Matlab* [149] is used and coupled with *Abaqus*. The general procedure is as shown in the following text. The parameter estimation script creates an input file – based on the current parameter vector – for *Abaqus*. Then, the simulation is executed and the results are compared to the experimental data. Based on the residual vector, the algorithm changes the parameter vector in order to minimize the residuum. This is depicted in Figure 4.16.

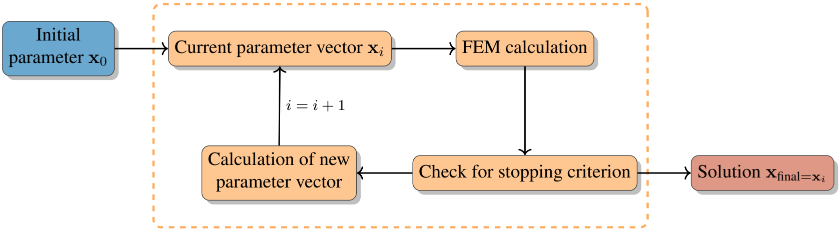

Figure 4.16: Optimization procedure to estimate a parameter set for the material models.

The algorithm can solve a non-linear, multi-variant minimization problem considering constraints:

$$\min_{x} f(\mathbf{x}), \text{ such that } \begin{cases} \mathbf{c}(\mathbf{x}) & \leq \mathbf{0} \\ \mathbf{c}_{\mathrm{eq}}(\mathbf{x}) & = \mathbf{0} \\ \mathbf{A} \cdot \mathbf{x} & \leq \mathbf{b} \\ \mathbf{A}_{\mathrm{eq}} \cdot \mathbf{x} & = \mathbf{b}_{\mathrm{eq}} \\ \mathbf{b}_{\mathrm{lo}} \leq \mathbf{x} & \leq \mathbf{b}_{\mathrm{hi}} \end{cases} . \tag{4.9}$$

In this case, it makes sense to choose the last inequality that defines the lower and upper bounds for the parameter vector $\mathbf{x}$. To solve the problem, several algorithms are available [149]. An overview over different optimization algorithms can be found in [150]. Here, the Interior-Point algorithm [151, 152, 153] is used, which was found to be the most robust method with regard to the problem at hand. In order to approximate the gradient of the function $f(\mathbf{x})$, either a central difference scheme or a forward difference step can be used. The latter results in less function calls and, as less simulations are executed, minimizes the computational costs.

The objective function $f(\mathbf{x})$ is the difference between the measurement data and the simulation results. To obtain more reliable residual results, the data is smoothed using a low pass filter and interpolated to obtain equidistant data over the displacement. Thus, the root mean square error is derived based on the forces:

$$RMSE_{stamp} = \sqrt{\frac{1}{n} \sum_{i=1}^{n} \left(f_{stamp,sim,i} - f_{stamp,exp,i}\right)^2} \tag{4.10}$$

and the $RSME_{pressureplate}$, respectively. The same is done for the strain gauges applied at three different heights. Thus, $RSME_{strain,1-3}$ is obtained. In order to normalize the residuum – thus taking into account the different order of magnitudes for force and strain – it is scaled with the initial residuum and a weight factor:

$$R_{final} = \frac{RSME_{force,i}}{RSME_{force,1}} + f \cdot \frac{RSME_{strain,i}}{RSME_{strain,1}} . \tag{4.11}$$

For the optimization, different parameter vectors are examined. In total, the following parameters are optimized: E, ν, c, φ, ψ, and μ_{g-a}. A reduced set is used to reduce the computational effort of calculating the gradient, as shown in Table 4.5.

The boundary values used in the minimization problem are based on physical and numerical considerations [146, 147]. The initial parameters x_i shown in Table 4.5 are expressed using:

$$x_i = b_{lo,i} + \tilde{x}_i \left(b_{hi,i} - b_{lo,i}\right) , \tag{4.12}$$

which results in an optimization vector $\tilde{\mathbf{x}} \in [0, 1]$ for the i quantities to optimize. This allows for an easier tweaking of the optimization options, such as step size or stopping criterion.

The interior point algorithm searches for the global minimum inside the design space. The restrictions are enforced using barrier functions added with penalty terms. Usually, an inverse or logarithmic barrier function is applied. In the algorithm, the logarithmic function is used:

$$P(\mathbf{g}(\mathbf{x}), r) = \frac{1}{r} \sum_{i} \log\left(-g_i(\mathbf{x})\right) , \tag{4.13}$$

Table 4.5: Parameter sets and initial values for the optimization of the Mohr-Coulomb material parameters.

	Parameter set		
Parameter	initial	small	large
E [MPa]	4.18	var	var
ν	0.28	var	var
φ	20	fixed	var
ψ	0.1	fixed	var
c [kPa]	118	fixed	var
μ_{g-a}	0.54	var	var

where $\mathbf{g}(x)$ are the boundary conditions and r the penalty parameter as the internal variable of the interior point algorithm. The problem is solved by using the *Karush-Kuhn-Tucker* condition and transferring the problem to a non linear system of equations [150]. Eventually, this will be solved using the *Newton-Raphson* scheme [149].

Results of parameter estimation

Since the proposed idea uses the FEM to calculate the far field response, with smaller compression ratios, the parameter identification is performed for different maximum compression levels. Thus, we restrict the compared compression level to 10 %, 20 %, and 30 %. This procedure allows to reduce the simulation time – and it serves as a basis to discuss the effect on the material parameters with respect to the compression level. The initial material parameters are given in Table 4.5. In the following, the results for 10 % will be presented in detail, followed by the two remaining compression ratios and, finally, a concluding discussion.

10 % compression Figure 4.17 shows a comparison between the experimental results and the simulations. The initial parameter set for the Mohr-Coulomb material model underestimates the measured forces. Not only the total force is too low, but also the force transmitted to the support stamp. Nonetheless, the initial guess using the analytical results from the previous section are acceptable. Using the proposed minimization algorithm the residuum can be reduced – leading to the curve shown in green. In this optimization, only the parameters estimated in this section – the Young's modulus, Poisson's ratio, and Friction coefficient – are changed. The error in residuum can be reduced by 70 %. Due to the constitutive material behaviour, a further reduction is not possible, since the bending of the curve due to breakage cannot be covered. Moreover, the path of the measured strain values cannot be caught very well, regardless which weight factor is chosen to take this residuum into account, see Equation (4.11). With only these parameters, the strains measured on the aluminium cylinder are not affected. In total, 10 iterations are performed during the minimization process with a quick reduction of the residuum during the first steps. The final parameters are listed in Table 4.6. The coefficient of determination

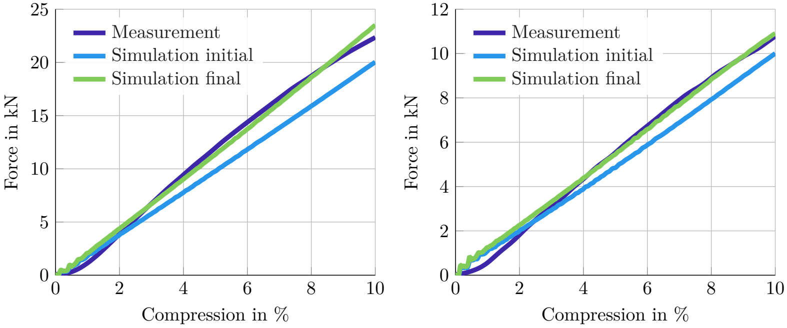

Figure 4.17: Force-displacement curves for an optimization up to 10% compression: total force applied (left) and force transmitted through the granules (right).

Table 4.6: Numerical results for the optimization of the two different parameter sets and three different optimization ranges.

Compression	10%		20%		30%	
Parameter set	small	large	small	large	small	large
E [MPa]	5.09	4.82	4.46	5.08	5.04	4.95
ν	0.25	0.28	0.24	0.20	0.15	0.20
φ	20	20.79	20	15.01	20	5.01
ψ	0.1	0.19	0.1	0.21	0.1	0.11
c [kPa]	118	158	118	196	118	211
μ_{g-a}	0.66	0.58	0.59	0.70	0.64	0.57

for the model is $R^2 = 0.99$, which indicates that the model is suitable for parameter identification [154].

Considering a larger parameter set leads to the curves shown in Figure 4.18. The result in reduction of the residuum is similar to the smaller parameter set, a reduction of 71 % can be observed. In contrast, the strain values are altered as well, leading to this slight improvement. The final values are given in Table 4.6. Compared to the initial and smaller parameter set, the changes in friction angle and dilatancy angle are quite small. Only the friction coefficient has a significant influence on the simulation results.

20 % and 30 % compression Using a different range for the parameter estimation leads to a different result. The parameters are shown in Table 4.6. Compared to the initial parameter, see Table 4.5, the following can be observed. First, the Young's modulus is underestimated, using the analytical approach. The friction coefficient φ decreases with higher strain, which corresponds to the results seen in [3]. Contrary, the cohesion increases. For higher stress levels, the Poisson's ratio shows a decreasing trend. Looking at the dilatation angle, the assumption of no dilatancy holds for the numerical parameter estimation. The friction coefficient is in the same range as the analytical results. Thus,

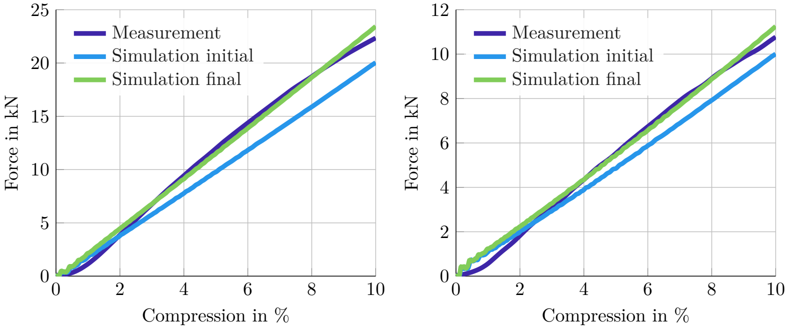

Figure 4.18: Force-displacement curves for an optimization up to 10% compression with the larger parameter set: total force applied (left) and force transmitted through the granules (right).

according to the values obtained for other material pairings, this experimental method is suitable.

For the sake of completeness, Figure 4.19 shows an overview of the results of the parameter estimation up to 20 % and 30 % compression. As can be seen, the parameters obtained by the optimization are especially suitable to cover the force transmitted though the granules. The parameters for the initial parameter set were derived up to a compression of 10%, which is why the simulation results using this set differ significantly for larger compressions. The crushing of the particles during the experiment cannot be modelled.

As a consequence, all further calculations are based on the obtained values up to 10 % compression and with six free parameters. This is due to the fact that most of the particles undergo only small deformations.

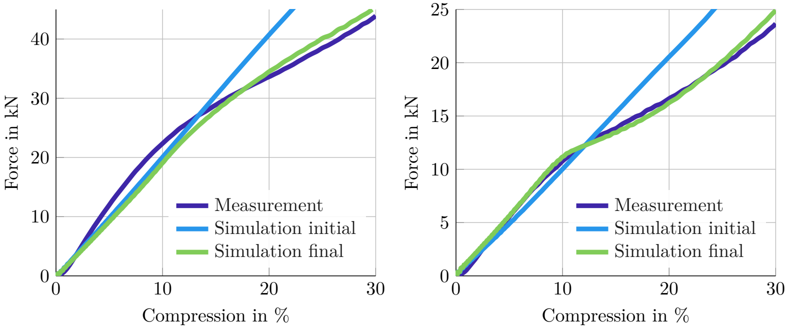

Figure 4.19: Force-displacement curves for an optimization up to 30% compression with the larger parameter set: total force applied (left) and force transmitted through the granules (right).

Table 4.7: Fitted results for Mohr-Coulomb material model for *Danamol* up to 10% compression and the large optimization set.

Material	E [MPa]	ν [-]	φ [°]	c [kPa]	ψ [°]
Danamol	3.16	0.28	15.1	101	0

For the second material, the material parameters given in Table 4.7 are obtained, and the corresponding force-displacement curves are shown in Figure A.4. For the parameter identification, the same boundary conditions and parameter set was used as for *Poraver*.

Hypoplastic material model The same approach was carried out for the hypoplastic material model. Since the material model requires more computational effort, only the estimation for one parameter set with a deformation range of up to 10 % is shown. Three parameters are optimised: the friction angle φ, the hardness h_s, and the exponent n.

As can be seen in Figure 4.20, the initial parameters derived from experimental tests do not yield a satisfactory result for the material *Poraver*, which will be discussed in the following. The material behaves too stiff in the uniaxial compression test. During the optimization process, the initial residuum is reduced by 97 %, resulting in the curve shown in the same Figure. In total, 12 iterations are performed to find this minimum. The final parameters used for the optimized simulations are shown in Table 4.8. The main change in the parameters can be observed for the hardness of the granule. The parameter h_s is decreased by 70 %, resulting in a good agreement for the total force. Compared to the Mohr-Coulomb parameter estimation – see Figure 4.17 – the force measured at the lower stamp is not estimated as accurately.

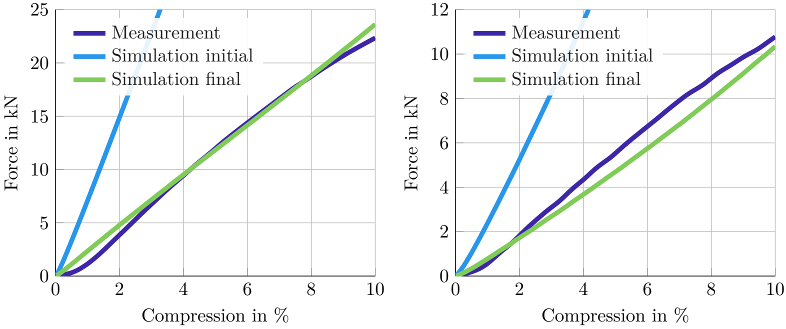

Figure 4.20: Force-displacement curves for an optimization up to 10% compression using the hypoplastic material model: total force applied (left) and force transmitted through the granules (right).

Figure 4.21 shows the compaction or displacement of the granules, with the experimental results in the middle. In the view from the top, a highly compacted top layer is visible, while the granules at the bottom of the probe are partially still intact. This behaviour

Table 4.8: Fitted material parameters using the hypoplastic material model with experimental data up to 10% compression.

Material	h_s [MPa]	n [-]	φ [°]	α [-]	β [-]	e_{d0} [-]	e_{i0} [-]	e_{c0} [-]
Poraver	1.98	1.04	17.5	0.017	1.4	0.3475	0.7096	0.6170
Danamol	21.46	0.36	30.6	0.112	5.61	2.009	3.160	2.748

can be observed in the simulation using the hypoplastic material model. There – see Figure 4.21 right – the main compaction occurs at the top layer of the granules. Using the Mohr-Coulomb material model – Figure 4.21 left – a uniform distribution can be observed. Thus, the hypoplastic material seems to be a promising alternative to the Mohr-Coulomb material model, if a more realistic state inside the granules is needed. This, of course, comes with the drawback of higher computational costs.

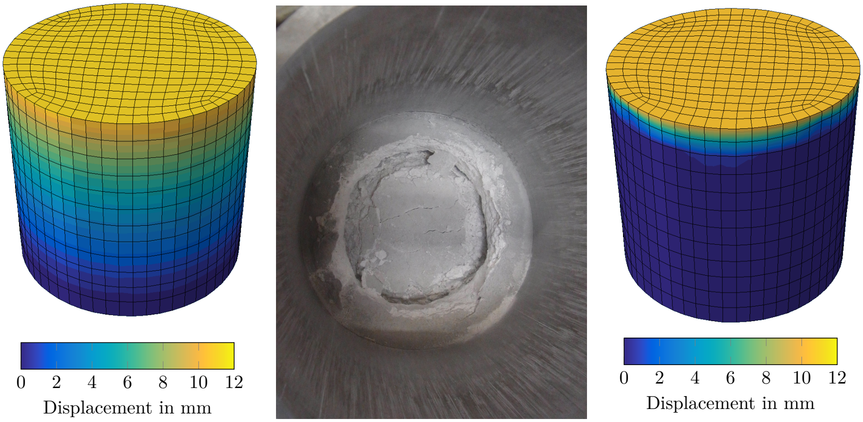

Figure 4.21: Displacement of *Poraver* during the uniaxial compression. Left: Mohr-Coulomb material model. Right: Hypoplastic material model. Middle: Compaction in the experiment.

For *Danamol*, the parameters shown in Table 4.8 are obtained after 15 iterations and a reduction in residuum of 92 %. The change in force-displacement response from the initial parameter set to the optimized parameter set is shown in Figure A.5. Compared to *Poraver*, the initial parameter set does not represent the experiment acceptably. The final parameter set covers the total force quite well, but the force transmitted to the stamp remains too high. Furthermore, more stick-slip effects are observed during the computation, resulting in a rougher curve.

4.5 Tensile test

As the last aspect, it is necessary to determine the parameters of the steel parts for the experimental setup of the double hull structure. A S235 ship building steel is used, with a minimum yield strength of 235 MPa. All steel plates have a thickness of 3 mm and are cut from a rolled steel plate. As the double hull structure was built and tested several times, the investigations involved steel plates from different manufacturing batches. Thus, the tests and parameter identification procedures are carried out separately for each of them.

To obtain stress-strain curves, tension tests according to DIN EN ISO 6892-1 (2017-02) are performed. Due to the manufacturing process, the material is not perfectly isotropic. The material parameters in longitudinal and transversal direction to the rolling direction vary slightly. The tests involve dog bone specimens with a width of b = 20 mm and a length of L_0 = 40 mm. The measured thickness during the test was between t = 2.9 mm and t = 3.1 mm. At least three tests are performed for each direction. The averaged results for the direction can be seen in Figure 4.22. The two different batches show a very different behaviour. Steel batch 1 has a higher yield strength and a visible Lüders expansion. The second steel batch has a higher fracture strain. For each batch, the longitudinal direction shows a smaller fracture strain compared to the transversal direction. The experimental results are given in Table 4.9 and Table 4.10.

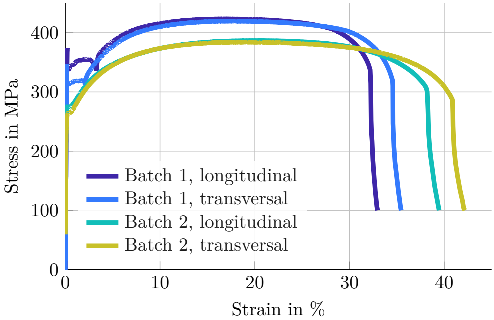

Figure 4.22: Experimental results from tensile test.

As stated in Chapter 2.1.4, an isotropic material model is assumed. Thus, the material parameters have to be averaged for each batch. To estimate the Young's modulus, the

Table 4.9: Tensile test results and standard deviation for batch 1.

	longitudinal	transversal	combined
t in mm	2.92 ± 0.04	2.9 ± 0.0	2.91 ± 0.03
$Rp_{0.2}$ in MPa	337.8 ± 1.6	314.8 ± 1.9	326.3 ± 12.2
R_m in MPa	423.6 ± 0.5	420.2 ± 1.3	421.9 ± 2.0
A in %	32.2 ± 0.4	34.4 ± 0.2	33.3 ± 1.2
Z in %	66.4 ± 2.1	69.6 ± 4.0	68.0 ± 3.5

Table 4.10: Tensile test results and standard deviation for batch 2.

	longitudinal	transversal	combined
t in mm	3.05 ± 0.01	3.07 ± 0.02	3.07 ± 0.02
$Rp_{0.2}$ in MPa	275.0 ± 0.0	261.7 ± 3.5	268.3 ± 7.6
R_m in MPa	387.0 ± 0.0	381.3 ± 3.1	384.2 ± 3.7
A in %	39.7 ± 0.6	$42.3.2 \pm 0,6$	41.0 ± 1.5
Z in %	53.0 ± 2.0	68.7 ± 0.6	60.8 ± 8.7

linear elastic part of the curve is considered. The results are $E = 205.92$ GPa for batch 1 and for $E = 197.28$ GPa batch 2. The Poisson's ratio of $\nu = 0.3$ is taken from the literature, see [148].

To determine the plastic behaviour of the material, it is necessary to find an expression for the hardening law, which also represents the material without any damage or necking. Therefore, Equation (2.39) can be used:

$$\tilde{\sigma}\left(\varepsilon^p\right) = C \cdot \left(\varepsilon_0 + \varepsilon^p\right)^n \qquad , \tag{4.14}$$

which is often applied for construction steel [107]. This has two advantages: First, this reduces the number of parameters needed to describe the material behaviour – and, secondly, the extrapolation needed for the simulation can be performed with ease. For the finite element simulation, the part of the Lüders expansion is assumed to be a constant line. Then, using an optimization algorithm yields the black curve shown in Figure 4.23.

With regard to the procedure in Figure 4.23, the measurement data between the vertical lines serves as a data basis for the extrapolation – and the black line is used as extrapolated data for the simulation. As a consequence, it can be observed that the stress-strain response underestimates the experimental result for batch 1 and overestimates it for batch 2, as can be seen in Figure 4.24 with the black line for batch 2. Therefore, an additional quadratic term is introduced at the beginning of the necking, i.e. from the beginning of the extrapolation [108]:

$$\sigma_{add} = k \cdot \left(\varepsilon^p - \varepsilon^p_{add}\right)^2 \qquad . \tag{4.15}$$

The resulting stress-strain curves are depicted in Figure 4.23 for steel batch 2. Comparing with the experimental results, see Figure 4.24, the value of k is chosen such that the simulation results are within the bounds given by the longitudinal and transversal experimental results in combination with an applied damage modelling.

The damage parameters are determined using a parameter optimization. As described in Section 2.1.4, it is necessary to determine the critical equivalent fracture strain $\bar{\varepsilon}^p_D$ and the damage evolution based on a generalized displacement given by Equation (2.41)

$$D = \frac{1}{\left(\bar{u}^p_f\right)^m} \cdot \left(\bar{u}^p\right)^m \qquad . \tag{4.16}$$

A detailed study about the influence of the parameters $\bar{\varepsilon}^p_D$, $\bar{u}^p_f$, and m is given in [108].

This results in the curves given in Figure 4.25 for both steel batches. As can be seen, both simulations are within the bounds of the corresponding longitudinal and transversal experimental results.

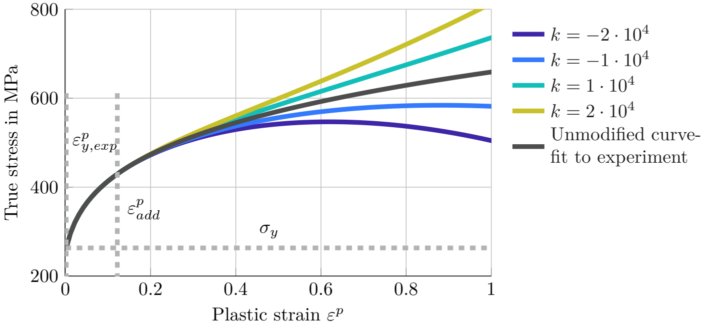

Figure 4.23: Extrapolation of the plastic behaviour without the onset of necking for *Abaqus* with a quadratic term added after the onset of necking ε^p_{add}.

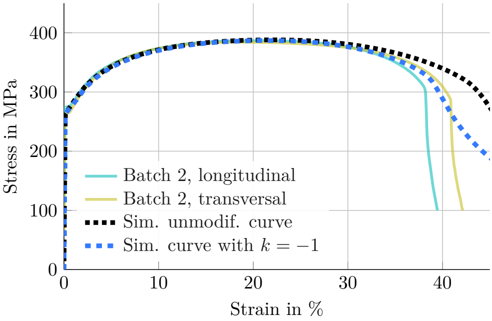

Figure 4.24: Simulation of tension test for steel batch 2 with damage modelling for the unmodified plastic curve and the modified plastic curve without damage.

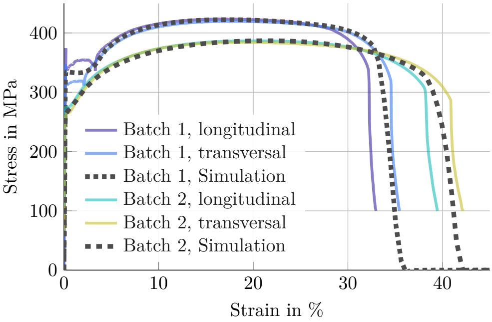

Figure 4.25: Simulation of tension test for steel batch 1 and batch 2 with damage modelling for the modified plastic curve including damage initiation and evolution.

5 Experimental investigation

In order to evaluate the granules as a filling material, a representative experiment has to be conducted. As mentioned in Section 1.2, collision tests are still mandatory to obtain experimental results for the validation of numerical simulations. The setup used here is similar to the one in [29, 20], where a bulb impact with a ship structure was investigated. The setup in [20] is adapted to the problem at hand, allowing to perform numerical computations, based on the given results, during the design process of the experimental test. There, a simplified double-bottom side structure with stiffeners and stringers was investigated, scaled down by a factor of 3. In order to adapt the details to the testing facility used for this work, the hull thickness was reduced slightly. Further, the inner structure was simplified and a closed box for the granules was created [106].

The next section focuses on introducing the setup, followed by a discussion of the experimental results. In total, seven experiments are conducted. The purpose of the first four experiments is to investigate the benefits of using granules. Thus, two empty and two filled experiments are performed. The last three experiments are carried out with an additional stiffener. The experiments are also performed with a different granular material.

5.1 Experimental setup

Figure 5.1 shows the simplified side hull structure with its dimensions. The two plates – later referred to as *outer hull* and *inner hull* – are connected by a rectangular box. The overall dimensions are 1500 mm in width and 1090 mm in depth, like in the experiment in [20]. The distance between the plates is 280 mm. Based on preliminary numerical results, a plate thickness of 3 mm was chosen. In doing so, a maximum force of 600 kN was predicted for a structure without granules [106]. Thus, the setup provides enough safety

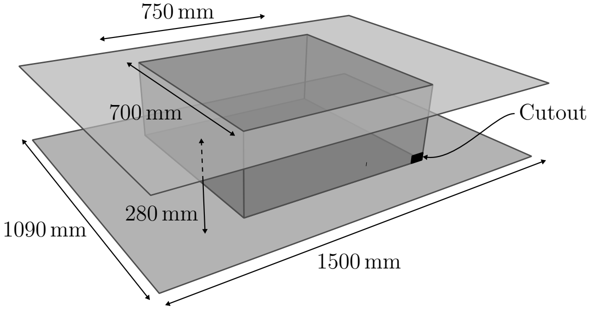

Figure 5.1: Model of the considered double hull structure with a box to contain the granules and a small cutout for filling.

margin in the case of higher forces due to granules or stiffener considering the capabilities of the test rig, which can apply a maximum load of 1200 kN.

The box containing the granules has the dimensions 750 mm × 700 mm and is welded to the two plates. The box consists of plates with a thickness of 3 mm. To be able to fill the granules into the double hull, a small hole is introduced at a corner of the box, which is closed after filling. The particles are filled into the structure by hand, without using any compaction device. By moving the structure during the filling process, it is ensured that no cavities are left. Thus, the experiment should be close to the proposed procedures in ship building.

This structure is welded to a rigid frame, as shown in Figure 5.2 and Figure 5.3. This frame – shown in orange – is considered and designed as fixed boundary conditions. Thus, it can be reused for the different experiments. Due to its high stiffness, a zero displacement boundary condition can be assumed for the finite element simulation later on. The cutouts which can be seen are for a digital image correlation (DIC) system. Further, a DIC system is used to monitor the displacement of the inner hull, so the frame is placed on four support beams to obtain a view from the bottom. A load cell is installed on each of these beams in order to measure the applied force.

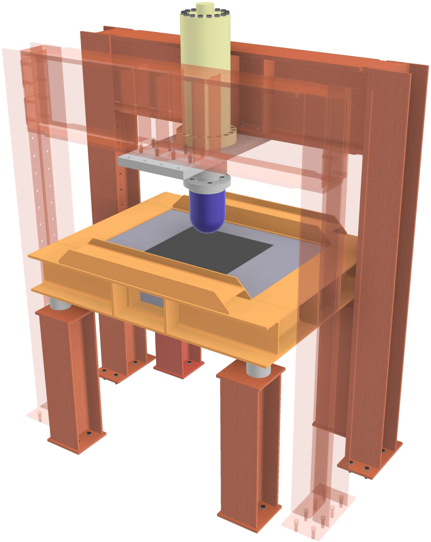

Figure 5.2: Experimental setup in the laboratory. The frame is placed on four columns to allow monitoring the inner hull with a DIC-System.

The indenter is depicted in blue in Figure 5.2. It is made of S355 from a solid block. The diameter of the indenter is 270 mm with a half-sphere as the bulbous bow. It is moved into the side hull structure with a constant velocity of 0.2 mm/s. Due to restrictions in the test rig – a maximum stroke length of 400 mm – an extension has to be installed during the experiment. For this, the experiment is stopped, unloaded, and continued. Thus, it is possible to drive the indenter to at least achieve rupture of the inner hull.

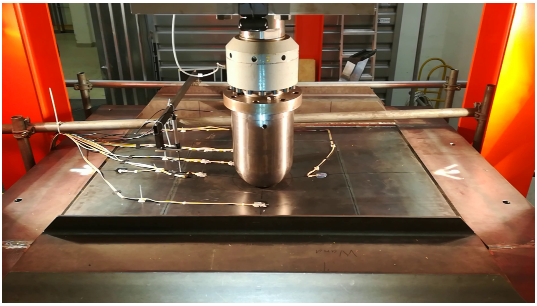

Figure 5.3: View on the experiment at the beginning of the penetration of the outer hull. Deformations and stresses are measured for comparison.

In addition to the load cells at the beams, the force applied to the indenter is measured. To verify the rigidity of the frame, its displacement and strain are measured at positions where the FEM computation predicted maximum values. Several strain and displacement sensors are attached to the side hull structure to determine the influence of the granules. As an important measurement quantity, the displacement of the centre of the inner hull and box should be mentioned. Apart from the applied force, they are the main comparison values for validation.

As mentioned before, four experiments were performed without a stiffener. The reason for this was a change in the boundary conditions. For the first two experiments, a horizontal movement of the frame was allowed. In the case of the filled box, this resulted in too large movements. Thus, the boundary conditions were changed to constrained movement in horizontal direction for all the following experiments, see Table 5.1.

Table 5.1: Overview over the experiments

Experiment	Box	Frame	Steel	Type
1	empty	free	Batch 1	–
2	Poraver 2-4	free	Batch 1	–
3	empty	fixed	Batch 2	–
4	Poraver 2-4	fixed	Batch 2	–
5	empty	fixed	Batch 2	Stiffener
6	Poraver 2-4	fixed	Batch 2	Stiffener
7	Danamol 30K	fixed	Batch 2	Stiffener

5.2 Experiments without stiffener

This section serves to discuss the experimental results. The experiments without granules are designed as reference experiments. As shown in Table 5.1, the first two experiments are carried out with unconstrained movement of the frame in horizontal direction. The idea behind this is to simulate the relatively free movement of ships – independent of each other – during a collision. In the subsequent two experiments, this was changed due to limitations in the test rig.

5.2.1 Experiment 1

This experiment is supposed to be the reference for the second experiment. Due to the symmetry of the hull structure, no or only little movement is expected in horizontal direction. Figure 5.4 shows the force-displacement curve. Here, and in all subsequent force-displacement curves, the calibrated sum of the four load cells at the corners will be shown. This means that only the applied force is measured, while the gravity loads are neglected. Further, it was checked that the results are in accordance with the force measured at the load cell of the indenter. Additional to that, the term *displacement* will be used for the movement of the tip of the bulbous bow, if not mentioned otherwise.

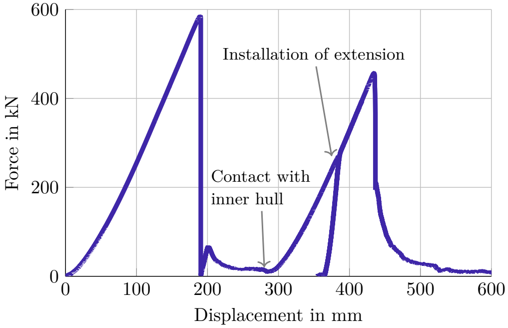

Figure 5.4: Force-displacement curve for the first experiment. The rupture of the two hulls can be clearly identified.

Having a general look at the plot, the rupture of the outer and inner hull can be clearly distinguished. It is also possible to make out where the indenter comes into contact with the inner hull at 280 mm. The unloading/loading path from the installation of the extension is shown in the plot at approximately 380 mm. The unloading leads to an elastic spring back, but the path is recovered very well during the continuation of the experiment.

In detail, the outer hull undergoes rupture at a maximum force of 580 kN and a displacement of 190 mm. A rather sudden rupture can be observed, with three cut lines developing immediately in radial direction. The branches originate in the regions of maximum stress and propagate up to the radius of the indenter, see Figure 5.5 [106, 155]. The sudden release of energy due to the immediate crack propagation results in a rapid deformation and decrease in force. Thus, the indenter can push through the structure easily until it comes into contact with the inner hull. The loading until rupture of the inner hull shows the same characteristic as the outer hull. The slope is similar, and the same stiffness is obtained. The rupture occurs at a total displacement of 435 mm. Originating from the time of contact with the bulbous bow, the inner hull ruptures after 155 mm and a force of

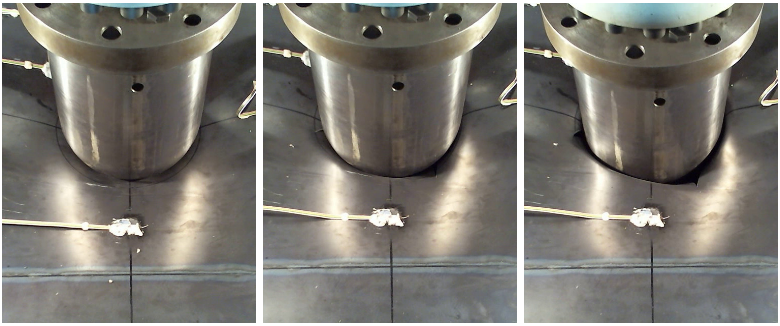

Figure 5.5: Development of the rupture, from left to right, for the outer hull in the first experiment.

460 kN. Compared to the outer hull, the crack propagation is slower. An initial cut appears at around 2/3 of the indenter radius. This crack grows slowly until a flap is formed, see Figure 5.6. This results in a slower drop in force, until the bulbous bow is driven through the whole structure. The pattern of black and white paint on the surface of the inner hull is used as a stochastic pattern to identify facets for the strain calculation with the DIC.

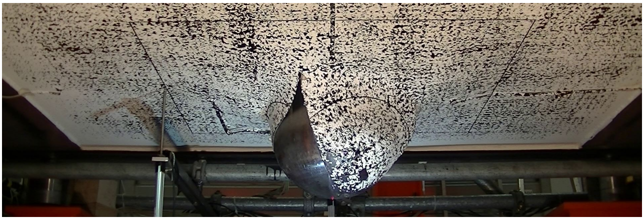

Figure 5.6: Flap occurring at the inner hull after rupture in the first experiment.

Recalling the setup, a similar rupture behaviour could be expected for the inner and outer hull. Comparing the measured strain values on the plates, both exhibit the same stress state. This is shown in Figure 5.7 left, which shows the strain in radial direction at a radius of 250 mm for the inner and outer hull. The displacement refers to the start of contact with the plate. As can be seen, both curves show similar behaviour until the strain gauge detaches due to too large deformations. A maximum strain of 40 % is measured using the DIC system, which is in the same range as measured in the tensile test in Section 4.5. The pattern observed with the DIC system – see Figure 5.7 right – can also be observed in [156, 157, 158], where Nakajima tests were performed. Thus, despite the fact that a sudden rupture propagation is observed for the outer hull, the rupture can be considered to be ductile. The inner hull shows a more typical rupture development for a ductile metal sheet [159, 160]. The location of the rupture initiation, compared to the radius of the indenter with respect to the size of the box, is similar to the results shown in [16]. There are various reasons for the different rupture behaviour. On the one hand, uncertainties related to the

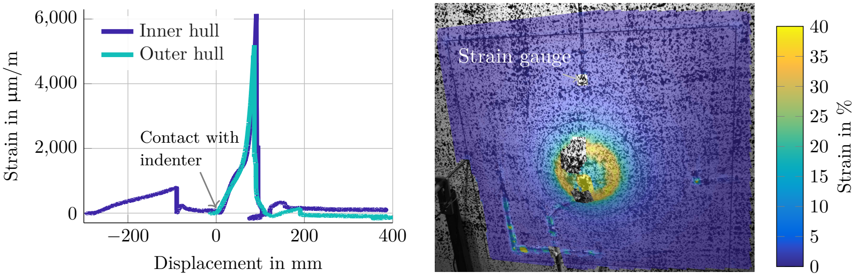

Figure 5.7: Comparison of the measured strain on the outer an inner hull, beginning at the contact with the indenter for each plate. The location of the strain gauge is marked in the DIC image on the right side.

steel could be a cause. The welding process of the structure might introduce residual stresses. Also, the tensile test results in the very first experiment surpass the standards for S235 significantly. Thus, the tensile strength was much higher than expected. On the other hand, the indenter was not used before. Thus, no sink holes or scratches could have led to initial damage on the surface of the plate during the transition through the outer hull. With regard to the other experiments, the rupture of the outer hull is rather unusual, which is why the force and displacement of the rupture have to be considered with caution.

As the last aspect, the displacement of the centre of the inner hull is considered. This is shown in Figure 5.8, where the displacement is plotted over the total displacement of the indenter. The first maximum, caused by the rupture of the outer hull, is located at the same displacement as in the force-displacement plot, Figure 5.4. In the case of the indentation of the outer hull, the displacement of the inner hull increases almost linearly until rupture. A maximum displacement of 28 mm is reached, and 26 mm are measured at the weld of the box to the inner hull. The displacement at the weld of the box to the outer hull is 27 mm, so the distance between the outer and inner hull is slightly reduced while the larger displacement at the centre is due to bending of the inner plate.

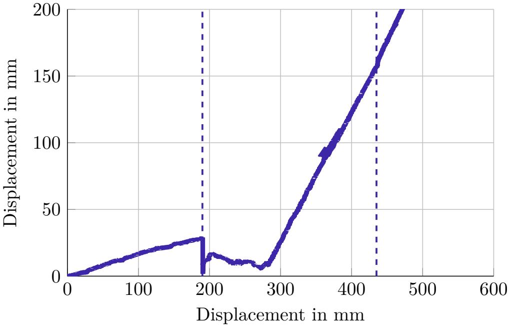

Figure 5.8: Displacement of the centre of the inner hull for the first experiment.

After rupture of the outer hull, a spring back can be observed. The remaining displacement due to plastic deformation of the side hull structure – remembering that the force drops to 0 kN after rupture – is approximately 10 mm. After the indenter comes into contact with the inner hull, the displacement follows the displacement of the bulbous bow in a linear manner. After rupture of the inner hull at 435 mm, the reference point for the measurement changes from the outer surface of the inner hull to the head of the bulbous bow, as can be seen in Figure 5.6.

5.2.2 Experiment 2

The second experiment uses *Poraver* as filling material in the box. In doing so, approximately 150 litre are filled into the box without using any advanced compaction mechanism, as described before. The obtained force-displacement curve is shown in Figure 5.9. The outer hull fractures at a displacement of 135 mm and a force of 460 kN. The rupture behaviour is similar to the mechanism observed in Experiment 1 for the inner hull. A crack is initiated at around 2/3 of the indenter radius. This can be seen in Figure 5.10 top left. This is in a good agreement with the experiments for rectangular plates [161]. As for the inner hull in Experiment 1, compare with Figure 5.6, a flap develops, which can be seen in the subsequent images in Figure 5.10.

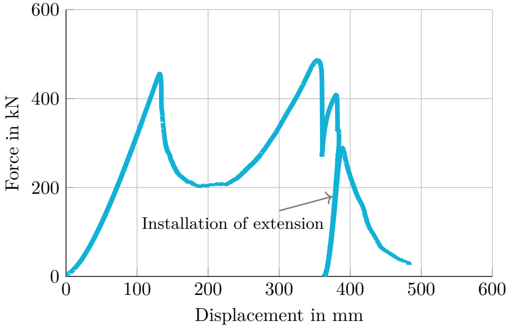

Figure 5.9: Force-displacement curve for the second experiment, where *Poraver* is filled into the box.

The granules between the outer and inner hull result in a higher stiffness before rupture of the outer hull, compared to Experiment 1. After rupture, the flap is clamped between the indenter and the granules. Therefore, it is dragged into the box, instead of being pushed away. This results in an increase in resistance force, as can be observed in the force-displacement plot between a total displacement of 135 mm and approximately 250 mm compared to Experiment 1. Here, the force remains around 200 kN, while the indenter moves through the box.

Due to the granules, an additional layer is added between the indenter and inner hull. At approximately 230 mm, we can observe an increase in force. Assuming that the granules will not show large movement orthogonally to the indentation direction, the granules are compacted over 80 %. Recalling the results from the uniaxial compression test – see Section

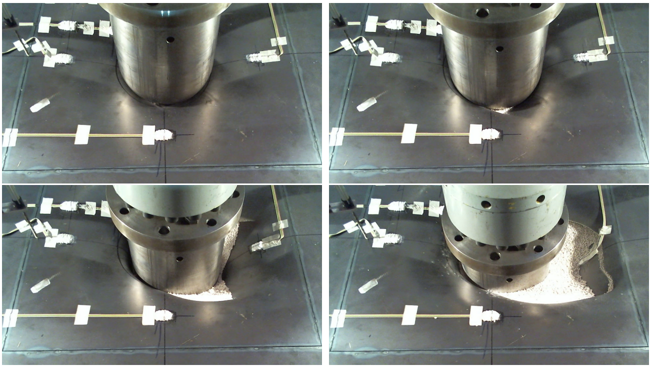

Figure 5.10: Rupture of the outer hull with granules during the indentation process (from top left to lower right). A metal flap is clamped between the granules and the indenter.

4.4.2 – they can carry a significant load and transfer the movement of the indenter to the inner hull. At the end of the indentation process, the granules are compressed to a fine powder, shown in Figure 5.11. Going back to the force-displacement curve, it is possible to observe a rupture of the flap from the outer hull at a displacement of 360 mm, as depicted in Figure 5.10 bottom right. Eventually, the inner hull ruptures at a total displacement of 380 mm with an applied force of 410 kN.

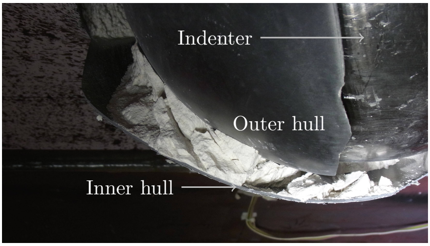

Figure 5.11: Close view at the clamped flap after the experiment. The granules formed a layer between the outer and inner hull.

A closer look at the granules reveals the following behaviour. The particles, which are in direct interaction region with the indenter and flap are highly compressed, as can be seen in Figure 5.11. Then again, intact particles can be found at the side of the box, see Figure 5.10 top right. This leads to the conclusion that only the particles in the direct path of the indenter are compressed and that there is no (or only very little) particle movement orthogonal to the movement of the indenter. Thus, most of the energy is transferred to the inner hull and not to the side of the box. This can also be seen looking at the deformation of the side shells of the box. For Experiment 1 and 2, the displacement is similar. An examination of the granules after the experiment shows that roughly 50 % of the particles are still intact.

As mentioned in the description of the experiments, horizontal movement of the frame is possible. Due to the non-symmetric rupture – as shown in Figure 5.10 – the frame, and therefore the double hull structure, slides in horizontal direction. In total, a horizontal movement of 30 mm could be observed. This results in a nonsymmetric contact with the inner hull.

Comparison with Experiment 1 The improvements in crashworthiness compared to Experiment 1 will be discussed. Therefore, the focus lies on the dissipated energy until the rupture of the inner hull. Since the elastic energy stored in the system is very small, see the displacement during the installation of the extension, the total energy introduced into the system is considered – which is, in case of a collision, relevant for the counterpart. Figure 5.12 shows a plotting of energy over displacement. The vertical lines indicate the rupture of the outer and inner hulls. Looking at Experiment 1 – without granules – it is possible to observe an energy increase until rupture of the outer hull, followed by the transition through the box with almost no increase in energy until the bulbous bow undergoes contact with the inner hull. Then again, an increase in energy can be observed until rupture of the inner hull. In total, 82 kNm are applied to move the indenter through the structure.

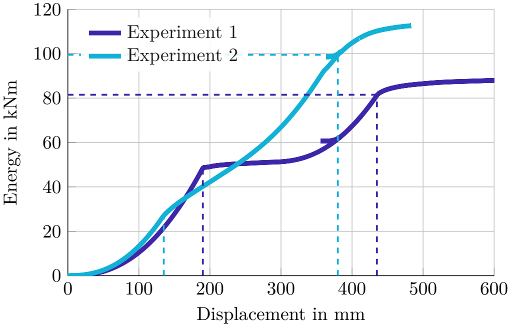

Figure 5.12: Energy dissipation during the experiment. The vertical lines indicate the rupture of the outer and inner hull, respectively. Experiment 2, filled with granules, can absorb more energy before rupture of the inner hull.

In Experiment 2 the resistance of the outer hull – or total stiffness of the whole structure – is higher. Thus, at the same displacement, more energy is needed. As stated before, the rupture of the outer hull occurs at a smaller total displacement. Other than in Experiment 1, the energy still increases due to the granules and the flap, as described before. In contrast to Experiment 1, there is no clear indication when the inner hull starts to counteract the bulbous bow. The tear of the flap can be observed as a bend in the curve, at 360 mm. At the final rupture of the inner hull, at a displacement of 380 mm, an energy of 100 kNm is applied to the structure. Note that the installation of the extension occurs shortly after the rupture, see Figure 5.9. Since the unloading path is recovered very well, this has no effect on the energy calculation. Compared to Experiment 1, the increase in energy after rupture of the inner hull is larger, due to the flap which interacts with the granules and the inner hull.

Despite the fact that the inner hull of Experiment 2 ruptures earlier, the structure filled with granules can absorb more energy. Here, an increase of 22 % can be observed. This outcome strongly depends on the position of the ruptures. The late rupture of the outer hull for the first experiment mitigates the potential. Assuming a rupture at a similar position as observed for the other shells, the plateau would be reached earlier and, thus, less energy would be needed for the empty double hull.

Figure 5.13 shows the displacement of the centre of the inner hull. The support of the inner hull during the indentation process can be seen. As in a sandwich plate, the granules transfer the load to the inner hull, resulting in a larger displacement compared to Experiment 1 until the outer hull ruptures. At rupture of the outer hull – marked with a light blue vertical line – the increase in displacement is approximately 15 mm. Thus, considering the conclusions above with regard to the particle movement, the result is a compaction of 37 % in the granules between the indenter and inner hull. In this compaction region, the granules start to carry a reasonable amount of load. Thus, we do not observe a spring back of the inner hull after the rupture for the experiment with granules.

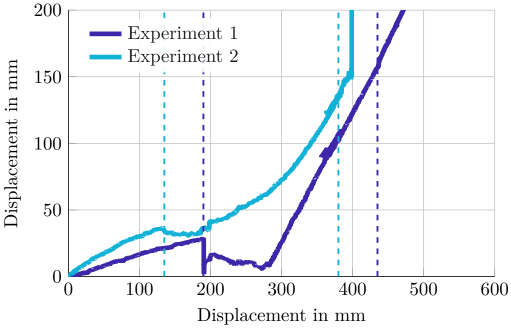

Figure 5.13: Comparison of the displacement of the centre of the inner hull. The granules lead to a higher deflection of the inner hull.

Continuing the translation through the box, the granules are highly compacted, and a layer with a thickness of approximately 30 mm of fine granular powder is created between the indenter and inner hull. This can be seen in Figure 5.11. The additional layer reduces the difference of 55 mm total indenter displacement for the location of the rupture of the inner hull. Comparing the local deflection of the inner hull, the difference reduces to 25 mm. In this state, the slopes of the two curves are very similar. This indicates that the breakage and pulverization of the particles ended, so that they form a non-compressible powder acting as an additional layer. Compared to the uniaxial compression test in Section 4.4.2, an almost vertical slope can be seen in the high compression region – as shown in Figure 3.2.

The chosen setup – allowing movement in horizontal direction – results in an nonsymmetric loading for the Experiment 2. This perhaps leads to a reduced resistance against penetration. This could be an additional cause for the differences in rupture behaviour of the inner hull.

5.2.3 Experiment 3

The horizontal movement for Experiment 2 and, thus, the unsymmetrical loading of the inner hull, suggest a change in boundary conditions, which is done for all subsequent tests. Thus, the horizontal movement of the frame on the load cells is hindered. Repeating the experiment with the same setup as for Experiment 1 and 2 will also allow for a closer look at the rupture behaviour of the plates, giving a better understanding of the unexpected rupture behaviour of the outer hull in Experiment 1.

As mentioned in Section 4.5, the same steel grade is used, but the steel plates are from different manufacturing batches. Thus, the parameter of the steel differs, thus only allowing for a qualitative comparison to Experiment 1 and 2.

Figure 5.14 shows the force-displacement curve. For Experiment 3, the force increases while moving into the outer hull up to a displacement of 150 mm. There, at a total force of 390 kN, the hull ruptures. Compared to Experiment 1, the rupture differs. Here, a slow crack growth occurs, as shown in Figure 5.15. Nonetheless, the pattern of the rupture is similar to that in Experiment 1, Figure 5.5. Due to the ongoing crack propagation,

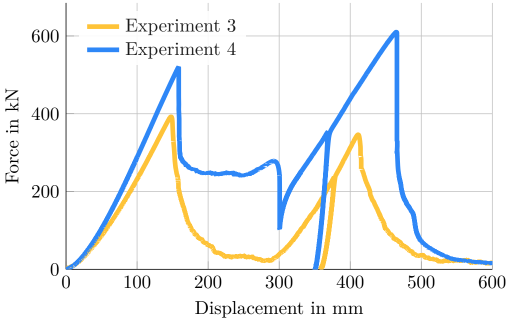

Figure 5.14: Force-displacement curves of Experiment 3 – without granules – and Experiment 4 – with granules.

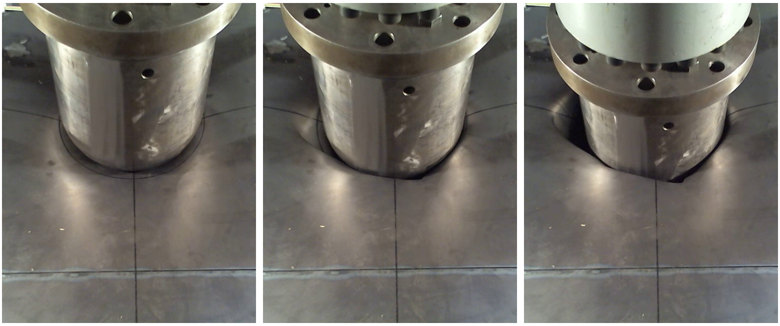

Figure 5.15: Rupture behaviour of the outer hull for Experiment 3.

we observe a slower drop in force, since the indenter has to shear the metal sheet. The contact with the inner hull can be identified due to the increase in resistance force at a displacement of 280 mm. The unloading path of the extension is recovered very well during the indentation of the inner hull. Finally, the structure ruptures at a displacement of 410 mm and a force of 340 kN. Compared to Experiment 1, the crack growth is similar. It initiates at around 2/3 of the indenter radius and grows slowly. Eventually, a flap is formed, see Figure 5.16 left, which is similar to Figure 5.6.

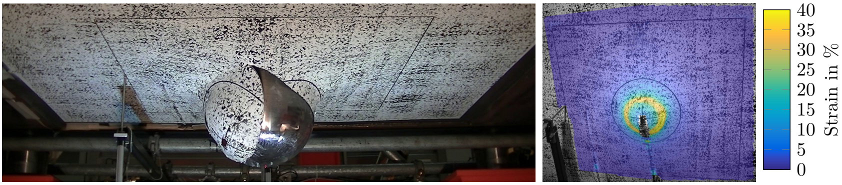

Figure 5.16: Rupture mechanism of the inner hull for Experiment 3 (left) and the strain pattern immediately before rupture (right).

With regard to the outer and inner hull, the strain pattern is very similar to the one in Experiment 1. The strain concentration of the inner hull before rupture is also circular, see Figure 5.16 right, and similar to the pattern obtained in Experiment 1, see Figure 5.7 right. A maximum strain of 40 % is measured using the DIC. Thus, the same statements regarding the rupture behaviour as in Section 5.2.1 can be made.

The displacement of the centre for the inner hull is similar to Experiment 1 and will be discussed in detail in the comparison with Experiment 4 in the next section.

5.2.4 Experiment 4

The force-displacement curve is given in Figure 5.14. The increase in stiffness of the structure can be observed for this experiment compared to Experiment 3. The rupture of the outer hull is nearly at the same displacement, here 160 mm, but with a higher force of 520 kN. After rupture of the outer hull, the resistance against indentation is on a high level. The granules counteract to the indenter and, as in Experiment 2, a flap is clamped between the indenter and the granules. Thus, the force needed to move through the box is around 250 kN. The drop in force at a displacement of 300 mm is due to the rupture of this flap. The process of the growth can be seen in Figure 5.17. Compared to Experiment 2, the flap is a bit smaller, but the development is similar.

After rupture of the flap, the force increases. The unloading path during the compression of the inner hull can be recovered very well. Compared to Experiment 2, the inner hull can withstand a much higher force before rupture. A displacement of 470 mm and total force of 600 kN is reached. Due to the high force – and, thus, a considerable amount of energy in the system – the crack grows faster than that in Experiment 3. However, as for the other experiments, a flap is created, see Figure 5.18. Due to the changed boundary conditions, the inner hull is loaded in its centre.

Figure 5.18 shows the additional layer due to the granules. Its thickness is approximately 20 mm.

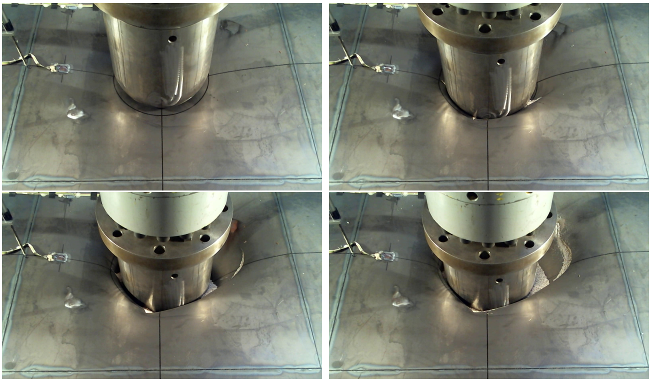

Figure 5.17: Rupture of the outer hull for Experiment 4, from top left to bottom right. Due to the granules, the outer hull is clamped and torn off.

Figure 5.18: Rupture pattern of the inner hull in Experiment 4 after breakage (left) and before (right).

Comparison with Experiment 3 To estimate the improvements, it is necessary to take a look at the dissipated energy in Figure 5.19. The vertical lines indicate the rupture of the outer and inner hulls. A plateau is observed in Experiment 3 – as already seen in

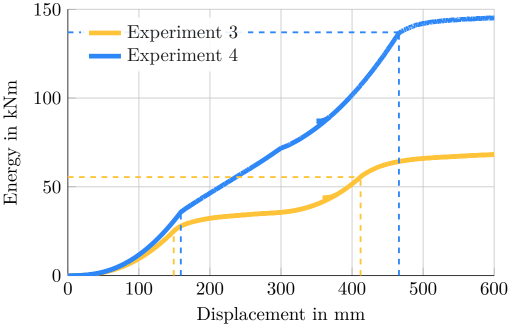

Figure 5.19: Dissipated energy for Experiment 3 – without granules – and Experiment 4 – with granules.

Experiment 1 – after rupture of the outer hull before the indenter comes into contact with the inner hull. Until the rupture of the inner hull at 410 mm, an energy of 56 kNm is induced into the structure.

The improvements due to the filling with granules can also be observed for Experiment 4. The stiffness of the entire structure is increased, leading to a higher energy dissipation until rupture of the outer hull for Experiment 4. Thereafter, a significant amount of energy has to be used to move through the granules and the box. The tear of the flap can be observed as a bend at 300 mm, but the energy increases until the rupture of the inner hull occurs. In total, 140 kNm is applied. Comparing Experiment 3 and 4, this is an increase of approximately 150 %. This large increase benefits from the late rupture for Experiment 4. Taking the additional layer into account, the difference in local deflection for the inner hull is 80 mm.

The behaviour of the inner hull at the centre location can be seen in Figure 5.20. For Experiment 4, the additional support due to the granular material can be clearly identified. After rupture of the outer hull and rupture of the flap, the deflection of the centre point changes only marginally. Thus, the granules transfer a significant amount of load to the inner hull. And – as for Experiment 2 – the particles appear to be pulverized completely under the indenter.

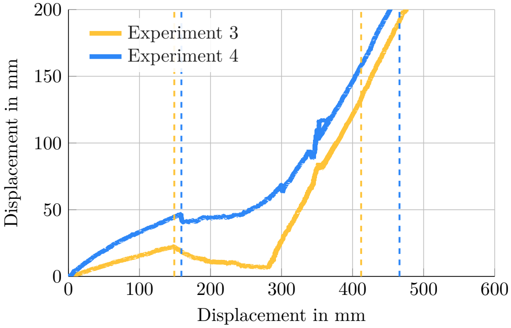

Figure 5.20: Displacement of the centre of the inner hull for Experiment 3 and 4. In Experiment 4, the granules lead to a larger deflection and a higher load transfer to the inner hull.

5.2.5 Conclusion for experiments without stiffener

A closer look at all four experiments provides the basis for a summary. The resulting displacement, force, and energy for each experiment and the respective outer and inner hull are shown in Table 5.2.

First, the rupture behaviour of the shells itself is considered. The displacements at which the ruptures occur are u_{ind} for the outer hull and u_{local} for the inner hull. Here, only the relative displacement is considered, meaning the movement of the centre point of the plate, taking into account the additional displacement introduced due to granules. Two shells stick out and undergo large displacements: on the one hand, the outer hull in Experiment 1, and on the other hand the inner hull in Experiment 4. All other shells rupture in the

Table 5.2: Overview over rupture positions and dissipated energy for Experiments 1 to 4.

	Outer hull			Inner hull				
Exp	u_{ind}	$F_{u,ind}$	$E_{u,ind}$	u_{ind}	u_{gran}	u_{local}	$F_{u,ind}$	$E_{u,ind}$
1	190 mm	580 kN	49 kNm	435 mm	–	155 mm	460 kN	82 kNm
2	135 mm	460 kN	28 kNm	380 mm	30 mm	130 mm	410 kN	100 kNm
3	150 mm	390 kN	25 kNm	410 mm	–	130 mm	340 kN	56 kNm
4	160 mm	500 kN	35 kNm	470 mm	20 mm	210 mm	600 kN	140 kNm

range of 130 mm to 160 mm. This coincides with a high application of force. Thus, the results in energy dissipation for these shells have to be treated with caution.

The high force applied in Experiment 4 results in a higher compression of the granules compared to Experiment 2. Thus, the resulting layer u_{gran} is narrower. However, as this occurs in a region over 80 % of compression, the load-carrying capacity of the granules is very high.

The aim of filling the box with granules was to increase the dissipated energy until the inner hull ruptures. This could be observed here. Considering the rupture behaviour of the two plates mentioned before, the increase lies between 22 % and 150 %. This discrepancy can be resolved by assuming an averaged rupture behaviour for the shells. Assuming a similar rupture behaviour for the outer hulls in Experiment 1, compared to the other shells, the dissipated energy would be smaller. Thus, the improvement will change to approximately 60 %. The same assumption can be made for the inner hull of Experiment 4, which will then decrease the introduced energy. In doing so, the increase in energy compared to Experiment 3 will be reduced to approximately 90 %.

To give a more reliable estimation, more tests would be needed to average over the repeated experiments. Then, a closer look at the rupture behaviour would be mandatory, because this is to be seen as the critical event regarding the energy dissipation until rupture. However a realistic assumption of an increase of 60 % can be noted. Nonetheless, the primary ideas of the filling with granules can be confirmed. The load transfer from the outer hull to the inner hull is clearly visible, due to the increase in stiffness of the whole structure during loading the outer hull. Further, the crushing and compression of the granules in the near field of the indenter is observed, leading to an increase in energy dissipation. An aspect not considered before is the additional effort to tear off a flap from outer hull, which is clamped between the indenter and the granules.

5.3 Experiments with stiffener

In order to examine the influence of granules on webs, stringers, and other reinforcement structural elements, the influence of stiffeners is investigated. As described in Section 5.1, the dimensions of the experiment are related to the setup in [20]. There, several beams are used to obtain a realistic side hull structure. In order to reduce the complexity, a different approach is chosen: only one stiffener is applied, parallel to the long side of the side hull structure. Similar experiments are conducted in [29], where one or two stiffeners are investigated.

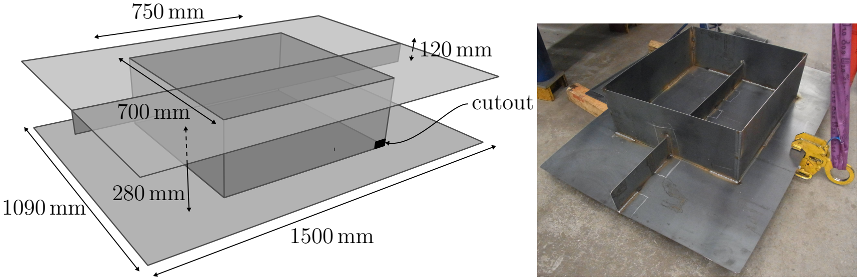

Figure 5.21: Model of the double hull structure with stiffener (left) and specimen for the experiment (right).

The changes in the structure can be seen in Figure 5.21.The model is shown on the left side. A stiffener, with a thickness of 3 mm, is connected to the outer hull. The stiffener has a depth of 120 mm and is made from the same steel plate as the side hull structure. In order to go through the box, cut outs were introduced to the box, as can be seen in Figure 5.21 right. All parts were welded together using the weld pattern seen in the image.

The idea to use one stiffener is motivated by looking at the buckling behaviour of a flat stiffener. Experimental results from [29] can be seen in Figure 5.22, where a single stiffener was used If the bar is in direct contact with granular material, this may result in an increased resistance against buckling. Thus, the flat stiffener contributes to protecting the connected outer hull against penetration. The resistance moment of a flat bar is smaller at the same height, compared to a P-bar or T-beam. Thus, the result will be more dependent on the influence of the granules.

Figure 5.22: Deformation of a single stiffener as can be seen in [29] (from [29]).

5.3.1 Experiment 5

To obtain reference data, an experiment without granules is performed. Thus, only the side hull structure with a stiffener at the outer hull is indented with the bulbous bow. As for Experiment 3 and 4, no movement in horizontal direction is allowed. The resulting force-displacement curve is shown in Figure 5.23. For comparison, the curve from Experiment 3 without stiffener is shown as well. Compared to the experiment without a flat bar, an increase in stiffness can be observed for the outer hull. The flat bar starts to buckle after

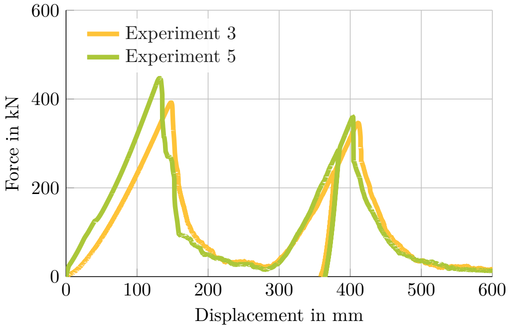

Figure 5.23: Comparison between Experiment 3 and 5, both without granules. The increase in stiffness for the outer hull is clearly visible for Experiment 5.

40 mm, which can be observed due to the kink in the curve. The rupture of the outer hull happens at a displacement of 130 mm and a force of 450 kN. The development of the rupture can be seen in the images in Figure 5.24. The first crack develops parallel to the stiffener, and another branch in the direction of the camera. At this state, the stiffener is still intact. At approximately 140 mm, the stiffener ruptures into two pieces. In more detail, this can be seen in Figure 5.25. In the middle, the structure without the bulbous bow is shown. The stiffener is pushed away from the camera and then ruptured. In the left and right image, the bulging of the stiffener can be seen. This is similar to the results shown in [29].

After the rupture of the outer hull, the loading path is similar to Experiment 3 – which is logical, since the difference due to the stiffener mainly affects the outer hull. The rupture of the inner hull occurs at a displacement of 405 mm with a force of 360 kN. Concerning the rupture pattern, a similar picture as in Experiment 3 is observed, see Figure 5.16.

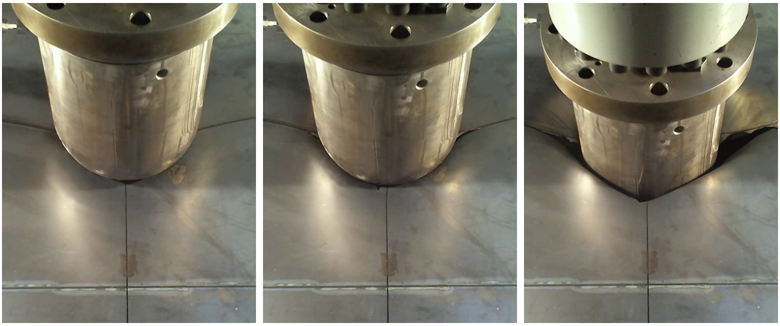

Figure 5.24: Rupture of the outer hull for Experiment 5.

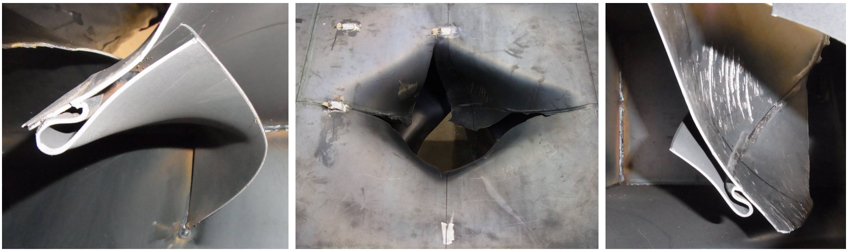

Figure 5.25: Rupture of the stiffener in Experiment 5. Shape of the outer hull after removal of the indenter (middle). The folding of both ends of the stiffener can be seen in the left and right image.

5.3.2 Experiment 6

The sixth experiment uses *Poraver* as filling material. Due to the additional bar inside the box, the filling process uses a second hole in the corner of the box. This way, it is possible to ensure that no voids remain near the stiffener. The obtained force-displacement curve for this experiment is shown in Figure 5.26. The outer hull fractures at a displacement of 125 mm and a force of 475 kN. The rupture mechanism is similar to the other experiments with granules, as can be seen in Figure 5.27. A crack is initiated on the left-hand side at around 2/3 of the indenter radius. This crack then propagates in circular direction and cuts the stiffener, such that a flap is created, which can be seen in the subsequent images. This flap ruptures from the outer hull at a displacement of 340 mm and a force of 480 kN. The flap is clamped between the indenter and the granules, see Figure 5.28. This results in a nonsymmetric deformation for the inner hull, as can be seen in Figure 5.29 left. In fact, the flap is dragged with the indenter during the penetration of the inner hull, as can be seen in the right image of Figure 5.28.

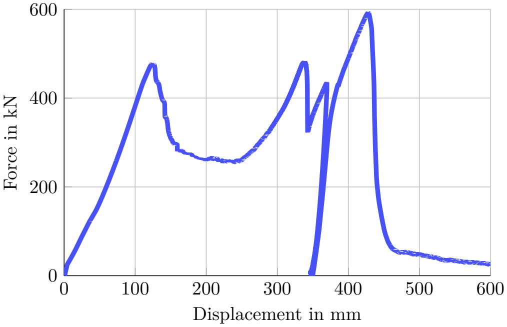

Figure 5.26: Force-displacement curve of Experiment 6 with granules and stiffener.

During the transition through the box and the granules, the applied force is at a high level. After the rupture of the flap, unloading is performed to install the extension. The

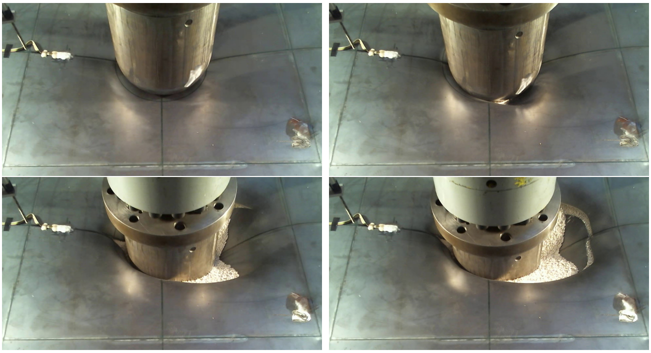

Figure 5.27: Development of a flap due to clamping of the outer hull in Experiment 6.

Figure 5.28: Ripped outer hull after indentation of the inner hull (left). The remaining flap in the inside of the box can be seen in the right image.

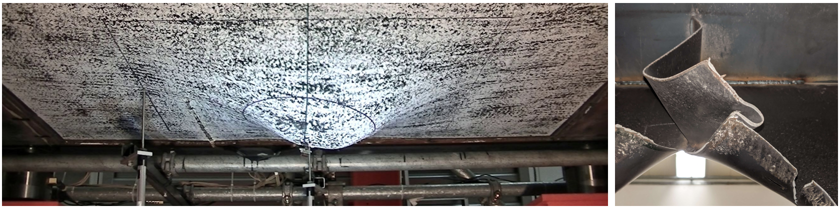

Figure 5.29: Nonsymmetric deformation of the inner hull (left) and shape of the stiffener after rupture (right).

path is recovered very well for lower forces, but there is a slight mismatch at the end of the reloading. This is probably caused by repositioning the flap during the unloading process.

The inner hull ruptures at a total displacement of 430 mm and a force of 590 kN. Due to the granules, an additional layer of approximately 20 mm has built up.

Comparison with Experiment 5 Figure 5.30 shows a plot of the energy over the displacement. As before, the vertical lines indicate the rupture positions of the shells. During the loading of the outer hull, Experiment 6 – with granules – only requires a very small amount of additional energy. Further, as in the first four experiments, we observe an increase in energy after the rupture of the outer hull, while Experiment 5 remains on a plateau. The detachment of the flap can be observed as a bend in the curve. Finally, the introduced energy until rupture of the outer hull is 136 kNm for Experiment 6 and 60 kNm for Experiment 5, respectively. This is a significant increase of 126 %. The rupture position for the outer hull is nearly the same. Thus, this result is strongly dependent on the displacement of rupture for the inner shell. However, the advantage during the translation through the box is clearly visible.

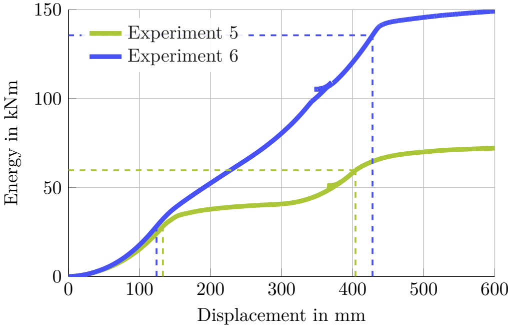

Figure 5.30: Dissipated energy for the experiments with stiffener, with and without granules.

The displacement of the centre of the inner hull is shown in Figure 5.31. During the first millimetres of the indentation, there is no difference between Experiment 5 and 6. Then, the inner hull undergoes an additional displacement with the granules. After rupture of the outer hull, the experiment with granules maintains the loading on the inner hull, while

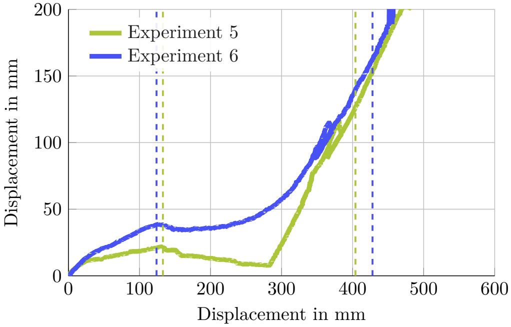

Figure 5.31: Displacement of the centre of the inner hull for Experiment 5 and 6.

Experiment 5 reduces its load. During the loading of the inner hull, the layer of granules decreases. This seems to happen because the flap – see Figure 5.28 right – is not clamped during the whole indentation process. Thus, the particles are dragged away.

5.3.3 Experiment 7

As the last aspect, the filling of the structure with a different type of granules will be investigated. To do so, *Danamol* is chosen. This material is chosen because its experimental results – see Section 3.1 – differ significantly from *Poraver*. Due to its different bulk density and void ratio, the increase in load carrying capacity is different. Thus, we expect a higher stiffness for the entire structure, resulting in more energy dissipation. The research question to be answered is whether the stiffer granules lead to a thicker layer of granules and therefore result in an earlier rupture of the inner hull.

The force-displacement curve of this experiment can be seen in Figure 5.32. The outer hull ruptures at a displacement of 140 mm and a force of 620 kN. The stiffness of the structure until there is similar to the experiment with *Poraver* as filling material. After the initial rupture of the outer hull, the rupture develops differently from the experiments before, which can be seen in Figure 5.33. A flap is observed, clamped between the indenter and the granules, but the rupture of the flap does not only occur at the surface of the outer hull far to the indenter. There is also an additional crack growing under the indenter, covered by the granules in the images. Eventually this smaller flap ruptures at a displacement of 300 mm and a force of 610 kN. During the transition through the box, the force rises fast, leading to the conclusion that the granules and flap carry a lot of load.

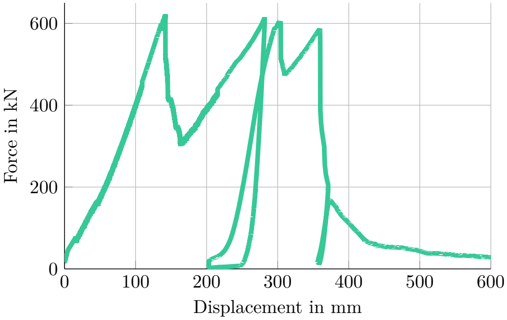

Figure 5.32: Force-displacement curve for the box with stiffener and *Danamol* as filling material.

Eventually, the inner hull ruptures at a displacement of 360 mm and a force of 590 kN. Due to the flap from the outer hull, the loading is slightly nonsymmetric, as can be seen in Figure 5.34. The rupture pattern of the inner hull is similar to the other experiments.

Comparison with Experiment 5 and 6 The energy dissipation is shown in Figure 5.35. *Danamol* further increases the stiffness of the entire structure penetrating the outer hull. After rupture, the energy needed to drive through the granules and tear off the plate is

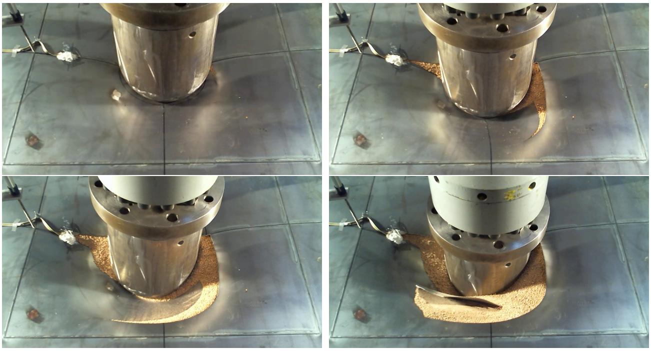

Figure 5.33: Rupture pattern of the outer hull, from top left to bottom right, during the indentation process.

Figure 5.34: Nonsymmetric deformation of the inner hull with *Danamol* (left) and the final shape of the stiffener (right).

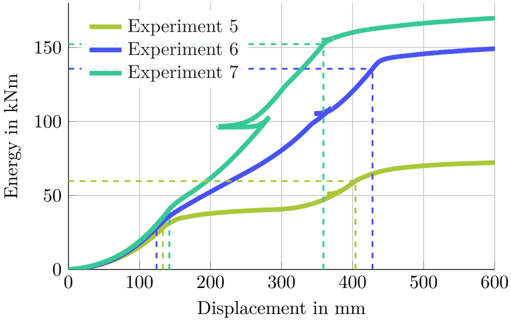

Figure 5.35: Dissipated energy for the experiments with stiffener. *Danamol* results in a faster increase, but the inner hull ruptures earlier than with *Poraver*.

higher. Finally, a rupture energy of 152 kNm for the inner hull is reached. This is an increase of 153 % compared to the empty box – Experiment 5 – and 12 % compared to Experiment 6.

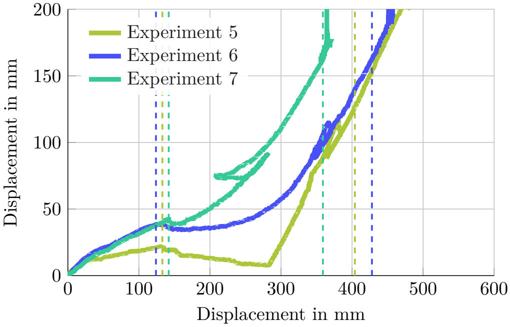

Figure 5.36: Displacement of the centre of the inner hull. Experiment 7 shows a thicker layer of granules using *Danamol* compared to Experiment 6.

A big difference between the two granules can be observed looking at the displacement of the centre of the inner hull, see Figure 5.36. While the path of the indentation of the outer hull is similar to Experiment 6, it seems like the granules can transfer a lot more load to the inner hull afterwards. The spring back after rupture is smaller and the compaction of the layer is marginal. Thus, the additional layer between the inner hull and the indenter has a thickness of approximately 80 mm. This explains the early rupture of the inner hull in terms of total displacement.

5.3.4 Conclusion of experiments with stiffener

The increase in energy dissipation for the experiments with filled double hulls is more than factor two. The relevant quantities of the experiment are summed up in Table 5.3. To begin with, the rupture behaviour of the shells is considered. The displacement of the centre of the plate is given by u_{ind} for the outer hull and u_{local} for the inner hull, respectively. The rupture position is very similar in all three experiments, resulting in a good comparability regarding the transition through the box and the granules. The local deflection is in the same range as for Experiments 1 to 4, see Table 5.2. Based on the small data basis, it was possible to ascertain a tendency towards earlier rupture for structures with a stiffener, which was also observed in [29, 26].

Table 5.3: Overview over rupture positions and dissipated energy for Experiments 5 to 7.

	Outer hull			Inner hull				
Exp	u_{ind}	$F_{u,ind}$	$E_{u,ind}$	u_{ind}	u_{gran}	u_{local}	$F_{u,ind}$	$E_{u,ind}$
5	130 mm	450 kN	28 kNm	405 mm	–	125 mm	360 kN	60 kNm
6	125 mm	475 kN	28 kNm	430 mm	20 mm	170 mm	590 kN	136 kNm
7	140 mm	620 kN	41 kNm	360 mm	80 mm	160 mm	590 kN	152 kNm

The increase in stiffness results in a higher force at this displacement for the box with granules. *Danamol* seems to be stiffer than *Poraver*. Thus, the energy until rupture of the outer hull increases over the experiments.

Looking at the inner hull, a larger local displacement can be observed before rupture. Experiment 6 and 7 undergo over 160 mm in displacement, while the reference Experiment 5 ruptures after 125 mm. This was also observed in Experiment 3 and 4, where the same steel was used. This indicates that the additional layer due to the granules mitigates effects that lead to rupture. On the one hand, the layer prevents direct contact between the bulbous bow and the inner hull. Thus, defects on the indenter surface cannot trigger scratches on the surface of the inner hull. On the other hand, it could act as a lubricating film, such that the load on the shell is distributed more evenly. Since the granules are compressed to a fine powder, they cannot harm the steel surface.

The additional layer due to the granules is much thicker for *Danamol*. This coincides with the experimental results for the uniaxial compression test in Section 4.4.2. *Danamol* undergoes a maximum compression of 70 %, while *Poraver* is compressed 90 %.

Considering the dissipated energy for the whole structure until rupture of the inner hull, the difference between the two granules is smaller. The higher force against penetration in Experiment 7 is reduced due to the lower indentation depth of the indenter. This is caused by the thicker layer of granules in this experiment. Thus, the higher bulk density and lower void ratio of *Danamol* increases the stiffness at the cost of indentation depth. Depending on the counterpart of the collision, this could be a crucial factor, since it is forced to decelerate faster.

To sum up, an increase of 126 % in energy dissipation is obtained for the granular material *Poraver*, which is in the same region as for Experiment 1 and 2, where no stiffener were used. Using *Danamol* as filling material, an improvement of 153 % can be obtained. As seen before in the experiments, the outcome strongly depends on the rupture behaviour of the shells. Comparing the results using stiffeners with the results using no stiffener, it appears that the influence of the granules is higher. Thus, the combination of an increase in resistance – due to the load transfer – and the prevention of buckling appears to be very promising, and a positive effect on the buckling behaviour of the flat bar can be assumed.

Based on these two experiments, it cannot be recommended to use *Danamol* as a filling material instead of *Poraver*. The slight improvement in energy dissipation comes at the cost of a lower indentation depth – which may affect the collision counterpart. Furthermore, the mechanical properties of *Poraver* are superior to *Danamol*. The lower bulk density and its chemical properties make it more suitable for a ship side hull structure.

6 Numerical investigation

After obtaining the experimental results, the modelling of the collision behaviour is the second main part of this thesis. As stated in the introduction, the focus lies on the FEM. In doing so, it is possible to compute large structures in reasonable time. For this purpose, the experiments are modelled and simulated using two different material models for the granules, as described in Section 2.1. A brief overview over some of the numerical results for Experiment 1 to 4 is presented in [106].

After determining the potentials and drawbacks of the FEM approach, a more realistic side hull structure will be evaluated numerically. In doing so, the aim is to investigate the effects occurring due to more stiffeners. Furthermore, possible changes in the geometry will be evaluated. Here, the application of granules can be used to reduce the double hull width without decreasing the energy dissipation compared to the original geometry.

6.1 Simplified side hull structure

The simplified side hull structure from Chapter 5 will be investigated numerically. This is done using the finite element software *Abaqus* [72]. An explicit time integration method is applied – which is a common choice for crash and impact simulations. It can handle non-linearities due to material models, rupture, and friction, and the small time resolution is favourable for comparisons with experimental data.

The initial model used for the calculations is shown in Figure 6.1. This model has been used to design the experimental setup with material data from [29] and to perform a mesh study. The frame – in orange – was designed in such a way that it can be assumed to be rigid. Thus, it is omitted in later calculations and replaced with fixed boundary conditions.

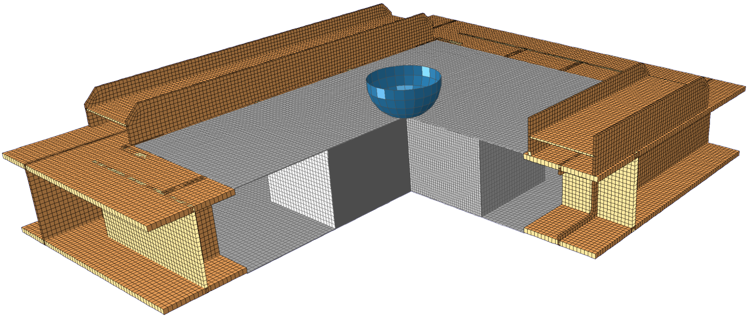

Figure 6.1: Finite element model used in computation. The orange frame around the hull structure can be neglected, since it can be assumed to be rigid.

A mesh study, performed a priori, results in the shown mesh with a total amount of 18524 elements for the double hull structure and 147000 elements for the granules. Due to the nonsymmetric rupture of the plates, the symmetry seen in Figure 6.1 cannot be used – and it is necessary to consider a full model. On the one hand, the computational cost is reduced due to omitting the frame, but, on the other hand, is increased by using a full model. Eventually, only the box, in grey, the granules, and the indenter are considered in the simulation.

The steel parts are modelled using four-noded shell elements with reduced integration, five integration points through the thickness, and a Reissner-Mindlin formulation. The material parameters are obtained in Section 4.5. The granules are modelled using continuum elements – here eight-noded hexahedral elements – with reduced integration. The material models in use are either Mohr-Coulomb or hypoplastic material behaviour, see Section 2.1. An analytical description is used for the indenter, thus assuming it to be rigid. In doing so, the computational cost is reduced due to fewer elements and due to a simplified contact detection.

The contact between the different parts is enforced with a predictor/corrector algorithm, see [73]. In normal direction, no penetration is allowed, and a frictional contact is assumed in tangential direction, based on the friction coefficients given in Section 4.3.

To reduce the computational cost, the time span of the indentation is reduced. In the experiments, the indenter moved with a velocity of 0.2 mm/s, allowing for an adequate data acquisition and for reaction time in the case of an unexpected event. Here, the entire indentation process is simulated in a smaller time period. In doing so, a quasi-static behaviour is observed, as for longer time spans, without introducing any significant dynamic effects. Testing several time spans, 0.5 s was found to be the optimum.

The following section focuses on comparing the simulations without granules. This will give an impression of the determined material parameters for the steel. Thus, Experiment 1, 3, and 5 are simulated. This is followed by modelling the granules. The potential of this method is of particular interest since the use of the DEM is computationally very expensive. Thus, being able to perform most of the simulation with the FEM is preferable.

6.1.1 Simulations without granules

First, the models without granules are compared with the simulations. As they will be used for comparisons with simulations including granules, the computations are denoted as reference configurations. Since different steel parameters are determined, Experiment 1 and 3 are simulated individually.

Experiment 1

In Figure 6.2, the force-displacement curve of the numerical simulation is compared with the experimental data. Using the parameters for steel from the previous section, a very good agreement is observed regarding the slope of the curves for both the outer and the inner hull. Also, the contact with the inner hull is at the same position, and the force applied after rupture of the outer hull is similar.

The critical aspect is the rupture of the plates. There is a good agreement for the inner hull, with a mismatch of 12 mm for the location, while the maximum force is underestimated by about 5 %. However, a look at the outer hull reveals that the results are not

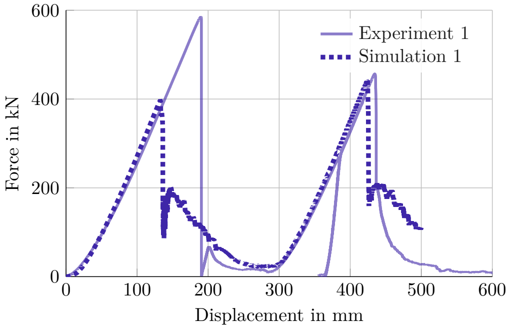

Figure 6.2: Comparison of the force-displacement curve for the first experiment with the simulation.

quite as good. The maximum force is similar to the inner hull, but the rupture occurs much earlier than in the experiment. This supports the conclusion made in Chapter 5, that the behaviour for the very first indentation of the hull is an outlier.

This difference in rupture force and position leads to a shift in the dissipated energy curve, see Figure 6.3. The shape is similar, and both curves in the simulation are very similar until rupture of the outer hull. However, the total amount of energy until rupture of the inner hull is approximately 23 % lower for the simulation. Looking only at the inner hull – measuring the increase in energy after rupture of the outer hull – both are close to each other, with an energy of 42 kNm for the simulation and 33 kNm for the experiment, respectively. This shows that the elasto-plastic deformation of the model is covered quite well, emphasising the aspect of the rupture mechanism.

Taking a closer look at the rupture behaviour, a flap is observed for both hulls. It develops quite fast, but not as sudden as for the outer hull in the experiment. This is shown in Figure 6.4. The calculated strain is in agreement with the measured values and

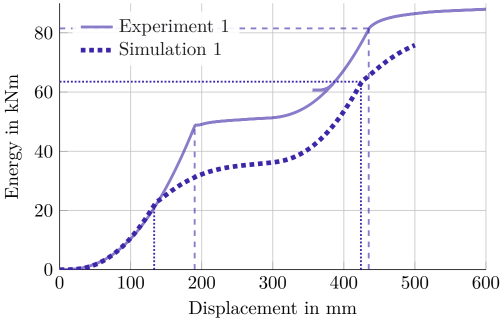

Figure 6.3: Comparison of the dissipated energy during the first experiment. The main difference in the curves is due to the rupture position of the outer hull.

the pattern on the surface, see Figure 5.7. The final shape of the flap can be seen in Figure 6.5. Compared to the experimental result, see Figure 5.6, the hinge is smaller and located on the other side – which is not crucial, since this setup is axisymmetric.

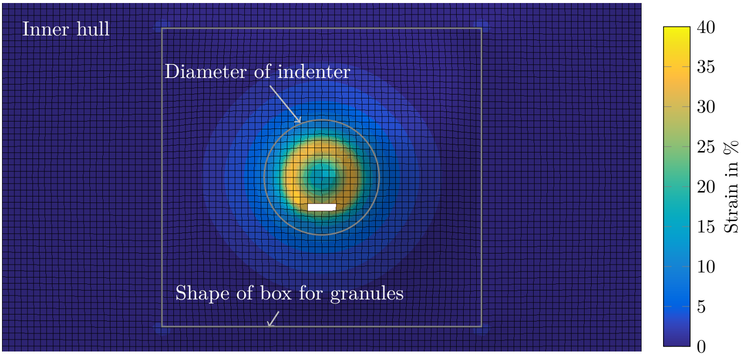

Figure 6.4: Strain distribution of the inner hull in the simulation at the beginning of rupture.

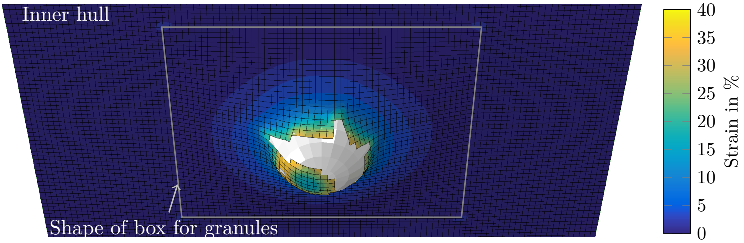

Figure 6.5: Shape of the inner hull after indentation with the bulbous bow and its strain pattern for Experiment 1.

Experiment 3

Compared to Simulation 1, the only changes in the model are the material properties of the steel, especially regarding the rupture behaviour. The force-displacement curve can be seen in Figure 6.6. The overall agreement compared to Simulation/Experiment 1 is much better. The slope and the behaviour after rupture are very similar to the experiment. Looking at the inner hull, the peak force is slightly overestimated and the indentation depth at rupture is slightly higher, but in a good agreement. The outer hull ruptures too early – and therefore with a smaller force – compared to the experiment. The error is approximately 11 % for the peak force and indentation depth. Due to this smaller mismatch – compared to Simulation/Experiment 1 – the dissipated energy is closer to the experimental results, see Figure 6.7. Looking only at the simulation, the higher peak force to penetrate the inner hull could be caused by frictional contact between the indenter and

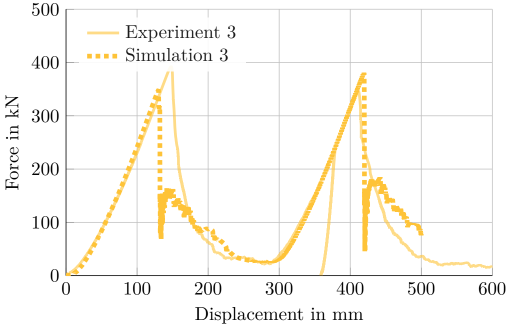

Figure 6.6: Comparison of the force-displacement curve for Experiment 3.

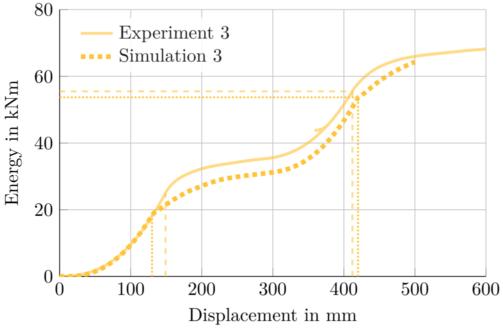

Figure 6.7: Dissipated energy of Simulation 3 compared to Experiment 3.

outer hull. Before the indenter comes into contact with the inner hull at a displacement around 280 mm, the force required to push through the structure is approximately 30 kN. This frictional contact remains while pushing through the inner hull, resulting in the higher total force.

18 kNm are required to push through the outer hull and 54 kNm in total are dissipated during the indentation process until rupture of the inner hull. A more precise prediction of the rupture of the outer hull would improve the prediction of the absorbed energy. Taking into account the other experimental results, it is more likely that the variation in the experiments is the reason for this mismatch. However, since only a limited amount of experimental data is available, it is hard to give a final conclusion.

The development of the rupture is similar to Simulation 1, as can be seen in Figure 6.8 compared to Figure 6.5. Both hulls exhibit a flap that is pushed away. The development starts at the long side of the box, expanding in circular direction. While the hinge is located on the short side of the box in most of the experiments, see Chapter 5, it appears on the long side in this case. The measured strain values coincide with the results from the experiments.

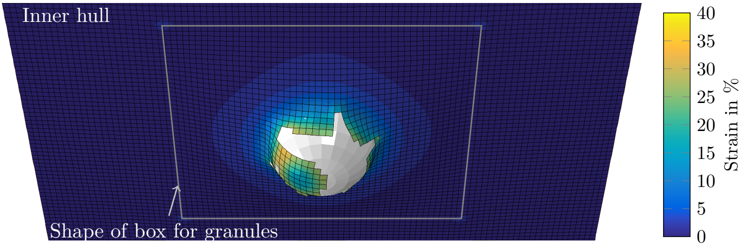

Figure 6.8: Shape of the inner hull after indentation with the bulbous bow and its strain pattern for Experiment 3.

Experiment 5

For the simulation of the experiment with a stiffener, the influence of the mesh size at the stiffener was determined beforehand. In doing so, it could be determined that the same mesh size as for the plates is suitable. This avoids possible mesh dependencies due to the rupture criteria. The force-displacement curve is shown in Figure 6.9. Starting with the outer hull, the increased stiffness is covered very well. The small kink in the curve due to the buckling of the stiffener is close to the location in the experiment. The rupture occurs a bit earlier, and therefore with a lower force. In the simulation, the rupture is not as sudden as in the experiment. Thus, the indenter needs more time and force to push the sheets away. The final rupture pattern of the outer hull can be seen in Figure 6.10. Compared to the experimental results in Figure 5.25, the rupture path is similar.

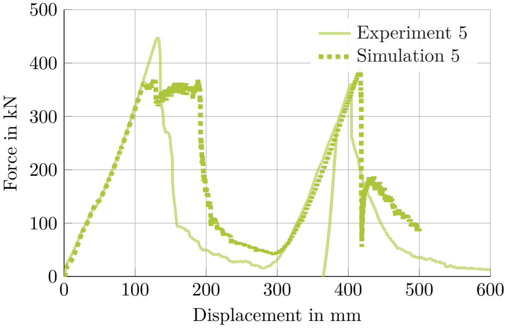

Figure 6.9: Force-displacement curve for the comparison of an empty box with stiffener in Experiment 5.

Due to the longer time needed, the behaviour after rupture is shifted slightly. Thus, the path is similar, but the force in the simulation is higher until the inner hull is reached. After coming into contact with the inner hull, the slope is matched very well. The rupture point and breakage force are overestimated by approximately 11 %. After rupture of the inner hull, the drop in force is more similar to Experiment/Simulation 3. The dissipated

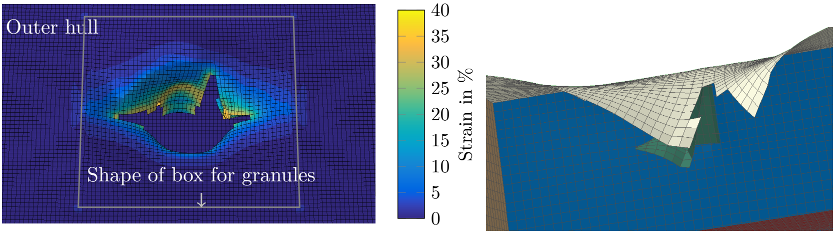

Figure 6.10: Rupture of the outer hull (left) and folding of the stiffener (right) of Simulation 5. Compare to experiment in Figure 5.25.

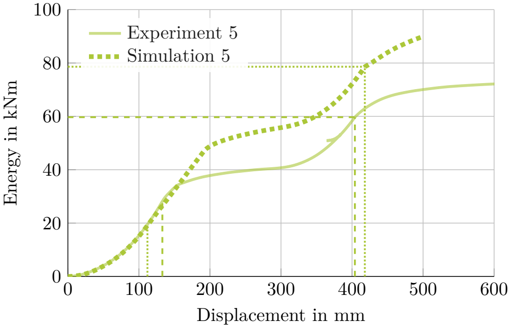

Figure 6.11: Comparison of energy dissipation for Experiment 5 and Simulation 5.

energy is shown in Figure 6.11. Due to the force plateau in the simulation after rupture of the outer hull, the simulation overestimates the energy dissipation by about 18 %.

Conclusion on simulations without granules

The numerical values obtained by the simulation are shown in Table 6.1, as done for the experiments in Table 5.2 and 5.3. Comparing these with the experiments, it can be stated that the total amount of dissipated energy for the simulations without stiffener is underestimated, while the case with a stiffener shows an overestimation. Compared to the

Table 6.1: Rupture positions and dissipated energy for simulations without granules.

	Outer hull			Inner hull				
Sim	u_{ind}	$F_{u,ind}$	$E_{u,ind}$	u_{ind}	u_{gran}	u_{local}	$F_{u,ind}$	$E_{u,ind}$
1	135 mm	400 kN	22 kNm	425 mm	–	145 mm	440 kN	64 kNm
3	130 mm	350 kN	18 kNm	420 mm	–	140 mm	380 kN	54 kNm
5	115 mm	360 kN	19 kNm	420 mm	–	140 mm	390 kN	79 kNm

experiments, the indentation depth at rupture is distributed more uniformly between the simulations and occurs at a local displacement between 130 mm and 145 mm for metal sheets without stiffener. As seen in the experiment, the stiffener increases the overall stiffness, while reducing the indentation depth until rupture. This was also observed in other experiments and simulations [29]. The second batch of steel has a lower maximum force, which was also observed in experiments. The behaviour between the outer and inner hull within a simulation is opposite to that in the experiments. There, the outer hull exhibits a higher maximum force, while in the simulations, it is the inner hull that carries a higher load. This could be caused by the surface of the indenter in the experiment, which is damaged due to the transition through the outer hull. These small scratches are not modelled in the simulation. The difference in peak force for the outer hull and inner hull is between 30 kN and 40 kN in the simulations. This is mainly caused by the frictional contact between the indenter and the flaps of the outer hull after its penetration.

6.1.2 Simulation with granules

Using granules as filling material, a total number of four experiments have to be simulated. The models are the same as in the previous section, with an added block of granules inside the box. For the friction between the steel and the granules, the values from Table 4.4 are chosen. For the material properties, the parameters obtained in Chapter 4 are compared, using two different material models and the initial and fitted parameter sets.

Experiment 2

Figure 6.12 shows the force-displacement curves of the different simulations. First, the results from the Mohr-Coulomb material model are compared. The orange curve shows the simulation using the initial material parameters obtained in Section 4.2, while the blue curve shows the results with the parameters fitted to the uniaxial compression test, see Section 4.4. With both parameter sets, we are not able to simulate the whole indentation process. The complex crushing behaviour of the particles cannot be covered using the

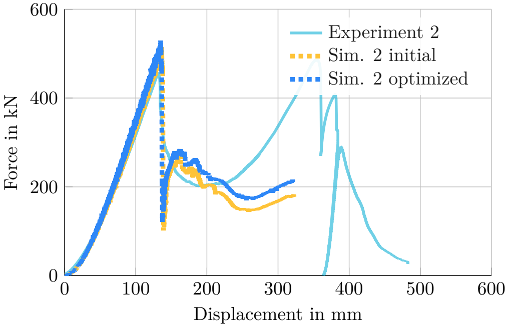

Figure 6.12: Force-displacement curve of Simulation 2 with two different material parameter sets using the Mohr-Coulomb material model for the granules.

Mohr-Coulomb material model with hexahedral finite elements. Thus, the simulation stops due to mesh distortion. However, this happens at a point where the DEM would be applied for the particles using the coupled approach. Therefore, it is possible to account for the advantages and disadvantages using the FEM only.

The initial material parameters for Mohr-Coulomb overestimate the peak and position of the rupture at the outer hull around 13 %. Up to there, the stiffness of the structure is matched very well. After rupture of the outer hull, the drop in force is more rapid than in the experiment, with a lower force during the transition through the granules. Still, a decrease is observed – especially where the force increases again in the experiment, at a displacement of 200 mm. Using the optimized parameter set, the peak force and rupture position are similar. Compared to the experiment and the initial parameter set, only the stiffness is slightly higher. After the sudden rupture, the force level is higher than with the initial parameters. In fact, it is slightly above the experimental data. As for the other simulation, no increase in force is observed.

Figure 6.13 shows the model after rupture of the outer hull: the left-hand side shows the simulation with granules (not displayed here) as well as the indenter – and the right-hand side shows the simulation without granules for comparison. In both pictures, the indenter moved 250 mm into the structure. The left-hand side shows a displacement of the inner hull, because of the transmitted force due to the granules. In the left picture, the sheet under the indenter is fully ruptured in a circular shape. As in the experiment, the initial flap is clamped between the granules and the indenter. Since no defects on the surface of the metal plates are modelled, the crack propagation occurs more evenly, leading to the round shape of the flap, instead of an edge that is attached to the remaining box. Figure 6.14 allows for a closer look, comparing the simulations with and without granules. In the left picture with granules – again not shown – all elements connecting the flap to the sheet exhibit the failure criterion. The failure strain corresponds to the values measured using DIC.

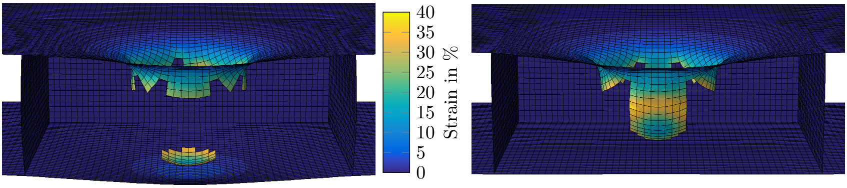

Figure 6.13: Rupture of the filled box (left) and empty box (right) for the indentation of the outer hull. The granules are not depicted in this image. Note the deflection of the inner hull in the left image due to the load transfer of the granules.

Figure 6.15 shows the displacement of the centroid at the inner hull. Until the rupture of the outer hull, the displacement is matched well, with an increasing error while approaching the rupture. The optimized parameter set is closer to the results from the experiment. The reduction in displacement after rupture of the outer hull is not as strong as in the experiment, but it can be observed in simulations. The reason for this can be determined by the modelling using a homogeneous block of granules. Thus, the elements close to the indenter cannot be pushed away. Thus, a tension state can be observed for some elements close to the indenter, which does not physically correspond to the behaviour of

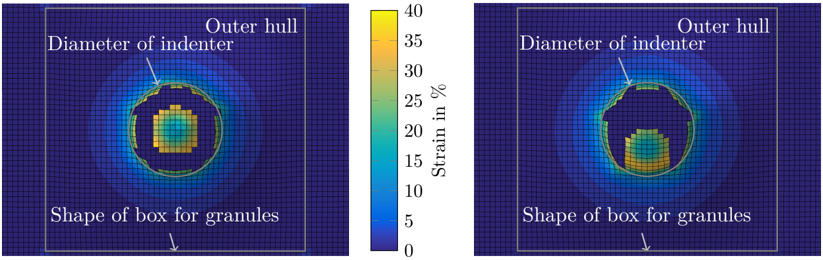

Figure 6.14: Close view on the rupture of the filled box (left) and the empty box (right) for the outer hull in Simulation 1 and Simulation 2.

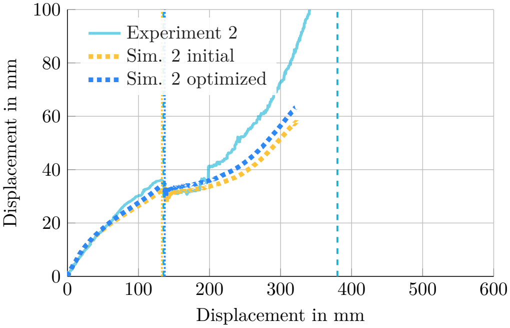

Figure 6.15: Displacement of the centroid at the inner hull during the indentation process for Simulation 2 using the Mohr-Coulomb material model.

the granules. After the drop, again, the optimized parameter set is closer to the experiment, thus representing the transmitting of the force to the inner hull in a better way.

Taking a look at the dissipated energy, the results are very similar to the experiment, since the force-displacement curve is matched very well. The plot can be seen in Figure 6.16. Compared to the reference experiment, Experiment 1, the numerical results are more satisfying. Since the force level after rupture of the outer hull does not drop to zero, the influence due to mismatch in position and maximum force is smaller for the experiment and the simulation with granules.

Hypoplastic material model Using the hypoplastic material model leads to the force-displacement curve shown in Figure 6.17. As before, the initial and the optimized parameter set for the material model is shown. Compared to the Mohr-Coulomb material model in Figure 6.12, this material model has more difficulties to simulate the indentation process after the rupture.

Taking a look at the simulation with the initial parameter set in Figure 6.17, the peak force is matched very well, and the position of the rupture for the outer hull is also in a good agreement. During the loading of the outer hull, the increased stiffness due to the

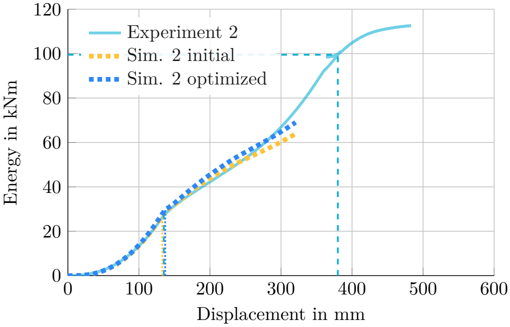

Figure 6.16: Dissipated energy over displacement for the two different parameter sets of granules using the Mohr-Coulomb material model.

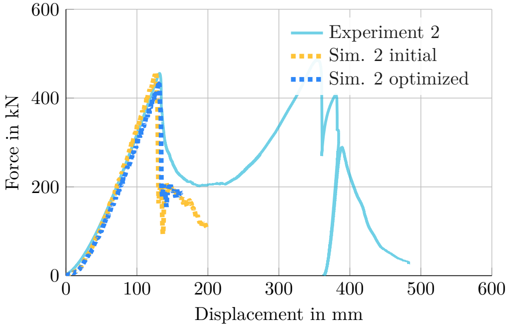

Figure 6.17: Force-displacement curve of Simulation 2 with two different material parameter sets using the hypoplastic material model for the granules.

granules is slightly too high. This is captured using the optimized parameter set more accurately, but with the drawback of a lower peak force.

After rupture of the outer hull, both parameter sets underestimate the resistance force due to the granules. The failure of the simulation shortly after the rupture is caused by distorted elements.

The displacement of the centre of the inner hull during the loading of the outer hull is shown in Figure 6.18. Compared to the Mohr-Coulomb results, the initial parameter set provides a better estimation of the displacement until the outer hull ruptures. After rupture of the outer hull, the elastic spring back is larger than with the Mohr-Coulomb material models. The optimized parameter set transfers less load to the inner hull, resulting in a smaller displacement than in the experiment. This – as already shown in the simulation of the triaxial compression test, Section 4.2 – indicates a behaviour that is too soft. Apparently, the optimization process governing the material parameters using only the uniaxial compression data is not as suitable for this material model as it is for the

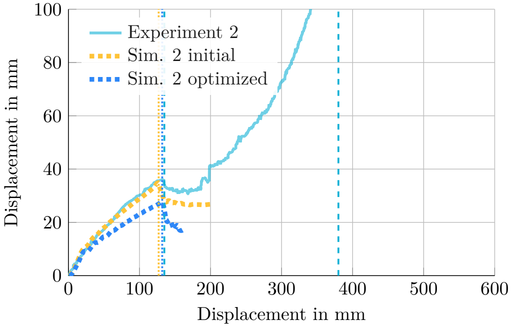

Figure 6.18: Displacement of the centroid at the inner hull during the indentation process for Simulation 2 using the hypoplastic material model.

Mohr-Coulomb model. Maybe the data provided by the uniaxial compression test is not able to identify the parameters correctly, since the hypoplastic material model has more variables. The inferior result of the optimized hypoplastic material parameter set for the triaxial test in Section 4.2.3 supports this explanation.

Experiment 4

The simulation of Experiment 4 is very similar to Experiment 2. Thus, what follows are a brief overview of the numerical results and a discussion of the differences caused by the different material data for the steel. The properties of the granules are the same as for Experiment 2. The force-displacement curve is shown in Figure 6.19. As before, the results for the two different parameter sets of the granules using the Mohr-Coulomb material model are depicted. The rupture of the outer hull occurs at the same position as in the simulation without granules – compare Figure 6.6. Compared to the experimental

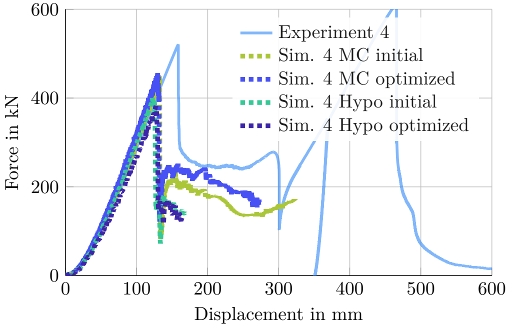

Figure 6.19: Force-displacement curve of Simulation 4 with the two material models and its parameter sets.

results, it ruptures too early. For both Mohr-Coulomb curves, the increase in stiffness while loading the outer hull is covered very well. After rupture, the observed force plateau is estimated more accurately using the optimized parameter set.

As in the simulation for Experiment 2, the displacement of the centre of the inner hull is underestimated, see Figure 6.20. During the first 50 mm, both Mohr-Coulomb parameter sets match the experiment very well. Then, the displacement of the inner hull is lower compared to the experiments. Thus, the granules reach a higher level of compaction in the numerical simulation. The optimized Mohr-Coulomb parameter set is closer to the experimental result. As shown before, the rupture position differs from the experiment. Thus, the position in drop of displacement is not matched. However, a kink at the numerical rupture and the observed drop in displacement is visible, but smaller than in the experiment.

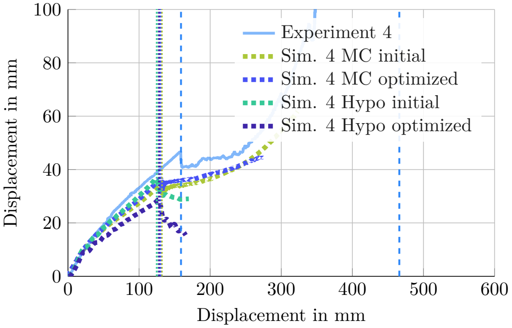

Figure 6.20: Displacement of the centroid at the inner hull during the indentation process for Simulation 4.

Figure 6.21 shows the dissipation in energy. Both Mohr-Coulomb parameter sets match the experimental results during the loading of the outer hull very well, as already seen in

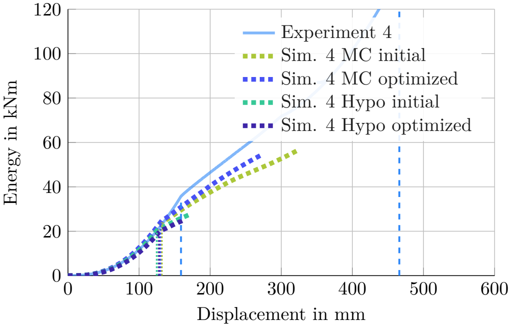

Figure 6.21: Dissipated energy over the displacement for the two different parameter sets of granules in Simulation 4.

Experiment 2. Due to the unmatched indentation depth at rupture, the flattening in the numerical simulations occurs at an earlier position than in the experiment. The slope after rupture is covered better using the optimized parameter set. The initial Mohr-Coulomb parameter lacks of energy dissipation after rupture.

Hypoplastic material model Using the hypoplastic material model, the mismatch regarding the hull rupture increases as compared to the Mohr-Coulomb material model, see Figure 6.19. The initial parameter set shows a slightly better agreement with the experimental results regarding the overall stiffness of the structure, while the optimized parameter set is too soft. After rupture in the model, both simulations with hypoplastic material model have a lower – but similar – force plateau as compared to the Mohr-Coulomb material model. As seen before, the robustness of this material model regarding element distortion is inferior compared to the Mohr-Coulomb model.

The soft behaviour of the optimized parameter set can also be seen from the displacement of the centre of the inner hull in Figure 6.20. While the initial parameter set for the hypoplastic material model performs slightly better than the Mohr-Coulomb material models, the optimized parameter set underestimates the displacement much more.

Considering the dissipated energy, the hypoplastic material models as well as the Mohr-Coulomb material model are a very good choice until the rupture of the outer hull. The main influence on the kink in the curve is related to the rupture behaviour of the steel modelling. After rupture, the lower resistance of the granules using the hypoplastic material model results in an underestimation of the required energy.

Conclusion on simulations with granules without stiffener

Summarizing, and taking into account the results from Experiment 2, the numerical behaviour is similar – regarding the rupture mechanism and pattern as well as the influence of the two material parameter sets for the Mohr-Coulomb material model. Both sets reflect the influence during the indentation of the outer hull very well, and the differences are minor. After rupture, the optimized parameter set performs slightly better, comparing the force needed to push through the granules and the displacement of the inner hull in this situation.

The hypoplastic material model using its initial parameter set results in a slightly better agreement until rupture of the outer hull. Especially the load transferred to the inner hull is matched more accurately. Considering the optimized parameter set, even the Mohr-Coulomb model with its initial material parameters performs in a better way. This could be resolved using additional data for the optimization process, but would make the entire identification process more expensive – especially considering the disadvantages regarding the general computation time, compared to the Mohr-Coulomb model, and its higher sensitivity undergoing mesh distortion.

Overall, the main factor for a good estimation of the dissipated energy is the rupture position of the outer hull. This was already observed in the previous section without granules and could also be observed here. With a matching indentation depth at rupture, the energy dissipation of the optimized Mohr-Coulomb parameter set would be very satisfying for the simulation, including indentation depths, where the use of the DEM is intended. Regarding the hypoplastic material model, more effort would have to be invested in parameter estimation and simulation stability in order to obtain a reasonable advantage over the Mohr-Coulomb material model. In fact, it is not possible to compute the whole indentation process, since the FEM used here cannot cover the distortion of elements in the later state of the experiment. Thus, switching to the DEM is recommended if the indenter comes into contact with elements of granules.

Experiment 6

The experiment with a stiffener was carried out with two different granules. Here, we will investigate the numerical results using *Poraver*. Again, both parameter sets for the Mohr-Coulomb material model are shown for the simulation of the force-displacement curve, see Figure 6.22. It is found that the increase in stiffness of the overall structure during the loading of the outer hull is covered very well by both parameter sets. As in the simulation without granules, the initial rupture position is too early, but the force still increases afterwards. A drop in force is observed at a displacement of approximately 180 mm for the optimized parameter set, while the simulation with the initial parameter set is not able to compute up to this point. The displacement at the drop in force is similar to the numerical results without granules, seen Figure 6.9.

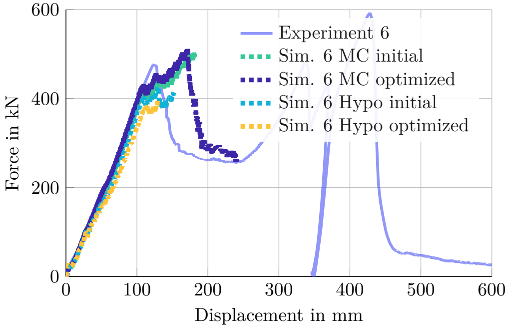

Figure 6.22: Force-displacement curve of Simulation 6 with two different material models and two parameter sets each.

The rupture pattern for the outer hull is similar to the results without granules, see Figure 6.23. The left image shows the final deformation of the outer hull at the end of the calculation with the optimized parameter set. The cut develops parallel to the stiffener, eventually leading to branches perpendicular to the stiffener, after the stiffener ruptures. Compared to the simulation without granules – see Figure 6.10 – the buckling of the stiffener is hindered, as can be seen in the right image of Figure 6.23. Thus, the intended influence due to the granules on the stiffener can be observed.

The dissipation in energy during the simulation matches the experiment until rupture of the outer hull, see Figure 6.24. Both Mohr-Coulomb material parameter sets are very similar. After rupture, the plateau in force results in an overestimation, compared to the experiment, for both. Comparing the displacement of the centre of the inner hull, the displacement is underestimated, starting with the rupture of the stiffener. This can be seen in Figure 6.25.

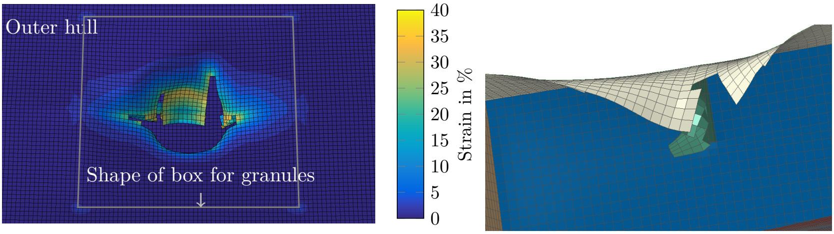

Figure 6.23: Rupture of the outer hull (left) and the stiffener (right) in Simulation 6. Compare to experimental results in Figure 5.27 and Figure 5.28.

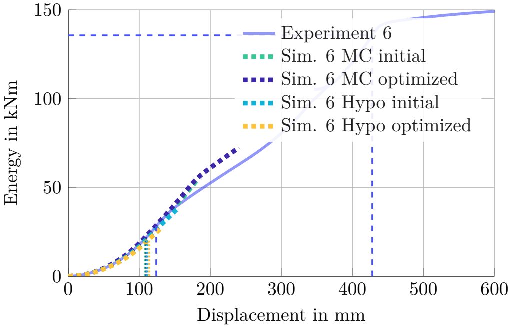

Figure 6.24: Energy dissipation during the indentation process of Simulation 6.

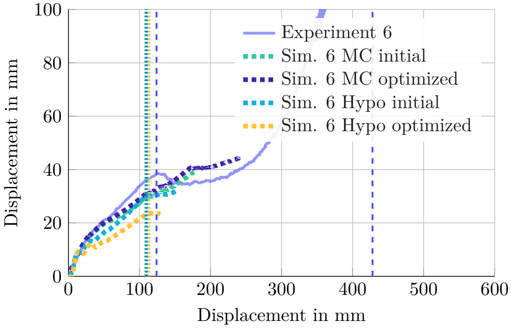

Figure 6.25: Displacement of the centroid at the inner hull during the indentation process for Simulation 6.

Hypoplastic material model Taking a look at the hypoplastic material model, the initial parameter set performs, as seen before, better than the optimized parameter set. Compared to the Mohr-Coulomb material model, it estimates the stiffness of the structure slightly better, see Figure 6.22. The rupture of the outer hull occurs at the same position as for the other material model, and an increase in force after rupture can be observed as well. The simulation using this material model fails shortly after the rupture of the outer hull.

Considering the dissipated energy, the initial parameter set is closer to the experiment, see Figure 6.24. However, all simulations are very close to the experiment until rupture of the outer hull. The displacement of the centre at the inner hull – see Figure 6.25 – is matched better by the initial parameter set. Nonetheless, the displacement is underestimated for both, and the Mohr-Coulomb material parameter sets seem to perform better.

Experiment 7

In order to investigate the influence of the chosen method on the modelling of the granules, the second type granule is simulated in the following. The material parameters for *Danamol* are given in Table 4.1 and Table 4.2, based on experiments, and in Table 4.7 and Table 4.8 based on the numerical optimization for the uniaxial compression test.

Figure 6.26 shows the corresponding force-displacement curves. Starting with the Mohr-Coulomb material model, a good match of the structure's stiffness is observed for both simulations. Both parameter sets yield similar results until the rupture of the outer hull.

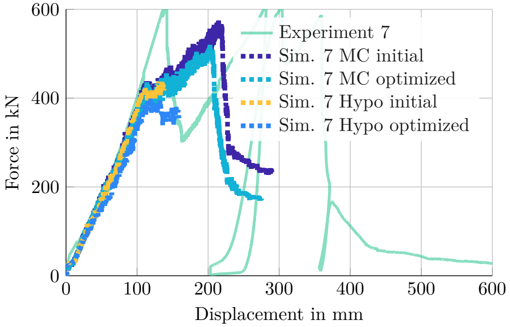

Figure 6.26: Force-displacement curve of Simulation 7 with two different material models and its parameter sets for the granules.

The position and force of this event is underestimated, and an increase in force is observed in the simulation after this event – due to the interaction with the remaining flap until it finally ruptures. Compared to the experiment, the drop in force after the initial rupture is not present, and the increase in force starts directly after the initial rupture. The finial rupture of the flap occurs earlier than in the experiment and with a higher drop in force. The rupture mechanism is similar to the rupture behaviour observed in the simulation in the previous section – see Figure 6.23. The folding of the stiffener is more pronounced than for *Poraver*, which is in contrast to the experimental results, but can be explained by the obtained material parameters used for the simulation. The Young's moduli for the initial parameter set and for the optimized parameter set are smaller than for *Poraver*, see Chapter 4.

Taking a look at the dissipated energy – shown in Figure 6.27 – the estimation is reasonable. The influence of the different rupture positions compared to the experiment is

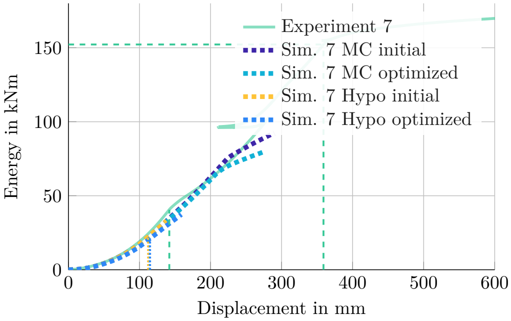

Figure 6.27: Energy dissipation during the indentation process of Simulation 7.

reflected due to a slight mismatch for higher indentation depths. Nonetheless, it is a good estimation for comparison with the simulations without granules.

Figure 6.28 shows the displacement of the centre of the inner hull. Both Mohr-Coulomb material sets cover the displacement up to 50 mm displacement very well. After this point, the displacement is slightly underestimated. At the point of the rupture of the flap, at approximately 200 mm, a spring back is observed. In the experiment, however, this was observed at the initiation of the rupture. Altogether, the initial parameter set for Mohr-Coulomb performs better than the optimized set.

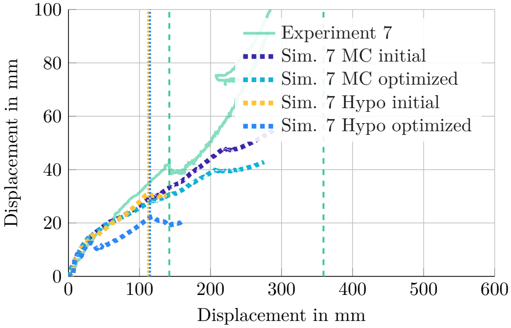

Figure 6.28: Displacement of the centroid at the inner hull in Simulation 7.

Hypoplastic material model The use of a different material model leads to the force-displacement behaviour shown in Figure 6.26. Compared to the Mohr-Coulomb material model, both parameter sets cover a smaller indentation depth. The stiffness of the initial parameter set matches well with the experiment, while the optimized parameter set is too soft. The rupture occurs at the same position as in the other material model, before the rupture in the experiment and at a lower indentation force. The force does not drop after rupture, but remains almost constant.

The softer behaviour of the optimized parameter set can also be found in the energy dissipation plot, see Figure 6.27. The initial parameter set matches the experiment very well, while the optimized parameters underestimate the dissipated energy. Even more clearly, the soft behaviour of the optimized parameter set is visible at the displacement of the inner hull in Figure 6.28. The initial parameter set covers the experimental results very well, even slightly better than simulations with the Mohr-Coulomb material model, while the optimized parameter set underestimates the deflection significantly.

Conclusion on simulations with granules and a stiffener

A comparison of the simulations in Experiment 6 and 7 shows a good agreement regarding the estimation of the stiffness of the double hull structure. Looking at the two different material models, the Mohr-Coulomb is preferred with regard to numerical stability and computational time. For both granules – *Poraver* and *Danamol* – the force-displacement curves are very similar for the initial and the optimized parameter set. Differences are visible in the displacement of the inner hull, where the initial parameter set performs slightly better. For both granules, the displacement is underestimated with a branch point that is similar to the experiment.

Using the hypoplastic material model, it is not possible to calculate much further than the rupture of the outer hull, due to element distortion. Here, the initial parameter set outperforms the parameters derived by applying an optimization to the uniaxial compression test. This can be seen in particular at the displacement of the inner hull. The optimized parameter set underestimates the experiment significantly, resulting in a substantial difference.

At the end, the estimation of the dissipated energy is of major interest. Therefore, the parameter sets with a better performance, as mentioned in the paragraph before, are preferable. As remarked in the experiments without a stiffener, the rupture is the most critical factor. Identifying the rupture parameters for each simulation and each hull segment separately would result in a better agreement, but would make a comparison between simulations impractical. Based on this approach, however, it can be stated that the observed energy dissipation would be covered very well, eliminating the most critical factor. Especially the Mohr-Coulomb model would lead to very promising results. After rupture of the outer hull, it is recommended to switch to the DEM, in order to account for particle crushing.

6.2 Realistic side hull structure

With the information about the modelling of granules obtained in the previous sections, it is possible to examine the side hull structure of a ship. In order to do so, a part of a chemical product tanker is modelled. This design was already subjected to an multi-objective optimization regarding its design variables – such as plate thickness and number of stiffeners – to identify the competitive optimum [162, 163]. Here, the focus lies on one structural design, and the collision behaviour with two different granules and their two parameter sets is investigated. The Mohr-Coulomb material is used for this, since it is of advantage in terms of efficiency, stability, and results as discussed in the chapter before. Furthermore, a potential design change using granules is discussed.

Figure 6.29 left shows the cross-section of the midship section. The numbers represent the plate thickness and the attached profile. The right side of Figure 6.29 shows the finite element model, where the different sections are represented with different colours.

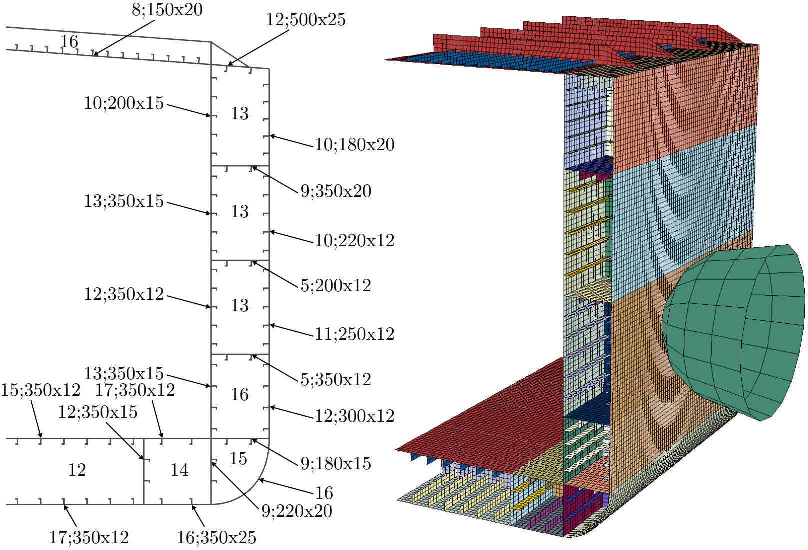

Figure 6.29: Panel definition of the midship (left, adapted from [162]) and finite element model with bulbous bow (right).

As in the simulation for the simplified side hull structure, an explicit time integration is chosen, using the same finite element solver Abaqus. The entire structure is modelled using four-noded shell elements with reduced integration, five integration points through the thickness, and a Reissner-Mindlin formulation. This includes the stiffeners. A rigid body is assumed for the indenter, and the contact interactions are the same as applied before, using the friction coefficients obtained in Chapter 4.3. The modelling of the granules with continuum elements requires more effort in the model creation. The presence of multiple stiffeners is accounted for with cutouts in the granular blocks in each section of the side hull structure, resulting in various contact surfaces.

6.2.1 Comparison of materials

In a first step, the potential is evaluated using granules with the hull design shown in Figure 6.29. The outer and inner hull have a distance of 2 m, and the cavity between the hull is filled with granules. Figure 6.30 shows the resulting force-displacement curves for *Poraver*. In addition, the simulation of the empty configuration is depicted.

The vertical lines indicate the rupture of the outer hull and inner hull, respectively. An improvement in terms of penetration resistance is clearly visible, considering only the rupture of the outer hull. The empty side hull structure ruptures after 1.36 m of indentation, while the filled structure remains intact until a penetration of 2.48 m for the

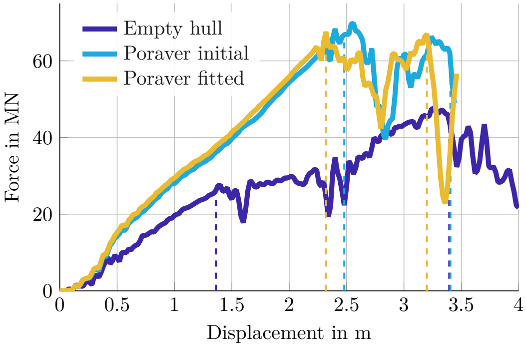

Figure 6.30: Force-displacement curve for the double hull structure filled with granules using *Poraver* with the Mohr-Coulomb material model.

initial material set and 2.32 m for the fitted material set of *Poraver*. In the further process of indentation, the inner hull ruptures after 3.4 m in the absence of granules, whereas the filled structure ruptures at 3.4 m and 3.2 m, respectively. Thus, the presence of granules does not lead to a significantly lower penetration resistance regarding the penetration depth. Both material parameter sets for the granules show a similar behaviour.

Considering the resistance force, almost double the force is observed up to the rupture of the outer hull at around 2.4 m – which, as will be shown later on, results in an improvement in energy dissipation. After the rupture of the outer hull, the resistance force maintains its level of approximately 60 MN until the rupture of the inner hull, which is higher than in the case without granules.

An interesting fact is the very late rupture of the outer hull for the case with granules, calling for a closer look at the details. The structure can withstand a 75% higher indentation depth compared to the empty hull. Comparing the displacements of the two configurations – see Figure 6.31 – the reason for this behaviour can be identified.

The Figure shows different loading states for the hull with and without granules. For small indentations up to 1 m, the structural behaviour is similar, also visible in the close force-displacement curves shown before. The following behaviour is observed for higher indentation depths: the entire structure undergoes a higher deformation if there are granules present. Comparing e.g. the displacement plots at an indentation depth of 3 m, the structure with a filling shows higher bending of the upper section and a higher deformation angle from the side section to the ground section. This global deformation results in smaller local deformations for the outer hull, compared to the empty structure. Thus, the rupture of the outer hull occurs at a later stage in the simulation. The last image shows that, for both cases, the inner hull is ruptured at 3.44 m indentation depth.

The resulting energy dissipation is shown in Figure 6.33. There, vertical and horizontal lines indicate the rupture of the outer and inner hull for the simulation with *Poraver* with the initial parameter set and, for comparison, the empty structure. The improvements due to the granules are significant. Considering the rupture of the outer hull, an increase in dissipated energy of a factor of nearly 5 is observed, due to the higher resistance force and the late rupture. The outer hull of the empty structure ruptures after an energy input of

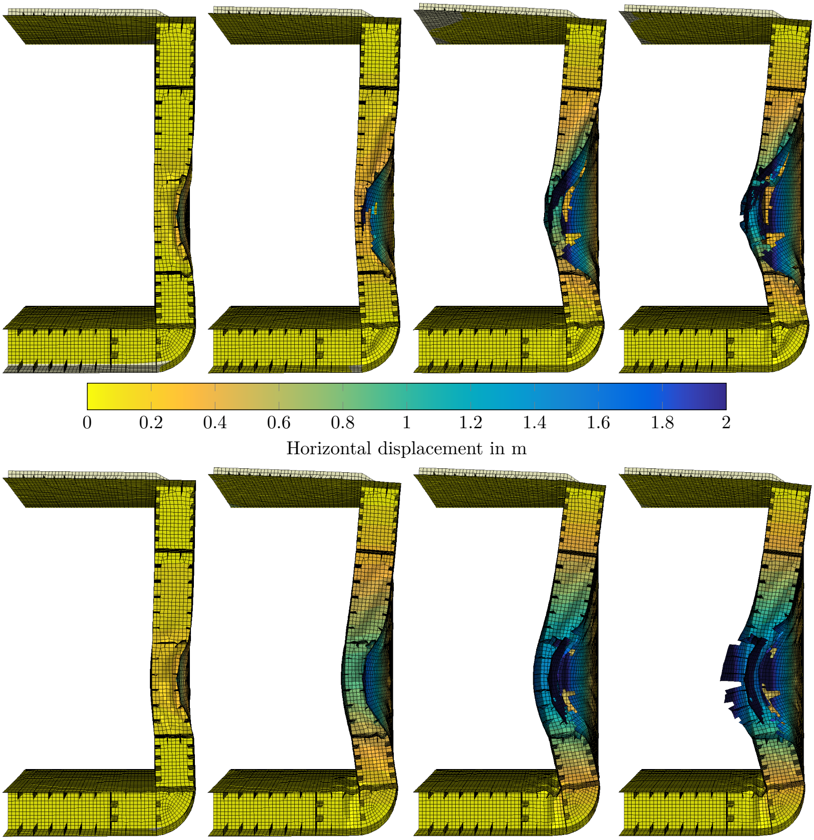

Figure 6.31: Displacement of the double hull structure: simulation without granules in the top row and simulation with granules in the bottom row using the initial material parameters for *Poraver*. Four different indentation depths are shown. From left to right: $1\,\mathrm{m}$, $2\,\mathrm{m}$, $3\,\mathrm{m}$, and $3.44\,\mathrm{m}$, which is the last step before failure of the model with granules.

$17\,\mathrm{MNm}$, while the filled variant can withstand $82\,\mathrm{MNm}$. Compared to the reference configuration, this is approximately the energy needed to indent the entire side hull structure – the outer and inner hull. The inner hull of the empty structure ruptures at an energy input of $85\,\mathrm{MNm}$, and the filled setup exceeds this with $137\,\mathrm{MNm}$. This is an improvement of 61%, which coincides with the results obtained for the simplified double hull structure.

For the second granular material, the force-displacement curves shown in Figure 6.32 are obtained. As already seen in Section 6.1.2, the force-displacement curves are similar to the results using *Poraver*. This is consistent with the very similar material parameter obtained for small compression ratios. The influence of the optimization for the material parameter is small regarding the loading path and energy dissipation, see Figure 6.33. Compared to

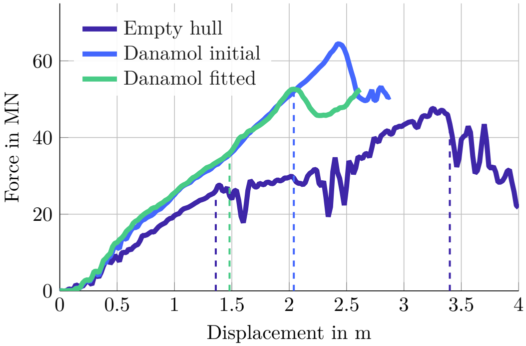

Figure 6.32: Force-displacement curve for the double hull structure filled with granules using *Danamol* with the Mohr-Coulomb material model.

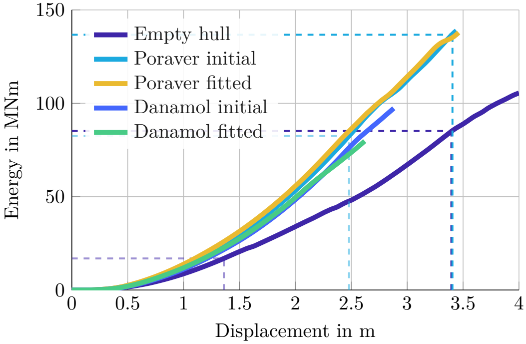

Figure 6.33: Energy dissipation for the double hull with different material models and its parameter sets using the Mohr-Coulomb material model.

Poraver, the material parameters are more sensitive for the continuum elements, so the model is not able to calculate the whole indentation process.

Concluding, the presented simulations show an advantage regarding the filling of the cavity between the double hull structure. Especially the load transfer to the inner hull and load distribution contributes considerably to collision safety. Due to the support of the outer hull, the local indentation is mitigated and the rupture of the outer hull is delayed.

6.2.2 Changes in hull design

As the last aspect, the potential of changing the double hull width of a ship will be investigated. The increase in energy dissipation shown before can be used to reduce the span between the outer and inner hull, aiming for the same energy dissipation compared to a void structure. In the following, the width will be reduced up to 30%, which is the limit so as not having to alter the inner structure and to leave enough space for the granules. In doing so, hull widths of 1.4 m, 1.6 m, and 1.8 m are simulated in addition to the original model.

Figure 6.34 shows the force-displacement curves for these variations, as well as the structure without granules. All four hull widths lead to the same increase in stiffness for the side hull section. Small differences can be found for the rupture of the outer hull, which occurs earlier for the smaller hull widths, but the results are close. After rupture of the outer hull, the curves are more distinguishable. The narrower hull widths carry more load, since there is less soft granular material in between, until the engagement of the inner hull. However, this results in the drawback of an earlier rupture of the inner hull for smaller hull widths. Thus, the penetration depth is reduced from 3.4 m, for a width of 2 m, to 3 m for a width of 1.4 m. The reduction in hull width does not correlate directly with the reduction in penetration depth. The reason for this can be found in the overall behaviour of the structure, which can be seen in Figure 6.35. Compared to the displacement for the width of 2 m, see Figure 6.31, the structure undergoes a stronger deformation before rupture of the inner hull.

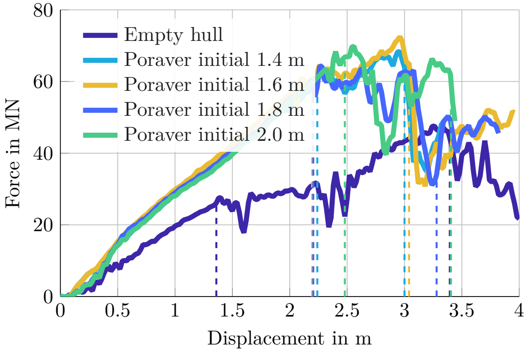

Figure 6.34: Force-displacement curves for different hull widths using the Mohr-Coulomb material model.

In terms of energy dissipation, the differentiation in the designs is due to the time of rupture for the inner hull, see Figure 6.36. As worked out before, the 2 m hull dissipates 137 MNm until rupture. For smaller widths, this is gradually reduced to 116 MNm for 1.4 m hull width. Thus, the advantage compared to the empty structure is still retained with an increase of 34% in energy dissipation.

This shows the potential of using granules as a reinforcement material in the design stage of a ship. A reduction in hull width can be considered without decreasing the penetration resistance, leading to more space for goods. In doing so, changes in structural behaviour can be taken into account in the design stage, so as to fulfil all concurrent requirements for ship safety due to the change in geometry.

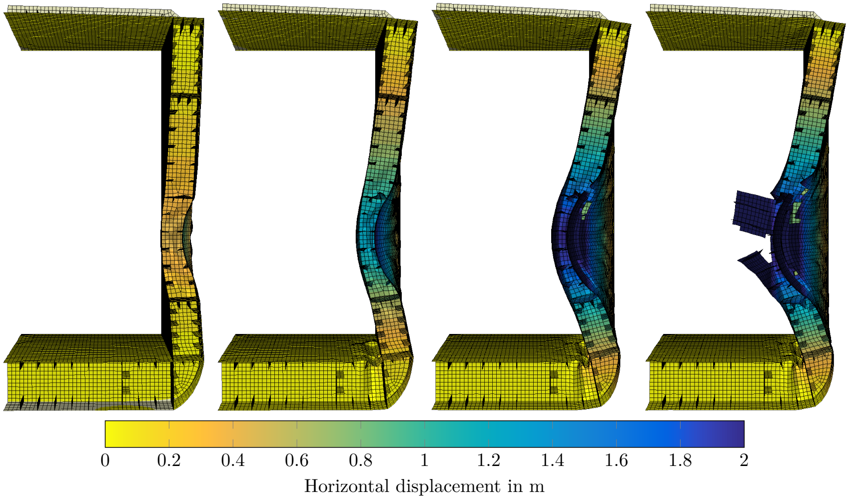

Figure 6.35: Displacement of the double hull structure with a hull width of $1.4\,\mathrm{m}$ with granules and initial material parameters for *Poraver*. Four different indentation depths are shown. From left to right: $1\,\mathrm{m}$, $2\,\mathrm{m}$, $3\,\mathrm{m}$, and $3.44\,\mathrm{m}$, which is the last step before failure of the model with granules.

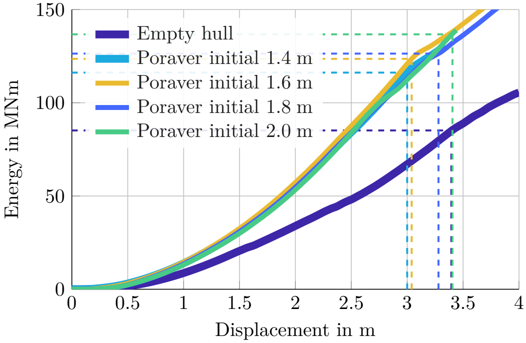

Figure 6.36: Energy dissipation for the double hull with different hull widths using the Mohr-Coulomb material model.

7 Conclusions and Outlook

The focus of this thesis was on studying the opportunities of using granules as a filling material for double hull stuctures. The investigation began with the identification of suitable materials for application in the ship industry. Based on environmental, economical, and mechanical requirements, lightweight natural materials, such as expanded glass, were found to be worth investigating.

In order to describe their mechanical properties, several tests were performed. On the one hand, tests based on single grains were carried out. To do so, a statistical model was derived to cover the distribution of diameter, crushing strength, and Young's modulus using material-dependent parameters. This leads to a combined three-dimensional distribution with a total of nine parameters describing a granular material. Eventually, this leads to a DEM-application, where this model was used to generate grain parameters in a parallel thesis.

On the other hand, the bulk behaviour of the granules was determined. A uniaxial compression test was introduced for this purpose, in order to determine the strength of the granules. This served to identify suitable materials and to optimize and validate the obtained material parameters. In order to obtain the material parameters, triaxial compression tests, oedometer tests, and friction tests were performed. For the latter, an experimental setup was developed. These tests revealed that the grains undergo crushing and fragmentation when subjected to loads beyond a threshold value.

Based on this work and on knowledge obtained about the granules, a collision scenario was designed for experimental testing. A simplified side hull structure was designed in order to confine the granules in a box between the outer and inner hull. A total of seven experiments were performed. A first series of experiments compared a filled and an empty structure with two different boundary conditions. Subsequently, a second series of experiments with an added stiffener to the structure and an additional granular material was carried out. The energy dissipation until rupture of the inner hull was chosen to quantify the improvements due to the filling of the cavity.

The first set of experiments showed an improvement by 22% to 150%. This spread in results is caused by the rupture behaviour of the steel plates. This behaviour is strongly dependent on the rupture initiation, which is driven by defects and abrasion at the indenter surface, as well as on the plates developed during the indentation. Averaging the rupture initiation over the experiments, a realistic estimation of 60% increase in energy dissipation was found to be reasonable using expanded glass granules as filling material.

The second set of experiments considered an additional stiffener on the outer hull through the box with granules. For the expanded glass granules, an increase in energy dissipation of 126% was obtained. The presence of the granules prevented a buckling of the stiffener, resulting in additional penetration resistance. Furthermore, an additional granular material was considered in this experimental set: diatomaceous earth. Judging by the characterizing tests, this material has a higher compression strength, but other disadvantages. This leads to a slightly higher improvement in energy dissipation, but reduces the indentation depth until rupture of the inner hull. This may affect the collision counterpart, and – due to its higher bulk density and chemical properties – expanded glass is better suited for use in ship structures.

To sum up, the granules help to mitigate a collision in three ways. First, a load transfer was observed –from the outer to the inner hull, starting at the beginning of the indentation. Thus, the inner hull absorbs collision energy due to deformation. Secondly, the local indentation of the outer hull is distributed to its surrounding structure. In addition, a change in rupture mechanism is observed. The outer hull is clamped between the indenter and the granules, so that extra energy is needed to detach the flap. And, thirdly, the granules are compressed and crushed close to the indenter, leading to an increased energy dissipation.

For the numerical simulation of the collision scenario, two material models for the granules were considered: the Mohr-Coulomb material model on the one hand, and the hypoplastic material model on the other. Both are used for soil modelling. The obtained material parameters from the bulk test were fitted and optimized to these material models. In addition, a series of tension tests was performed for the steel plates, and the parameters were fitted to the experimental results. This includes failure criteria using a ductile damage model.

For the empty side hull structure, the simulation results were in a good agreement. The characteristics of the simulation results were basically the same as in the experiment, while the differences were due to the different rupture behaviour of the steel plates in the experiment. Comparing the different simulations, the rupture behaviour of the steel plates was very similar. Thus, the simulation results can be compared with each other.

Considering the simulations of experiments with granules, a good agreement was observed for the indentation of the outer hull. The use of continuum models with its limitations regarding crushing of particles is not reliable enough after rupture of the outer hull and the transition of the indenter through the granules. In particular, the computation of the dissipated energy before rupture of the outer hull matches very well – for both material models. After rupture of the outer hull, the results are comparable, but not reliable. The Mohr-Coulomb material model shows advantages over the hypoplastic material model with regard to robustness and speed of the computation and its parameter determination. Thus, despite the fact that the hypoplastic material model shows more realistic results for other experiments, the use of Mohr-Coulomb material model is preferable, as long as no crushing or large deformations occur. At a later state of the indentation process, switching to DEM is recommended, at the latest where the indenter comes into contact with elements of granules.

In the simulation with a stiffener and two different granules, the results from the previous paragraph can be transferred regarding the structural response and material models. The simulation of the second granular material under consideration – diatomaceous earth – resulted in a good agreement with its corresponding experimental results, validating the methods derived using the expanded glass material for parameter identification with the preceding tests.

With the obtained material parameters, it was possible to show a practical application: the midship of a vessel, with its cavity filled with granules. Using expanded glass granules, an increase in energy dissipation of 61% was observed. The idea of using this additional safety margin to reduce the hull width was presented, in connection with calculations based on changed hull widths. It was shown, that, despite the fact that the width was reduced by 30%, an increase in energy dissipation could still be retained compared to an empty, wider hull. This shows the potential of the idea in ship construction.

In order to further investigate the proposed method and to reduce the uncertainties and limitations encountered in this thesis, the following ideas and research topics were developed. The rupture mechanism was found to be a very critical factor in the experiments, and especially defects and abrasion played a major role. Thus, it is recommended to investigate the influence of these phenomena. This goes along with the aspect of repeatability of the experiments. More experiments lead to a statistically representative result, eventually consolidating the estimated improvement in this thesis.

In order to model the entire indentation process, the coupling of particle methods and continuum methods should be developed further, which can then be validated using results obtained in this thesis.

Appendix

A Material parameter identification

A.1 Experimental results for material models

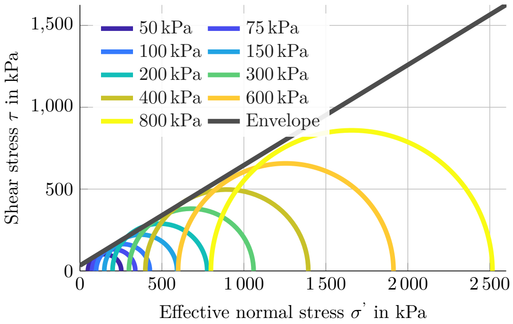

Figure A.1: Mohr's circles for radial pressures from 50 kPa to 800 kPa and the corresponding envelope for *Danamol*.

Figure A.2: Displacement of *Danamol* during the triaxial compression for different radial pressures. From left to right: 100 kPa, 400 kPa, and 800 kPa.

A.2 Numerical results for material models

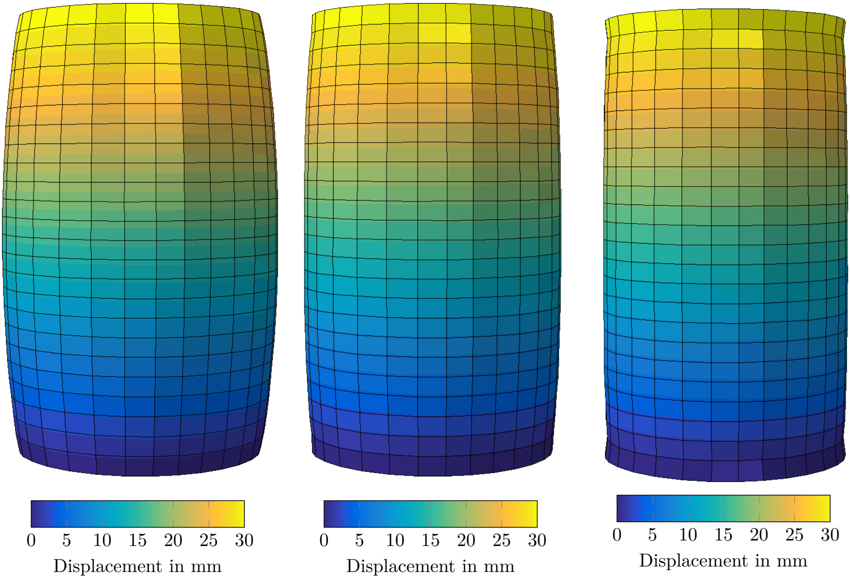

Figure A.3: Displacement of *Danamol* during the simulation of the triaxial compression for different radial pressures and the hypoplastic material model. From left to right: 100 kPa, 400 kPa, and 800 kPa.

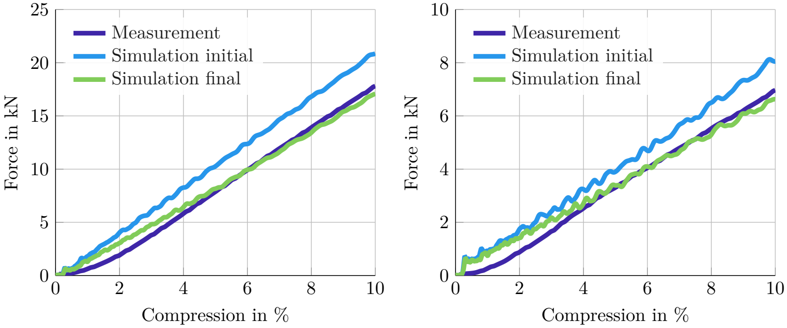

Figure A.4: Force-displacement curves for an optimization up to 10% compression using the Mohr-Coulomb material model for *Danamol*: total force applied (left) and force transmitted through the granules (right).

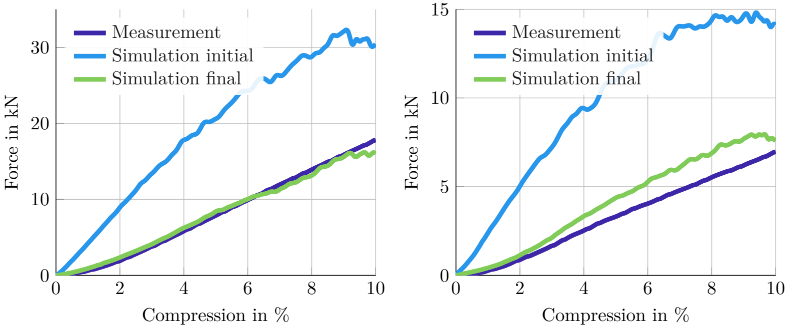

Figure A.5: Force-displacement curves for an optimization up to 10% compression using the hypoplastic material model for *Danamol*: total force applied (left) and force transmitted through the granules (right).

Bibliography

[1] National Transportation Safety Board, Marine Accident Report: Grounding of the U.S. Tankship Exxon Valdez on Bligh Reef, Prince William Sound Near Valdez, Alaska, Article, National Transportation Safety Board (2003) [cited 2020-12-22].
URL `https://www.hsdl.org/?abstract&did=746707`

[2] Ship Structure Committee, PRESTIGE: Complete hull failure in a single-hull tanker, Article, Ship Structure Committee (2003) [cited 2020-12-20].
URL `http://www.shipstructure.org/case_studies/Prestige.pdf`

[3] M. Schöttelndreyer, Füllstoffe in der Konstruktion: Ein Konzept zur Verstärkung von Schiffsseitenhüllen, Ph.D. thesis, Technische Universität Hamburg-Harburg (2015). `doi:10.15480/882.1258`.

[4] IMO, International Maritime Organization (2019) [cited 2019-03-07].
URL `http://www.imo.org/`

[5] P. Wriggers, Nonlinear Finite Element Methods, Springer-Verlag, 2008. `doi:10.1007/978-3-540-71001-1`.

[6] T. Belytschko, W. K. Liu, B. Moran, K. Elkhodary, Nonlinear Finite Elements for Continua and Structures, John Wiley & Sons, 2013, ISBN:978-1-118-70008-2.

[7] K.-J. Bathe, Finite element procedures, 2nd Edition, Prentice-Hall, 2014, ISBN:978-0-9790049-5-7.

[8] P. Wriggers, Computational Contact Mechanics, 2nd Edition, Springer-Verlag, 2006. `doi:10.1007/978-3-540-32609-0`.

[9] International Conference on Designs and Methodologies for Collision and Grounding Protection of Ships, Society of Naval Architects and Marine Engineers (U.S.) (Eds.), Proceedings of the International Conference on Designs and Methodologies for Collision and Grounding Protection of Ships, Society of Naval Architects and Marine Engineers, 1996.

[10] M. Lützen, Technical University of Denmark, Collision and grounding of ships (Eds.), Proceedings of the 2nd International Conference on Collision and Grounding of Ships, Department of Mechanical Engineering, 2001, ISBN:978-87-89502-50-2.

[11] International Conference on Collision and Grounding of Ships, Nihon-Zōsen-Gakkai, ICCGS, International Conference on Collision and Grounding of Ships (Eds.), Proceedings of the 3rd International Conference on Collision and Grounding of Ships, Society, 2004, OCLC:255381345.

[12] Schiffbautechnische Gesellschaft (Ed.), Proceedings of the 4th International Conference on Collision and Grounding of Ships, Schiffbautechnische Gesellschaft, 2007, ISBN:978-3-89220-639-2.

[13] S. Ehlers, J. Romanoff, Aalto-Yliopisto, International Conference on Collision and Grounding of Ships, ICCGS (Eds.), Proceedings of the 5th International Conference on Collision and Grounding of Ships, Aalto Univ., School of Science and Technology, 2010, OCLC:930790713.

[14] J. Amdahl, S. Ehlers, B. J. Leira, Collision and Grounding of Ships and Offshore Structures, CRC Press, 2013, ISBN:978-1-315-88489-9.

[15] C. G. Soares (Ed.), Developments in the Collision and Grounding of Ships and Offshore Structures: Proceedings of the 8th International Conference on Collision and Grounding of Ships and Offshore Structures, CRC Press, 2019, ISBN:978-1-00-076803-9.

[16] G. Wang, K. Arita, D. Liu, Behavior of a double hull in a variety of stranding or collision scenarios, Marine Structures 13 (3) (2000) 147–187. `doi:10.1016/S0951-8339(00)00036-8`.

[17] F. Wu, R. Spong, G. Wang, Using numerical simulation to analyze ship collision, in: International Conference on Collision and Grounding of Ships et al. [11], pp. 217–224, CorpusID:55030378.

[18] T. Nakamura, T. Kuroiwa, Experimental study on failure of ship's side structure, Proceedings of International Conference on Technologies for Marine Environment Preservation (1995) 130–136. ISBN:4930966019.

[19] T. K. Lee, J. D. Kim, T. B. Chun, B. C. Shin, Experimental study on the collision strength of VLCC side structures, in: Proceedings of The Ninth International Offshore and Polar Engineering Conference, International Society of Offshore and Polar Engineers, 1999, p. 113.

[20] J. W. Ringsberg, Characteristics of material, ship side structure response and ship survivability in ship collisions, Ships and Offshore Structures 5 (1) (2010) 51–66. `doi:10.1080/17445300903088707`.

[21] J. K. Paik, J. Y. Chung, I. H. Choe, A. K. Thayamballi, P. T. Pedersen, G. Wang, On rational design of double hull tanker structures against collision, in: Proceedings of The Annual Meeting of The Society of Naval Architects and Marine Engineers, Society of Naval Architects and Marine Engineers, 1999, pp. 1–33.

[22] R. Toernqvist, Design of crashworthy ship strucures, Ph.D. thesis, Technical University of Denmark, ISBN:978-87-89502-74-8 (2003).

[23] A. Gong, J. Liu, B. Xiao, N. Wang, The analysis and comparison of double side skin crashworthiness, in: Proceedings of The 6th International Conference on Collision and Grounding of Ships (ICCGS6), 2013, pp. 315–322, OCLC:852832415.

[24] J. Amdahl, D. Kavlie, Experimental and numerical simulation of double hull stranding, in: DNV-MIT Workshop on: Mechanics of Ship Collision and Grounding, 1992, pp. 1–15.

[25] U. B. Karlsson, J. W. Ringsberg, E. Johnson, M. Hoseini, A. Ulfvarson, Experimental and numerical investigation of bulb impact with a ship side-shell structure, Marine Technology 46 (1) (2009) 1–15.

[26] A. AbuBakar, R. S. Dow, Simulation of ship grounding damage using the finite element method, International Journal of Solids and Structures 50 (5) (2013) 623–636. `doi:10.1016/j.ijsolstr.2012.10.016`.

[27] A. Kulzep, J. Peschmann, E. Lehmann, Life-Cycle Design, Teilvorhaben D2A Seitenkollision von Doppelhüllenschiffen, Report, Abschlussbericht -Vorhaben FKZ-18S0129, Abschlussbericht -Vorhaben FKZ-18S0129 (1999).

[28] R. Toernqvist, B. C. Simonsen, Safety and structural crashworthiness of ship structures; modelling tools and application in design, in: International Conference on Collision and Grounding of Ships et al. [11], pp. 285–294, OCLC:255381345.

[29] H. S. Alsos, J. Amdahl, On the resistance to penetration of stiffened plates, part I – experiments, International Journal of Impact Engineering 36 (6) (2009) 799–807. `doi:10.1016/j.ijimpeng.2008.10.005`.

[30] A. Klanac, S. Ehlers, J. Jelovica, Optimization of crashworthy marine structures, Marine Structures 22 (4) (2009) 670–690. `doi:10.1016/j.marstruc.2009.06.002`.

[31] J. Ringsberg, P. Hogström, A methodology for comparison and assessment of three crashworthy side-shell structures: the X-core, Y-core and corrugation panel structures, in: Proceedings of The 6th International Conference on Collision and Grounding of Ships (ICCGS6), 2013, pp. 323–330. `doi:10.1201/b14915-39`.

[32] G. Wang, C. Ji, P. Kujala, S. Gab Lee, A. Marino, J. Sirkar, K. Suzuki, P. Terndrup Pedersen, W. Vredeveldt, V. Yuriy, Collision and grounding, in: Proceedings of the 16th International Ship and Offshore Structures Congress, University of Southampton, 2006, pp. 201–218, ISBN:978-0-85432-855-0.

[33] S. Ehlers, K. Tabri, J. Romanoff, P. Varsta, Numerical and experimental investigation on the collision resistance of the X-core structure, Ships and Offshore Structures 7 (1) (2012) 21–29. `doi:10.1080/17445302.2010.532603`.

[34] B. Werner, C. Daske, H. Heyer, M. Sander, M. Schöttelndreyer, W. Fricke, The influence of weld joints on the failure mechanism of scaled double hull structures under collision load in finite element simulations, Procedia Materials Science 3 (2014) 307–312. `doi:10.1016/j.mspro.2014.06.053`.

[35] H. Endo, Y. Yamada, O. Kitamura, K. Suzuki, Model test on the collapse strength of the buffer bow structures, Marine Structures 15 (4) (2002) 365–381. `doi:10.1016/S0951-8339(02)00008-4`.

[36] Y. Yamada, Bulbous buffer bows: a measure to reduce oil spill in tanker collisions, Ph.D. thesis, Technical University of Denmark, ISBN:978-87-89502-33-5 (2007).

[37] Y.-f. Huang, K.-A. Wu, H.-C. Chien, C. Chou, K. Tseng, C. H. Hung, C.-c. Chang, Effect of crushable bow on the overall crashworthiness in ship collision, in: Proceedings of the 3rd International Conference on Marine Structures, Taylor & Francis Group, 2011, pp. 365–372. `doi:10.1201/B10771-45`.

[38] M. Schöttelndreyer, I. Tautz, J. Kubiczek, W. Fricke, E. Lehmann, Influence of bulbous bow structures on their collision behaviour, in: Proceedings of the 3rd International Conference on Marine Structures, Taylor & Francis Group, 2011, pp. 381–390. `doi:10.1201/B10771-45`.

[39] I. Martens, Konstruktive Aspekte beim Entwurf von Bugwülsten zur Verbesserung des Energieaufnahmevermögens bei Schiffskollisionen, Ph.D. thesis, Technische Universität Hamburg-Harburg (2014). `doi:10.15480/882.1192`.

[40] W. Fricke, M. Schöttelndreyer, I. Tautz, Verifizierung eines alternativen Aussteifungssystems durch Großversuche: Abschlussbericht BMWI-Vorhaben SideColl, Report, Technische Universität Hamburg-Harburg, ISBN:978-3-89220-675-0 (2014).

[41] W. Fricke, S. Krüger, H. Dankowski, H. Werner, ELKOS Verbundvorhaben: Verbesserung der Kollisionssicherheit durch Integration struktureller Maßnahmen in die Leckstabilitätsberechnung moderner RoRo-Fahrgastschiffe, in: Tagungsband der Statustagung Maritime Technologien, 2013, pp. 37–56.

[42] H. Nagasawa, K. Arita, M. Tani, S. Oka, A study on the collapse of ship structure in collision with bridge piers, Journal of the Society of Naval Architects of Japan 1977 (142) (1977) 323–332. `doi:10.2534/jjasnaoe1968.1977.142_323`.

[43] A. Kulzep, Verhalten von ausgeschäumten Schiffsstrukturen bei Kollision und Grundberührung, Ph.D. thesis, Technische Universität Hamburg-Harburg, ISBN:978-3-89220-609-5 (2001).

[44] M. Schöttelndreyer, I. Martens, W. Fricke, Validierung von kollisionsberechnungen durch großversuche an konstruktionsvarianten von seitenhüllen: Abschlussbericht BMWI-vorhaben ELKOS, Report 676, Technische Universität Hamburg-Harburg, ISBN:978-3-89220-676-7 (2014).

[45] C. E. D. Ouwerkerk, A micro-mechanical connection between the single-particle strength and the bulk strength of random packings of spherical particles, Powder Technology 65 (1) (1991) 125–138. `doi:10.1016/0032-5910(91)80175-I`.

[46] P. Müller, M. Seeger, J. Tomas, Druck- und Bruchverhalten von γ-Al2O3-Granulaten, Chemie Ingenieur Technik 86 (8) (2014) 1284–1293. `doi:10.1002/cite.201300021`.

[47] C. Lillie, P. Wriggers, Dreidimensionales Diskrete Elemente Modell für Superellipsoide, Ph.D. thesis, Universität Hannover, ISBN:978-3-935732-25-3 (2007).

[48] M. Dosta, S. Antonyuk, S. Heinrich, Multiscale simulation of agglomerate breakage in fluidized beds, Ind. Eng. Chem. Res. 52 (33) (2013) 11275–11281. `doi:10.1021/ie400244x`.

[49] X. Lin, T.-T. Ng, A three-dimensional discrete element model using arrays of ellipsoids, Géotechnique 47 (2) (1997) 319–329. `doi:10.1680/geot.1997.47.2.319`.

[50] T. Pöschel, T. Schwager, Computational Granular Dynamics: Models and Algorithms, Springer-Verlag, 2005. `doi:10.1007/3-540-27720-X`.

[51] C. Wellmann, C. Lillie, P. Wriggers, Homogenization of granular material modeled by a three-dimensional discrete element method, Computers and Geotechnics 35 (3) (2008) 394–405. `doi:10.1016/j.compgeo.2007.06.010`.

[52] C. Subero-Couroyer, M. Ghadiri, N. Brunard, F. Kolenda, Weibull analysis of quasi-static crushing strength of catalyst particles, Chemical Engineering Research and Design 81 (8) (2003) 953–962. `doi:10.1205/026387603322482194`.

[53] Y. Rozenblat, D. Portnikov, A. Levy, H. Kalman, S. Aman, J. Tomas, Strength distribution of particles under compression, Powder Technology 208 (1) (2011) 215–224. `doi:10.1016/j.powtec.2010.12.023`.

[54] H. K. D. Portnikov, Determination of elastic properties of particles using single particle compression test, Powder Technology 268 (1) (2014) 244–252. `doi:10.1016/j.powtec.2014.08.011`.

[55] D. Peric, D. R. J. Owen, E. A. d. S. Neto, Computational methods for plasticity: theory and applications, Wiley, 2013, OCLC: 865005169.

[56] P. A. Vermeer, Non-associated plasticity for soils, concrete and rock, in: H. J. Herrmann, J.-P. Hovi, S. Luding (Eds.), Physics of Dry Granular Media, NATO ASI Series, Springer Netherlands, 1998, pp. 163–196. `doi:10.1007/978-94-017-2653-5_10`.

[57] P. Menetrey, K. J. Willam, Triaxial failure criterion for concrete and its generalization, Structural Journal 92 (3) (1995) 311–318. `doi:10.14359/1132`.

[58] C. Wellmann, P. Wriggers, A two-scale model of granular materials, Computer Methods in Applied Mechanics and Engineering 205–208 (2012) 46–58. `doi:10.1016/j.cma.2010.12.023`.

[59] K. Terzaghi, Theoretical Soil Mechanics, John Wiley & Sons, Ltd, 1943. `doi:10.1002/9780470172766`.

[60] R. Brown, J. Richards, Principles of Powder Mechanics, Elsevier, 1970. `doi:10.1016/C2013-0-01576-9`.

[61] D. Kolymbas, Geotechnik: Bodenmechanik, Grundbau und Tunnelbau, 2nd Edition, Springer, 2007, ISBN:978-3-540-68965-2.

[62] T. Knabe, M. Zimmerer, T. Most, T. Schanz, Identification of constitutive parameters for geomaterials modeling using an optimization strategy, in: Proceedings of the 2nd International Conference on Computational Methods in Tunelling, 2009, pp. 1–10, OCLC: 698260586.

[63] C. Truesdell, Hypo-elastic shear, Journal of Applied Physics 27 (5) (1956) 441–447. `doi:10.1063/1.1722399`.

[64] D. Kolymbas, An outline of hypoplasticity, Archive of Applied Mechanics 61 (3) (1991) 143–151. `doi:10.1007/BF00788048`.

[65] G. Gudehus, A comprehensive constitutive equation for granular materials, Soils and Foundations 36 (1) (1996) 1–12. `doi:10.3208/sandf.36.1`.

[66] D. Kolymbas, A rate-dependent constitutive equation for soils, Mechanics Research Communications 4 (6) (1977) 367–372. `doi:10.1016/0093-6413(77)90056-8`.

[67] I. Herle, G. Gudehus, Determination of parameters of a hypoplastic constitutive model from properties of grain assemblies, Mechanics of Cohesive-frictional Materials 4 (5) (1999) 461–486. `doi:10.1002/(SICI)1099-1484(199909)4:5<461::AID-CFM71>3.0.CO;2-P`.

[68] H. Engin, H. Jostad, A. Rohe, On the modelling of grain crushing in hypoplasticity, in: M. Hicks, R. Brinkgreve, A. Rohe (Eds.), Numerical Methods in Geotechnical Engineering, CRC Press, 2014, pp. 33–38. `doi:10.1201/b17017-8`.

[69] N. T. V. Phuong, A. Rohe, R. B. J. Brinkgreve, A. F. van Tol, Hypoplastic model for crushable sand, Soils and Foundations 58 (3) (2018) 615–626. `doi:10.1016/j.sandf.2018.02.022`.

[70] Z. Wang, G. Wang, Q. Ye, A constitutive model for crushable sands involving compression and shear induced particle breakage, Computers and Geotechnics 126 (2020) 103757. `doi:10.1016/j.compgeo.2020.103757`.

[71] A. Moussa, M. Salah, D. Rafik, Improvement of a hypoplastic model for granular materials under high-confining pressures, Geotechnical and Geological Engineering 38 (4) (2020) 3761–3771. `doi:10.1007/s10706-020-01256-y`.

[72] Dassault Systèmes, Abaqus Unified FEA - SIMULIA, Website, Dassault Systèmes (2019) [cited 2019-08-08].
URL `https://www.3ds.com/products-services/simulia/products/abaqus/`

[73] Dassault Systèmes, Abaqus Theory Guide (SIMULIA User Assistance 2019), Dassault Systèmes (2019) [cited 2019-08-08].
URL `https://help.3ds.com/2019/English/DSSIMULIA_Established/SIMACAETHERefMap/simathe-c-ov.htm`

[74] C. Wellmann, A two-scale model of granular materials using a coupled DE-FE approach, Ph.D. thesis, Universität Hannover (2011). `doi:10.15488/7779`.

[75] M.-h. Yu, Advances in strength theories for materials under complex stress state in the 20th century, Applied Mechanics Reviews 55 (3) (2002) 169–218. `doi:10.1115/1.1472455`.

[76] P.-A. von Wolffersdorff, A hypoplastic relation for granular materials with a predefined limit state surface, Mechanics of Cohesive-frictional Materials 1 (3) (1996) 251–271. `doi:10.1002/(SICI)1099-1484(199607)1:3<251::AID-CFM13>3.0.CO;2-3`.

[77] A. Niemunis, I. Herle, Hypoplastic model for cohesionless soils with elastic strain range, Mechanics of Cohesive-frictional Materials 2 (4) (1997) 279–299. `doi:10.1002/(SICI)1099-1484(199710)2:4<279::AID-CFM29>3.0.CO;2-8`.

[78] M. Kelm, Nummerische Simulation der Verdichtung rolliger Böden mittels Vibrationswalzen, Ph.D. thesis, Technische Universität Hamburg-Harburg, Hamburg, ISBN:978-3-936-31006-1 (2003).

[79] J. C. Simo, T. J. R. Hughes, Objective integration algorithms for rate formulations of elastoplasticity, in: J. C. Simo, T. J. R. Hughes (Eds.), Computational Inelasticity, Interdisciplinary Applied Mathematics, Springer, 1998, pp. 276–299. `doi:10.1007/0-387-22763-6_8`.

[80] P. Wood, Fundamentals of bulk solids flow, Technical Report IEA/ICTIS/TR-31, International Energy Agency Coal Research, London (UK), OSTI ID:7806777 (1986).

[81] R. T. Shield, On coulomb's law of failure in soils, Journal of the Mechanics and Physics of Solids 4 (1) (1955) 10 – 16. `doi:10.1016/0022-5096(55)90043-0`.

[82] V. V. Sokolovskii, Statics of Granular Media, Pergamon, 1965, ISBN:978-0-08-013624-0.

[83] R. M. Nedderman, Statics and Kinematics of Granular Materials, Cambridge University Press, 1992. `doi:10.1017/CBO9780511600043`.

[84] M. K. Hubbert, Mechanical basis for certain familiar geologic structures, GSA Bulletin 62 (4) (1951) 355–372. `doi:10.1130/0016-7606(1951)62[355:MBFCFG]2.0.CO;2`.

[85] A. S. Khan, S. Huang, Continuum Theory of Plasticity, 1st Edition, Wiley-Interscience, 1995, ISBN:978-0-471-31043-3.

[86] O. Reynolds, On the dilatancy of media composed of rigid particles in contact. with experimental illustrations, The London, Edinburgh, and Dublin Philosophical Magazine and Journal of Science 20 (127) (1885) 469–481. `doi:10.1080/14786448508627791`.

[87] M. Massoudi, M. M. Mehrabadi, A continuum model for granular materials: Considering dilatancy and the mohr-coulomb criterion, Acta Mechanica 152 (1) (2001) 121–138. `doi:10.1007/BF01176949`.

[88] Dassault Systèmes, Abaqus/CAE User's Guide (SIMULIA User Assistance 2019), Dassault Systèmes (2019) [cited 2019-08-08].
URL `https://help.3ds.com/2019/English/DSSIMULIA_Established/SIMACAECAERefMap/simacae-c-ov.htm`

[89] W. F. Chen, D. J. Han, Plasticity for Structural Engineers, softcover reprint of the original 1st ed. 1988 Edition, Springer New York, 1988, ISBN:978-1-4612-8380-5.

[90] D. Kolymbas, Introduction to Hypoplasticity: Advances in Geotechnical Engineering and Tunnelling 1, CRC Press, 2000, ISBN:978-1-4822-8378-5.

[91] C. Tamagnini, G. Viggiani, R. Chambon, A review of two different approaches to hypoplasticity, in: D. Kolymbas (Ed.), Constitutive Modelling of Granular Materials, Springer, 2000, pp. 107–145. `doi:10.1007/978-3-642-57018-6_5`.

[92] W. Wu, D. Kolymbas, Hypoplasticity then and now, in: D. Kolymbas (Ed.), Constitutive Modelling of Granular Materials, Springer, 2000, pp. 57–105. `doi:10.1007/978-3-642-57018-6_4`.

[93] D. Kolymbas, Introduction to hypoplasticity, in: Modern Approaches to Plasticity, Elsevier, 1993, pp. 213–224, ISBN:978-0-444-59930-8.

[94] R. Chambon, J. Desrues, W. Hammad, R. Charlier, CLoE, a new rate-type constitutive model for geomaterials theoretical basis and implementation, International Journal for Numerical and Analytical Methods in Geomechanics 18 (4) (1994) 253–278. `doi:10.1002/nag.1610180404`.

[95] M. Goldscheider, Grenzbedingung und Fliessregel von Sand, Mechanics Research Communications 3 (6) (1976) 463–468. `doi:10.1016/0093-6413(76)90037-9`.

[96] D. Kolymbas, Eine konstitutive Theorie für Böden und andere körnige Stoffe, Habilitation, Universität Karlsruhe, Heft 109 (1988).

[97] W. Wu, D. Kolymbas, Numerical testing of the stability criterion for hypoplastic constitutive equations, Mechanics of Materials 9 (3) (1990) 245–253. `doi:10.1016/0167-6636(90)90006-2`.

[98] M. F. Atiyah, I. G. Macdonald, Introduction to commutative algebra, Addison-Wesley series in mathematics, Addison-Wesley, 1969, ISBN:978-0-201-00361-1.

[99] C. C. Wang, On representations for isotropic functions, Archive for Rational Mechanics and Analysis 33 (4) (1969) 268–287. `doi:10.1007/BF00281279`.

[100] W. Wu, Hypoplastizität als mathematisches Modell zum mechanischen Verhalten granularer Stoffe, Ph.D. thesis, Universität Karlsruhe, OCLC: 841702542 (1992).

[101] H. Matsuoka, T. Nakai, Stress-strain relationship of soil based on the SMP, in: Proceedings from the Ninth International Conference on Soil Mechanics and Foundation Engineering, 1977, pp. 143–285.

[102] E. Bauer, Constitutive modelling of critical states in hypoplasticity, Proceedings of the Fifth International Symposium on Numerical Models in Geomechanics (1995) 15–20.

[103] E. Bauer, Calibration of a comprehensive hypoplastic model for granular materials, Soils and Foundations 36 (1) (1996) 13–26. `doi:10.3208/sandf.36.13`.

[104] I. Herle, Hypoplastizität und Granulometrie einfacher Korngerüste, Ph.D. thesis, Universität Karlsruhe, OCLC: 635192283 (1997).

[105] D. Mašín, Modelling of Soil Behaviour with Hypoplasticity: Another Approach to Soil Constitutive Modelling, 1st Edition, Springer, 2019, ISBN:978-3-030-03975-2.

[106] C. Woitzik, A. Düster, Experimental investigation of granules as crash-absorber in ship building, Ships and Offshore Structures 16 (3) (2020) 314–325. `doi:10.1080/17445302.2020.1727179`.

[107] H. S. Alsos, J. Amdahl, On the resistance of tanker bottom structures during stranding, Marine Structures 20 (4) (2007) 218–237. `doi:10.1016/j.marstruc.2007.06.001`.

[108] P. Rduch, Vergleich verschiedener Versagensmodelle von Metall im Zusammenhang mit Kollisionsversuchen von Schiffen, Master thesis, Technische Universität Hamburg (2018).

[109] H. Hooputra, H. Gese, H. Dell, H. Werner, A comprehensive failure model for crashworthiness simulation of aluminium extrusions, International Journal of Crashworthiness 9 (5) (2004) 449–464. `doi:10.1533/ijcr.2004.0289`.

[110] M. A. Chaudry, P. Wriggers, On the computational aspects of comminution in discrete element method, Computational Particle Mechanics 5 (2) (2018) 175–189. `doi:10.1007/s40571-017-0161-8`.

[111] M. A. Chaudry, C. Woitzik, A. Düster, P. Wriggers, A multiscale DEM–FEM coupled approach for the investigation of granules as crash-absorber in ship building, Computational Particle Mechanics (online) (2021) 1–19. `doi:10.1007/s40571-021-00401-5`.

[112] M. A. Chaudry, A multiscale DEM-FEM coupled approach for modelling of collision of particle-filled structures, Ph.D. thesis, Universität Hannover, ISBN:978-3-941-30235-8 (2020).

[113] P. A. Cundall, O. D. L. Strack, A discrete numerical model for granular assemblies, Géotechnique 29 (1) (1979) 47–65. `doi:10.1680/geot.1979.29.1.47`.

[114] G. N. Pande, Numerical Methods in Rock Mechanics, John Wiley & Sons Ltd, 1990, ISBN:978-0-471-92021-2.

[115] F. Radjai, F. Dubois, Discrete Numerical Modeling of Granular Materials., John Wiley & Sons, 2011, ISBN:978-1-84821-260-2.

[116] M. A. Chaudry, C. Woitzik, A. Düster, P. Wriggers, Experimental and numerical characterization of expanded glass granules, Computational Particle Mechanics 5 (3) (2018) 297–312. `doi:10.1007/s40571-017-0169-0`.

[117] M. A. Sulong, M. Vesenjak, I. V. Belova, G. E. Murch, T. Fiedler, Compressive properties of advanced pore morphology (APM) foam elements, Materials Science and Engineering: A 607 (2014) 498–504. `doi:10.1016/j.msea.2014.04.037`.

[118] K. Stöbener, D. Lehmhus, M. Avalle, L. Peroni, M. Busse, Aluminum foam-polymer hybrid structures (APM aluminum foam) in compression testing, International Journal of Solids and Structures 45 (21) (2008) 5627–5641. `doi:10.1016/j.ijsolstr.2008.06.007`.

[119] M. Vesenjak, M. Borovinšek, T. Fiedler, Y. Higa, Z. Ren, Structural characterisation of advanced pore morphology (APM) foam elements, Materials Letters 110 (2013) 201–203. `doi:10.1016/j.matlet.2013.08.026`.

[120] C. Reiner, Experimentelle Bestimmung der Materialeigenschaften von Granulaten zur Erhöhung der Kollisionssicherheit von Schiffen, Bachelor thesis, Technische Universität Hamburg-Harburg (2016).

[121] C. Woitzik, A. Düster, Modelling the material parameter distribution of expanded granules, Granular Matter 19 (3) (2017) 52. `doi:10.1007/s10035-017-0735-4`.

[122] P. Wriggers, B. Avci, Discrete element methods: Basics and applications in engineering, in: L. De Lorenzis, A. Düster (Eds.), Modeling in Engineering Using Innovative Numerical Methods for Solids and Fluids, CISM International Centre for Mechanical Sciences, Springer International Publishing, 2020, pp. 1–30. `doi:10.1007/978-3-030-37518-8_1`.

[123] B. M. Das, Principles of foundation engineering, 7th Edition, Thomson - Brooks/Cole, 2010, ISBN:978-0-495-41130-7.

[124] C. Woitzik, M. A. Chaudry, P. Wriggers, A. Düster, Statistical characterization of granular material applied as crash absorber in ship building, in: Proceedings in Applied Mathematics and Mechanics, Vol. 17, 2017, pp. 487–488. `doi:10.1002/pamm.201710213`.

[125] Y. Petukhov, H. Kalman, Empirical breakage ratio of particles due to impact, Powder Technology 143–144 (2004) 160–169. `doi:10.1016/j.powtec.2004.04.009`.

[126] E. Parzen, On estimation of a probability density function and mode, The Annals of Mathematical Statistics 33 (3) (1962) 1065–1076. `doi:10.1214/aoms/1177704472`.

[127] M. Rosenblatt, Remarks on some nonparametric estimates of a density function, The Annals of Mathematical Statistics 27 (3) (1956) 832–837. `doi:10.1214/aoms/1177728190`.

[128] V. K. Rohatgi, A. K. E. Saleh, An Introduction to Probability and Statistics, Second Edition, John Wiley & Sons, Inc., 2000. `doi:10.1002/9781118165676`.

[129] L. Devroye, Non-Uniform Random Variate Generation, Springer New York, 1986. `doi:10.1007/978-1-4613-8643-8`.

[130] R. B. Nelsen, An Introduction to Copulas, Springer Series in Statistics, Springer New York, 2006. `doi:10.1007/0-387-28678-0`.

[131] M. A. Chaudry, C. Woitzik, C. Weißenfels, A. Düster, P. Wriggers, DEM-FEM coupled numerical investigation of granular materials to increase crashworthiness of double-hull vessels, in: Proceedings in Applied Mathematics and Mechanics, Vol. 16, 2016, pp. 311–312. `doi:10.1002/pamm.201610144`.

[132] C. O'Sullivan, J. D. Bray, S. Li, A new approach for calculating strain for particulate media, International Journal for Numerical and Analytical Methods in Geomechanics 27 (10) (2003) 859–877. `doi:10.1002/nag.304`.

[133] W. K. Liu, S. Jun, Y. F. Zhang, Reproducing kernel particle methods, International Journal for Numerical Methods in Fluids 20 (8) (1995) 1081–1106. `doi:10.1002/fld.1650200824`.

[134] Y. Feng, K. Han, D. Owen, J. Loughran, On upscaling of discrete element models: similarity principles, Engineering Computations 26 (6) (2009) 599–609. `doi:10.1108/02644400910975405`.

[135] J. Korelc, U. Šolinc, P. Wriggers, An improved EAS brick element for finite deformation, Computational Mechanics 46 (4) (2010) 641–659. `doi:10.1007/s00466-010-0506-0`.

[136] C. Weißenfels, Contact methods integrating plasticity models with application to soil mechanics, Ph.D. thesis, Universität Hannover, ISBN:978-3-941302-06-8 (2012).

[137] J. C. Gelin, O. Ghouati, An inverse method for material parameters estimation in the inelastic range, Computational Mechanics 16 (3) (1995) 143–150. `doi:10.1007/BF00369777`.

[138] A. Tarantola, Inverse Problem Theory and Methods for Model Parameter Estimation, Other Titles in Applied Mathematics, Society for Industrial and Applied Mathematics, 2005. `doi:10.1137/1.9780898717921`.

[139] Dennert Poraver GmbH, Poraver - technical data sheet, data sheet, Dennert Poraver GmbH (2019) [cited 2020-08-13].
URL `https://www.poraver.com/`

[140] DIN e.V., DIN EN ISO 17892-8:2018-07, Geotechnische Erkundung und Untersuchung - Laborversuche an Bodenproben - Teil 8: Unkonsolidierter undränierter Triaxialversuch (ISO 17892-8:2018); Deutsche Fassung EN ISO 17892-8:2018, DIN standard, Beuth Verlag GmbH (2018). `doi:10.31030/2778750`.

[141] J. T. H. Wu, S. C.-Y. Tung, Determination of model parameters for the hardening soil model, Transportation Infrastructure Geotechnology 7 (1) (2020) 55–68. `doi:10.1007/s40515-019-00085-8`.

[142] I. Herle, P.-M. Mayer, Verformungsberechnung einer Unterwasserbetonbaugrube auf der Grundlage hypoplastisch ermittelter Parameter des Berliner Sandes, Bautechnik 76 (1) (1999) 34–48. `doi:https://doi.org/10.1002/bate.199900050`.

[143] D. Kolymbas, E. Bauer, Soft oedometer - a new testing device and its application for the calibration of hypoplastic constitutive laws, Geotechnical Testing Journal 16 (2) (1993) 263–270. `doi:10.1520/GTJ10044J`.

[144] J. Williams, C. Gamonpilas, Using the simple compression test to determine young's modulus, poisson's ratio and the coulomb friction coefficient, International Journal of Solids and Structures 45 (16) (2008) 4448–4459. `doi:10.1016/j.ijsolstr.2008.03.023`.

[145] DIN e.V., DIN 2413:2018-01, Nahtlose Stahlrohre für öl- und wasserhydraulische Anlagen - Berechnungsgrundlage für Rohre und Rohrbögen bei schwellender Beanspruchung, DIN standard, Beuth Verlag GmbH (2018). `doi:10.31030/2794888`.

[146] C. Woitzik, M. A. Chaudry, P. Wriggers, A. Düster, Experimental and numerical investigation of granular materials for an increase of the collision safety of double-hull vessels, in: Proceedings in Applied Mathematics and Mechanics, Vol. 16, 2016, pp. 409–410. `doi:10.1002/pamm.201610193`.

[147] P. Rduch, Approximation der Materialparameter von granularen Füllstoffen mittels eines Minimierungsproblems, Project thesis, Technische Universität Hamburg-Harburg (2017).

[148] R. Gomeringer, Tabellenbuch Metall: ohne Formelsammlung, 46th Edition, Europa-Fachbuchreihe für Metallberufe, Europa-Lehrmittel, 2014, ISBN:978-3-8085-1726-0.

[149] I. The MathWorks, MATLAB, Software, The MathWorks, Inc. (2019) [cited 2019-08-08].
URL `https://www.mathworks.com/products/matlab.html`

[150] M. J. Kochenderfer, T. A. Wheeler, Algorithms for Optimization, MIT Press Ltd, 2019, ISBN:978-0-262-03942-0.

[151] R. H. Byrd, M. E. Hribar, J. Nocedal, An interior point algorithm for large-scale nonlinear programming, SIAM Journal on Optimization 9 (4) (1999) 877–900. `doi:10.1137/S1052623497325107`.

[152] R. H. Byrd, J. C. Gilbert, J. Nocedal, A trust region method based on interior point techniques for nonlinear programming, Mathematical Programming 89 (1) (2000) 149–185. `doi:10.1007/PL00011391`.

[153] R. Waltz, J. Morales, J. Nocedal, D. Orban, An interior algorithm for nonlinear optimization that combines line search and trust region steps, Mathematical Programming 107 (3) (2006) 391–408. `doi:10.1007/s10107-004-0560-5`.

[154] S. Krämer, S. Rothe, S. Hartmann, Homogeneous stress–strain states computed by 3d-stress algorithms of FE-codes: application to material parameter identification, Engineering with Computers 31 (1) (2015) 141–159. `doi:10.1007/s00366-013-0337-7`.

[155] J. K. Paik, Computational models for structural crashworthiness analysis in collisions and grounding, in: J. K. Paik (Ed.), Advanced Structural Safety Studies: With Extreme Conditions and Accidents, Topics in Safety, Risk, Reliability and Quality, Springer Singapore, 2020, pp. 279–311. `doi:10.1007/978-981-13-8245-1_11`.

[156] G. Gruben, D. Vysochinskiy, T. Coudert, A. Reyes, O.-G. Lademo, Determination of ductile fracture parameters of a dual-phase steel by optical measurements, Strain 49 (3) (2013) 221–232. `doi:10.1111/str.12030`.

[157] G. Gruben, S. Sølvernes, T. Berstad, D. Morin, O. Hopperstad, M. Langseth, Low-velocity impact behaviour and failure of stiffened steel plates, Marine Structures 54 (2017) 73–91. `doi:10.1016/j.marstruc.2017.03.005`.

[158] M. Storheim, J. Amdahl, I. Martens, On the accuracy of fracture estimation in collision analysis of ship and offshore structures, Marine Structures 44 (2015) 254–287. `doi:10.1016/j.marstruc.2015.09.006`.

[159] K. Liu, Z. Wang, W. Tang, Y. Zhang, G. Wang, Experimental and numerical analysis of laterally impacted stiffened plates considering the effect of strain rate, Ocean Engineering 99 (2015) 44–54. `doi:10.1016/j.oceaneng.2015.03.007`.

[160] L. Hong, Simplified analysis and design of ships subjected to collision and grounding, Ph.D. thesis, Norwegian University of Science and Technology, ISBN:978-82-471-1398-1 (2018).

[161] B. Liu, R. Villavicencio, C. Guedes Soares, Experimental and numerical plastic response and failure of laterally impacted rectangular plates, Journal of Offshore Mechanics and Arctic Engineering 135 (4). `doi:10.1115/1.4024274`.

[162] S. Ehlers, H. Remes, A. Klanac, H. Naar, A multi-objective optimisation-based structural design procedure for the concept stage – a chemical product tanker case study, Ship Technology Research 57 (3) (2010) 182–196. `doi:10.1179/str.2010.57.3.004`.

[163] O.-V. E. Sormunen, S. Ehlers, P. Kujala, Collision consequence estimation model for chemical tankers, in: Proceedings of the Institution of Mechanical Engineers, Part M: Journal of Engineering for the Maritime Environment, Vol. 227(2), 2013, pp. 98–106. `doi:10.1177/1475090212462192`.


VDI nachrichten
TECHNIK WIRTSCHAFT GESELLSCHAFT
Schlüsseltechnologie Power-to-X
ENERGIEWENDE: Deutschland erreicht seine Klimaziele nur mit einer umfassenden Dekarbonisierung aller Sektoren.
VON STEPHAN W. EDER, PETER KELLERHOFF UND BETTINA RECKTER

REIHE 18
MECHANIK/
BRUCHMECHANIK

NR. 356

ISBN 978-3-18-335618-8

BAND
1|1

VOLUME
1|1